Modelling of Fast Ion Losses in Tokamaks

Manuel García Muñoz

Diploma Thesis performed at the
Max-Planck-Institut für Plasmaphysik
fulfilling the requirements of the
Ludwig-Maximilians-Universität of Munich.

May 11, 2003

Contents

Chapter 1

Introduction

1.1 Basics

Fusion, the way in which the Sun obtains its energy, has the potential of providing an essentially unlimited source of energy. Human beings have been searching for a long time for a way to reproduce such a source of energy. The Sun generates its energy by means of the following reactions:

$$
\begin{align}
p + p &= D + e^+ + \nu_e + 1.5\,\text{MeV} \tag{1.1} \\
D + p &= {}^3\text{He} + \gamma + 5.4\,\text{MeV} \tag{1.2} \\
{}^3\text{He} + {}^3\text{He} &= {}^4\text{He} + 2p + 12.9\,\text{MeV} \tag{1.3}
\end{align}
$$

The cross-section for the whole cycle due to the weak interaction involved in reaction (1.1) is too low to reproduce on Earth (the Sun overcomes this problem by its huge mass). Because of this, for controlled Fusion on Earth only the following reactions are possible candidates:

$$
\begin{align}
D + T &= {}^4\text{He} + n + 17.6\,\text{MeV} \tag{1.4} \\
D + {}^3\text{He} &= {}^4\text{He} + p + 18.4\,\text{MeV} \tag{1.5} \\
D + D &= n + {}^3\text{He} + 3.27\,\text{MeV} \tag{1.6} \\
D + D &= p + T + 4.032\,\text{MeV} \tag{1.7}
\end{align}
$$

However, in order to reach the "ignition" conditions (when the fusion-born particles heat the plasma and compensate for the heat losses) even for the most favorable reaction between deuterium and tritium (1.4), the D-T Plasma must be heated to a temperature of $T \approx 20\text{keV}$ [1](230 million K) and must be confined to satisfy the Lawson criterion:

---

[1]Following the convention accepted in Fusion, temperatures are written in eV. Thus, in place of conventional kT^0 (where k is Boltzmann's constant and T^0 is in degrees Kelvin) we write T(eV), so that $T^0 = T(joules)/1.381 \cdot 10^{-23}$, where $T(joules) = T(eV) \cdot 1.602 \cdot 10^{-19}$.
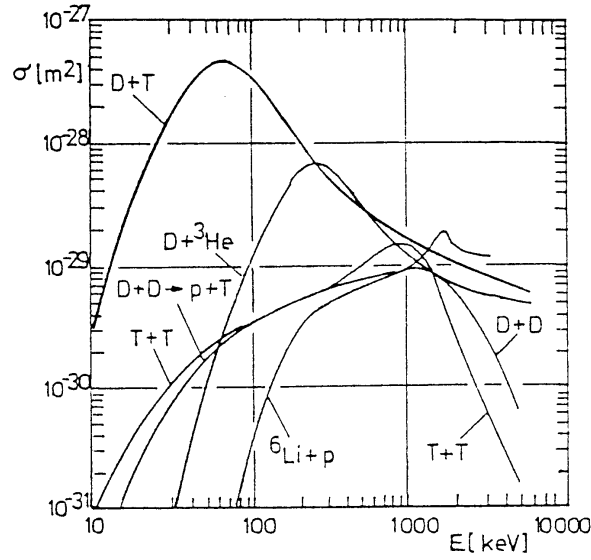
Figure 1.1: Cross-section of different fusion reactions

$$n\tau_E > 1.5 \cdot 10^{20} \text{ m}^{-3}\text{s} \qquad (1.8)$$

where τ_E is the energy confinement time and n is the D-T fuel density.

As Fig (1.1) shows, all reaction's cross sections highly depend on the relative kinetic energy of the nuclei in the center-of-mass system. The D-T reaction is the one with the largest cross-section at the lowest energies. Therefore, the most suitable candidate for a fusion reactor is the reaction (1.4). Here, a resonant metastable state is formed, (^{4}He) providing the highest cross-section of all fusion reactions.

In present experiment, usually D fuel is used to avoid the large neutron flux produced in reaction (1.4), as well as the T-handling, despite the fact that the cross section in reactions (1.6) and (1.7) is lower by a factor of 10-100 compared to the D-T reaction.

It is important to remark that to be a candidate for an energy-producing system, the fusion fuel has to be sufficiently abundant. Deuterium comes as a fraction of $3.3 \cdot 10^{-5}$ in water. Given the water of the oceans, the static energy range is larger than the time the Sun will continue to burn (a few billion years). The other reactive for the fusion, tritium, is an unstable radioactive isotope of the hydrogen, with a half-life of 12.3 years. Due to the unstable nature of the tritium, a significant amount does not exist. But tritium can be produced easily with nuclear reactions of the neutrons from D-T reaction and lithium. In this way, the only fusion fuels will be deuterium and lithium. Keeping in mind that lithium is also very abundant on the Earth's crust and even in the ocean's water, table (1.1) summarizes the estimated world energy resources [Wesson, 1997].

From the Lawson Criterium is easy to understand the importance of a long confinement time for the fusion. That is because of the high cross-section for the elastic Coulomb scattering,

Present world annual primary energy consumption	$3 10^{11}$ gigajoules	Time
Resources		
Coal	10^{14}	300 years
Oil	$1.2 \cdot 10^{13}$	40 years
Natural Gas	$1.4 \cdot 10^{13}$	50 years
235^{U} (fission reactors)	10^{13}	30 years
238^{U} and $232^{T}h$ (breader reactors)	10^{16}	30000 years
Lithium (D-T fusion reactors):		
Land	10^{16}	30000 years
Oceans	10^{19}	$3 \cdot 10^{7}$ years

Table 1.1: Energy resources

higher than the cross-section for a fusion process σ_{Fus} by a factor of 10^4 at 10 keV and even higher at lower temperatures. That makes the use of cross particle beams not suitable for the generation of fusion energy. Thus, the particles must long enough be confined to a volume in order to undergo many collisions.

Nowadays, two methods of confinement are investigated in fusion research to reach an ignited plasma.

Inertial confinement High density and short confinement time. A solid pellet is heated by a laser or a heavy ion beam in order to achieve a density of $10^{30} m^{-3}$ in a volume of a fraction of mm^3. Thus, for a very short time (μs), a dense hot plasma is produced and confined by its inertia. During this time, fusion can take place. Problems arise due to the low efficiency of the driver beams and the need for a highly symmetric irradiation (asymmetries lead to instabilities during the compression process).

Magnetic confinement Low density and long confinement time. Since charged particles gyrate around magnetic field lines, a plasma may be confined in a magnetic cage. A typical gyroradius of a deuteron in a field of $B = 3T$, with an energy of $T = 10$keV is $\rho_D \simeq 6.8mm$. Therefore, the particles are tied to the field lines. There are different magnetic topologies, being stellarators Fig.(1.2.a) and tokamaks Fig(1.2.b) the most common . The one that is most promising at present is the Tokamak configuration.

1.2   Tokamaks

As a first attempt to confine particles by magnetic fields, a cylindrical configuration could be taken into account . As particles can move freely along field lines, such devices suffer from end losses. To overcome this problem, the cylinder can be bent into a torus, generally allowing particles to be confined in all directions. The tokamak is a toroidal plasma confinement machine.
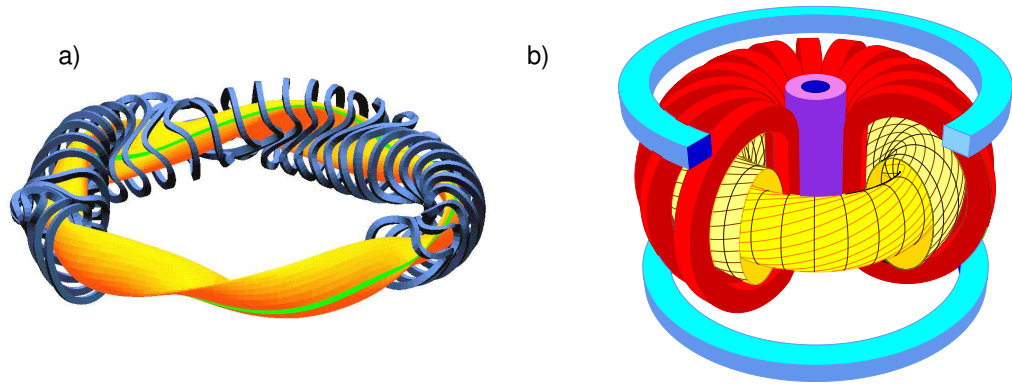
Figure 1.2: Schematic drawing of a tokamak and a stellarator

The main magnetic field is a toroidal one, but the plasma could not be confined only with this one. The toroidal magnetic field is produced by coils. In order to achieve an equilibrium, the different drifts have to be compensated by means of a poloidal magnetic field. This field is produced by an internal current flowing in the toroidal direction, I_{Plasma}. The combination of both fields gives rise to magnetic field lines which have helical trajectories around the torus, Fig. (1.2.b)and form the so-called magnetic surfaces, Fig. (1.3).

Tokamak plasmas are heated to temperatures of a few keV by the ohmic heating of the plasma current. The required temperatures around 10 keV are then achieved by additional heating by particle beams or electromagnetic waves. Nowadays tokamak plasmas have particle densities of around $10^{19} - 10^{20} m^{-3}$. This is a factor 10^6 lower than in the atmosphere. Therefore, the plasma has to be contained within a vacuum vessel and to minimize the presence of impurities, low background pressures must be maintained. Impurities in the plasma give rise to radiation losses and also dilute the fuel. The limiting of the amount of impurities into the plasma plays a fundamental role in the successful operation of tokamaks; in order to do so, the plasma has to be separated from the vessel wall. There are two techniques to carry this out. Both possibilities give the plasma a different shape. The first one is to define an outer boundary of the plasma with a material limiter. The second one is to keep the particles away from the vacuum vessel by means of a modification of the magnetic field to produce a magnetic divertor as shown in Fig. (1.3)

1.3   Fast Particles

In order to reach the ignition conditions described above, the tokamak plasma is heated by the ohmic dissipation of the induced current by additional heating schemes such as the injection of high energy neutral beams, or by launching electromagnetic waves into the plasma. Once ignited, the plasma is intended to become entirely self-heated through the fusion-born α-particles (He^4 nuclei of energy 3.52 MeV).

It is the aim of this work to study in depth the behavior of fast ions by means of particles which
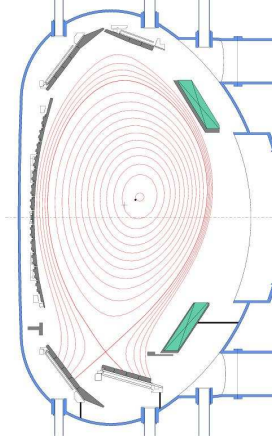
Figure 1.3: Magnetic surfaces of a typical discharge in ASDEX Upgrade.

are generated by the NBI heating. Considering the distribution function of the background ions in the velocity space as a Maxwellian distribution, this work concerns particles which have a much higher energy that the thermal energy of the background plasma and their density is much higher than that in the tail of the Maxwellian.

Larmor Radius	Temperature			
	100 eV	1 keV	10 keV	100 keV
ρ_e	0.011 mm	0.035 mm	0.11 mm	0.35 mm
ρ_p	0.48 mm	1.5 mm	4.8 mm	15.18 mm
ρ_D	0.68 mm	2.1 mm	6.8 mm	21.5 mm

Table 1.2: Typical Larmor Radius of various fast ions, B=3T.

As table (1.2) shows, such ions have a Larmor radius much larger than the electrons' one, $r_{li} >> r_{le}$, due to their high energy and mass. Differences between the 5 keV fast particle trajectory and the one with 100 keV , due to its Larmor radius, can be easily seen in Fig. 1.4.

Expected velocities of such ions are very high compared with thermal ions ones, but not high enough for considering the relativistic correction. The given values for ions with an energy of several dozens of keV (40-100 keV) are around 10^6 m/s. Thus, the relativistic correction is small and the non relativistic mechanic is accurate enough.

In general, the performance of fusion plasmas is affected by fast ion confinement in different ways [Werner, 2001]:

- Fast ions can be lost within μs, i.e. before they have slowed down. This deteriorates the efficiency of the heating scheme by which they were initially produced. A charged particle detector installed at the edge of the plasma could measure the flux and the energy of the fast ions. Experiments have been undertaken at several tokamaks PLT [Heidbrink, 1984], ASDEX [Bosch, 1987], JET [Kallne, 1987], DIII-D [Duong, 1990], TFTR [Boivin, 1993] and TEXTOR [Bonheure, 2000].
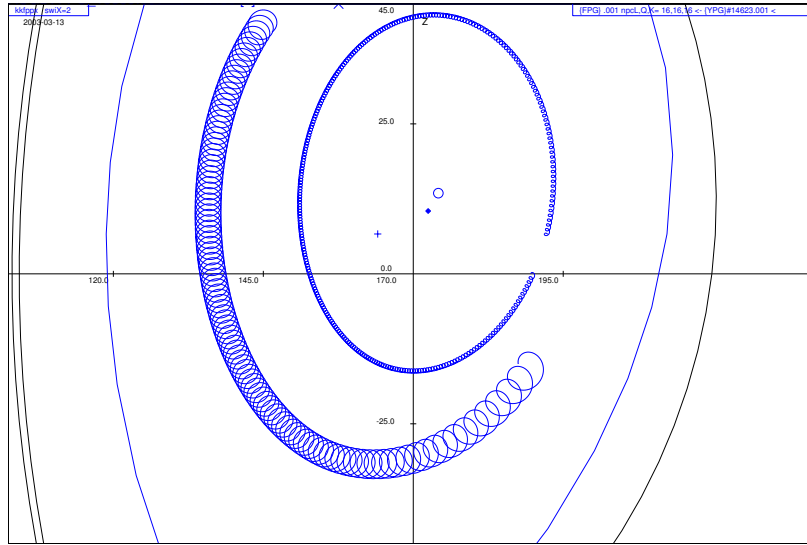
8

Figure 1.4: Typical orbits of a deuterium with 93 keV and 5 keV respectively.

- If fast ion fluxes encounter the first wall, excessive heat loads and additional impurities are generated by sputtering or desorption processes. In discharges with good impurity confinement this may endanger stationary plasma operation as envisaged for fusion reactors.This effect has been observed in the Tokamak Fusion Test Reactor (TFTR)[Hawryluk, 1991].

- In order to prevent accumulation of the helium ash, it has to be removed from the vacuum vessel, that plays even a much more important role for further Tokamak reactors like ITER. Since helium particles are produced with a high velocity, the study of fast ions becomes much more important.

Thus, the confinement properties of these highly energetic particles (α-particles and NBI-particles) are therefore of crucial importance for further tokamak reactors.

Several studies with neutral beam injection (NBI) and α -particles on different Tokamaks are carried out in order to understand in depth the possible loss mechanisms.

In order to simplify the study of the different loss mechanisms two groups are suggested.

- Fast ions can be lost due to insufficient confinement properties of the magnetic field topology, [Darrow, 2002]. The so-called *prompt losses* are particles which, after the ionization, are on a such orbit that they are immediately lost from the plasma. For particles that are initially well confined, collisions can lead to transitions from an initially confined orbit to an unconfined orbit, resulting in the loss of this particle.

- Losses may also be induced by magnetohydrodynamic (MHD) perturbations. Experiments with neutral beam injection (NBI) and α -particles on Tokamaks DIII-D

9

[Duong, 1993a] and TFTR [Darrow, 1992] in D-T plasmas have shown that under certain conditions Alfvén instabilities can cause a significant loss of those particles. Due to their relatively high phase velocity, $v_A \sim 5 \cdot 10^6 m/s$, Alfvén waves mainly resonate [Rosenbluth, 1975] with these highly energetic particles by means of their ∇B drifts. This interaction can destabilize the MHD modes whenever $\omega < \omega_b$, where ω_b is the diamagnetic frequency of the beam. Different MHD-induced loss mechanisms are suggested, [Duong, 1993b].

Beam ions that circulate at the mode frequency can experience convective radial transport. This mechanism was studied on PDX tokamak, [White, 1983] with "fishbones" activity . This "mode particle pumping" loss mechanism causes the fast ions to migrate radially outward due to E × B drifts. The initial value of the magnetic moment μ is conserved, and the radial velocity is linearly proportional to the mode amplitude $\tilde{B}$. This kind of losses are concentrated near the midplane and occur only when the beam has a particular phase with respect to the instabilities.

A second loss resonant mechanism is associated with the loss of parallel velocity, due to resonant interaction between high energetic α particles and Alfvén waves. They become resonant and lose energy to the wave. With the loss of parallel energy, initially passing particles can become trapped in the inner leg of their orbit and move onto a large, unconfined banana orbit. The losses are predicted to scale linearly with the mode amplitude $\tilde{B}$ [Sigmar, 1992]. According to studies on DIII-D tokamak [Duong, 1993b] with TAE modes, there is no threshold amplitude in the scaling of fast ion losses with mode amplitude, suggesting that mode particle pumping is the dominant loss mechanism. In simulations, this mechanism can dominate alpha losses during TAE modes, [Sigmar, 1992]. Experiments with neutral beam injection (NBI), [Wong, 1991] and [Heidbrink, 1991], and α-particles, [White, 1995] and [Duong, 1993a], on TFTR and on DIII-D have shown that under certain conditions such Alfvén instabilities can cause significant losses.

Another possible mechanism is orbit stochasticity [Sigmar, 1992]. This process does not depend on a resonant interaction with the mode; rather the helical distortion of the field beats with harmonics of the orbital motion causing island overlap in phase space. Once island overlap occurs, the particles diffuse rapidly. Transport associated with orbit stochasticity only occurs above a threshold in the mode amplitude. It is important to understand that even fast particles on passing drift orbits, which are normally thought of as well confined, can be affected by orbit stochasticity. Several studies of beam ion transport during MHD activity [Carolipio, 1998] show that these losses scale approximately as $\tilde{B}^2$. In that work large coherent MHD modes were observed to reduce the neutral beam current drive efficiency by a factor of 40 % through orbit stochasticity. On a positive side, orbit stochasticity has been connected with a technique of removing intermediate energy α-particles in a reactor through the external application of helical perturbations [Mynick, 1993].

1.4   Scope of this Work

The confinement of fast ions was studied in detail in deuterium-deuterium (DD) scenarios of the ASDEX Upgrade tokamak. As seen in the previous section, the performance of fusion plasmas is affected by fast ion losses. In order to understand theoretically the fast ion losses, a full description of fast ion trajectories from birth to loss was made. Collisions between beam ions and background ions as well as electrons were taken into account. It is the aim of this work to compute the deposition patterns of injected 93 keV deuterons on the tokamak wall, under normal operating conditions as well as in the presence of MHD instabilities.

To measure these losses, the installation of a detector in ASDEX Upgrade is intended. The most favorable place to install it was calculated using the code-packages. In order to interpret measurements once the detector is installed, the code-packages will be of great value.

A real magnetic field configuration was taken from the ASDEX Upgrade tokamak.

The complexity of the magnetic field configuration does not allow an analytical integration of the trajectory. So it was found necessary to use a computational method. The numerical calculations are performed using the following three codes: FAFNER [Lister, 1985], HAGIS [Pinches, 1996] and GOURDON [Gourdon, 1970], each one for each period of the fast ion trajectory.

For this magnetic configuration, the FAFNER code calculates the distribution function of fast ions from the NBI heating. FAFNER calculates exactly where each particle was ionized and also its pitch angle. That conforms the initial distribution function for HAGIS code. Thousands of co- and counter-injected deuterons are traced inside and outside the plasma until they either reach the wall or a time limit is reached. Inside the plasma boundary, the guiding centers are traced with the HAGIS code using Boozer-coordinates. Pitch angles scattering, MHD instabilities and also the slowing down of the particles are taken into account. In the edge region, to trace real orbits as well as to compute fast ion deposition on the wall, an extended version of GOURDON code was used. The underlying code system is summarized in Fig(1.5), which serves as a reminder throughout the thesis.

1.4.1   GOURDON

The final version of GOURDON used here has some differences compared to the original one, which was planed to compute trajectories with a stellarator magnetic field configuration and did not run under the computer platform used at ASDEX Upgrade. Therefore, several changes were made in order to adapt GOURDON code to the ASDEX Upgrade topology and to the work environment (which means the Sun machines used for computation). The magnetic field equilibrium was computed using the routines which allow to calculate the equilibrium using different statistical methods. Since these routines provide the equilibrium in toroidal coordinates and GOURDON works in cartesian coordinates, the appropriate coordinate transformation in the code was made. GOURDON then writes the magnetic field in a 2-D grid though it calculates particle trajectories in 3-D. The implementation of the ASDEX Upgrade geometry was made, taking into account that the number and position of the target-plates vary with the
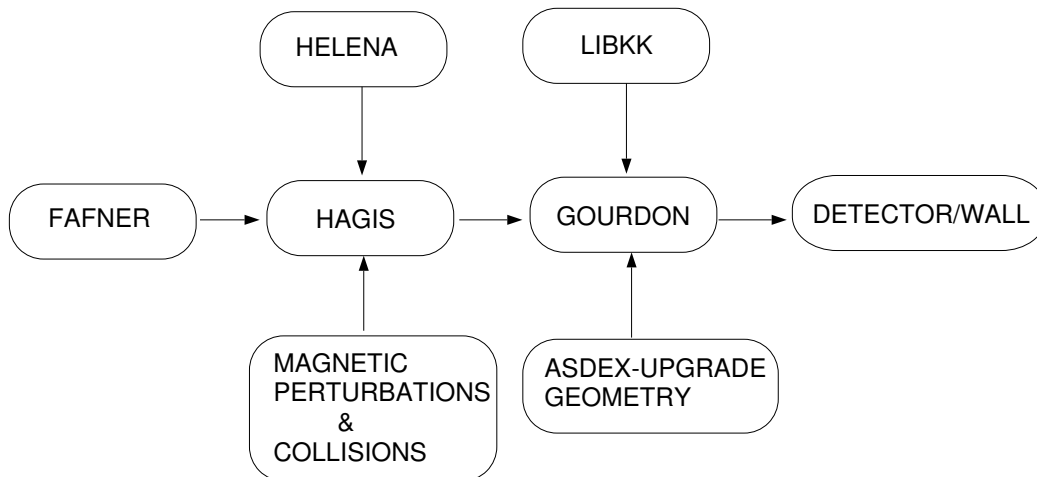
Figure 1.5: Overview of the codes

shot number. The corresponding coordinates to each target-plate were calculated. The implementation of the geometry in the code was made as follows: at each step of the integration of the trajectory, it was asked if the particle had crossed a target-plate or not. Several tests were carried out, following magnetic field lines in order to validate the final code.

1.4.2 HAGIS

The input data required by HAGIS-code consist of four parts: the equilibrium field configuration, the perturbed field data, the fast particles initial condition, and the collision parameter.

The magnetic field configuration is supplied by the HELENA-code [Huysmans, 1990], by solving the Grad-Shafranov equation. The perturbed field is given by computing the changes in the poloidal flux function, by means of Fourier harmonics which represent the MHD-mode. The fast particles initial conditions are supplied by the FAFNER-code, considering the parameter corresponding to the discharge used in this work, and making the density of fast ions to be zero outside the separatrix.

Since FAFNER supplies the fast ions' initial conditions in toroidal coordinates, the correct transformation to Boozer coordinates was made.

The collisions were implemented into the code by computing a specific Fokker-Planck collision operator given by [Littlejohn, 1982].

In order to obtain the desired data of the lost particles, for a better understanding of ion losses, a subroutine which supplies all of these data in m.k.s. units was also programmed.

1.4.3 Results

The study of fast ion losses in ASDEX Upgrade was made during this work, using the code-package here presented. The trajectory of thousands of particles was computed from the begin-

ning, where the particles are born, until they leave the plasma, striking the wall of the vessel. The initial distribution of the fast ions, calculated using the NBI parameters with FAFNER, is fully described in its section, representing the distribution in the real space as well as in the space of velocities. It is shown that the distribution in the plane, formed by the two toroidal coordinates, ϕ and z, has two branches, since the beam simulated was almost tangential to the inner side of the torus. The distribution in the velocity space seems to be not homogeneous since all injected particles have the same energy and almost the same direction. The exponential decay of the ionization with the radial coordinate is shown in this section, the largest number of the neutral atoms are ionized just after they enter the plasma.

The NBI simulation supplies the initial distribution for the HAGIS code. The behavior of the fast ions inside the plasma was studied using HAGIS. Fast ion's trajectories were computed under different conditions. It was found that the final distribution of losses is always localized in the poloidal angle, but not always in the toroidal direction. Different cases with collisions and MHD-modes were considered leading to different distributions in the plane formed by the flux coordinates ϕ and θ as well as in the velocity plane. In absence of collisions and MHD-modes, the distribution of fast ion losses was studied for two different cases, co- and counter-going particles. It was proved that the number of prompt losses due to counter-injected particles was larger than in the case of co-injected particles. Once collisions were considered, the velocity of the lost particles was found all over the plane of velocities, but distributed in three regions: The one where the lost particles had not changed their velocity, the one where the particles, which leave the plasma, have velocities lying in the loss cone, (trapped orbits cause large radial excursions) and the region where the particles have slowed down and have given their energy to the bulk of the plasma, thermal particles. The effect of collisions on the ions leads to a symmetrization of the spatial distribution of the losses in the toroidal direction. Two time-independent different modes were studied with a high amplitude and a given radial profile, leading to different distributions in the real space, as well as in the velocity space.

Since the location of each mode is different in the radial coordinate, two different radial profiles, each one for each mode, were computed. The fast ion losses, considering the mode n=1 and m=4, were found along the field lines, corresponding to the flux surface q=4. Thus, the spatial distribution is not localized around any toroidal or poloidal angle anymore. However, more losses around the location of the neutral beam injector were found, where the prompt losses are.

The effect of the mode m=2 on the spatial distribution of the losses leads to a symmetrization in the toroidal direction, still being localized around the midplane. However, more losses were also found in this case around the X-point of the inland.

In order to validate the code, the confinement time and the slowing down of particles were calculated and compared with analytical results obtained under the neoclassical approach. Once particles have left the plasma, they are followed by means of the real orbits' code, GOURDON. Between the separatrix and the vessel walls, the orbits were traced using GOURDON, in order to know where they strike the vessel. That made possible the following of a particle which starts at the wall with specific parameters and cross the separatrix at a (ϕ, R, z) position, allowing the study of the reason for such a loss. The validation of GOURDON with AS-

DEX Upgrade configuration was made tracing some trajectories of fusion born particles and then comparing it with the guiding center trajectory calculated with HAGIS. Finally, the code-packages here presented was used as a first attempt to name the particles which strike a further detector. The operation of a detector based on the mechanism of a magnetic spectrometer was studied and is also presented.

Chapter 2

Particle Motion in Toroidal Magnetic Devices

2.1 Introduction

As is well-known, a charged particle must follow a homogeneous magnetic field line as long as there is no other interaction.

The motion of a non-relativistic particle of charge q and mass m in an electric field E and magnetic field, B is given by the following equation:

$$m\frac{d\mathbf{v}}{dt} = e(\mathbf{E} + \mathbf{v} \times \mathbf{B}) \tag{2.1}$$

In a tokamak, external forces such as gravity are negligible in comparison with electromagnetic ones. Considering only the magnetic field, the components of this equation are:

$$\frac{dv_x}{dt} = \omega_c v_y, \quad \frac{dv_y}{dt} = \omega_c v_x, \tag{2.2}$$

$$\frac{dv_z}{dt} = 0, \tag{2.3}$$

where

$$\omega_c = \frac{eB}{m} \tag{2.4}$$

is the cyclotron frequency and the z axis has been chosen to be along the magnetic field. From this set of equations one derives that the particle trajectory is a helical orbit composed of the circular motion perpendicular to the field and a constant velocity in the direction of the magnetic field. The radius of this circular motion is the Larmor radius:

$$\rho_l = \frac{mv_\perp}{qB} \tag{2.5}$$

where $v_\perp$ is the velocity component in the plane perpendicular to the magnetic field. The fast gyro motion can be separated from the guiding center motion, when the Larmor radius ρ_l is small compared to the characteristic length of the magnetic field variation :

$$L = \frac{B}{|\nabla B|} \gg \rho_l \qquad (2.6)$$

2.1.1 Adiabatic Invariants

It is well known from classical mechanics [Goldstein, 1980], that whenever a system has a periodic motion, the action integral $\oint pdq$ taken over a period is a constant of motion. Here p and q are the generalized momentum and coordinate. If the fields in the system change slowly compared with the characteristic period and on a scale large compared with the characteristic length of the motion, then the quantity $\oint pdq$ remains constant too, and is called an *adiabatic invariant*. Adiabatic invariants play an important role in plasma physics. There are three adiabatic invariants, each corresponding to a different type of motion. Being the magnetic moment defined as $\mu = mv_\perp^2/2B$, the first adiabatic invariant with respect to the motion of charged particles in an electromagnetic field. The periodic motion is the Larmor gyration, p is the angular momentum $mv_\perp\rho$, and the coordinate q is the angle θ. Considering the action integral yields

$$\oint pdq = \oint mv_\perp\rho_l d\theta = 2\pi\rho_l mv_\perp = 4\pi\frac{m}{e}\mu. \qquad (2.7)$$

The invariance of μ plays an important role in the study of the particle motion parallel to the magnetic field.

2.1.2 Guiding Center Motion

The evaluation of the confinement time of particles in fusion devices and the determination of particle diffusion requires to follow particle orbits for very long times [White, 1989]. In order to integrate the particle motion for the required length of time, an expansion of the equations of motion in the gyro radius must be made, and the rapid particle gyro phase motion averaged out, leaving equations for the guiding center motion. The Larmor radius of a charged particle in a tokamak plasma is small, compared to the plasma dimensions and the curvature radius of the magnetic field. Even fusion products with energies of a few MeV have Larmor radius 1/20 of the minor radius of a typical tokamak reactor design. Thus, charged particle motion is well described using the drift approximation. The guiding center equations of motion, which describes this drift motion, were first developed by Alfvén [Alfvén, 1940].

Taking **F** as an external force, the motion of charged particles can be studied by means of the following formula:

$$m\frac{d\mathbf{v}}{dt} = \mathbf{F} + e(\mathbf{v} \times \mathbf{B}) \qquad (2.8)$$
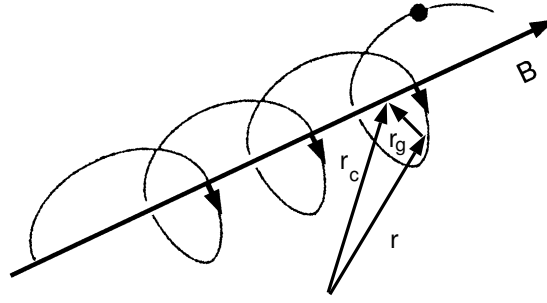
16

Figure 2.1: Guiding center coordinates

The guiding center approximation Fig. (2.1) provides the possibility to separate the motion of charged particles in a magnetic field into two different motions, the gyration due to B and the effect of an external force. If the guiding center "c" is the center of the gyration cycle, its position can be written as

$$\mathbf{r}_c = \mathbf{r} + \mathbf{r}_g \tag{2.9}$$

where r is the position of the particle and r_g the gyration radius vector

$$\mathbf{r}_g = \frac{m}{qB^2} \mathbf{v} \times \mathbf{B} \tag{2.10}$$

In *strongly magnetized* plasmas, such as in fusion experiments, the Lorentz force dominates other forces **F**. Then, ρ_l is often much smaller than other length scales, and ω_c much higher than other frequencies. Consequently, the particle orbit is well described by the motion of the guiding center. Deriving the equation (2.9), the velocity of the guiding center for a constant magnetic field is given by:

$$\mathbf{v}_c = \dot{\mathbf{r}}_c = \mathbf{v} + \frac{m}{eB^2} \frac{d\mathbf{v}}{dt} \times \mathbf{B} \tag{2.11}$$

$$= \mathbf{v} + \frac{1}{eB^2} (e(\mathbf{v} \times \mathbf{B}) + \mathbf{F}) \times \mathbf{B}. \tag{2.12}$$

Finally, from the vector relation

$$(\mathbf{v} \times \mathbf{B}) \times \mathbf{B} = (\mathbf{v}_\perp \times \mathbf{B}) \times \mathbf{B} = \mathbf{B}(\mathbf{v}_\perp \cdot \mathbf{B}) - \mathbf{v}_\perp (\mathbf{B} \cdot \mathbf{B}) = -\mathbf{v}_\perp B^2, \tag{2.13}$$

arises the guiding center velocity

$$\mathbf{v}_c = \mathbf{v}_\parallel + \frac{\mathbf{F} \times \mathbf{B}}{qB^2} \tag{2.14}$$

The motion of the guiding center can then be split into the two components referred to the magnetic field

$$\mathbf{v}_{c,\perp} = \frac{\mathbf{F}_\perp \times \mathbf{B}}{eB^2}, \qquad\qquad \frac{d\mathbf{v}_{c,\parallel}}{dt} = \frac{\mathbf{F}_\parallel}{m}. \qquad\qquad (2.15)$$

Any force with perpendicular components to the magnetic field leads to a perpendicular motion to **B** and **F** with the velocity $\mathbf{v}_{c,\perp}$.

2.1.3 Particle drifts

A non-homogeneous magnetic field or an electric field can lead to a guiding center particle drift perpendicular to the magnetic field.

$E \times B$ **drift**

A constant electric field is just a force with perpendicular components to the magnetic field, taking the electric force as an external force **F** and substituting it into the equation for the drift motion of the guiding center (2.15), leads to a drift,

$$\mathbf{v}_E = \frac{\mathbf{E} \times \mathbf{B}}{B^2}. \qquad\qquad (2.16)$$

The $\mathbf{E} \times \mathbf{B}$ drift leads to a macroscopic movement of the plasma since it does not depend on the sign of the charge or the mass of the particles.

∇B **drift and Curvature drift**

Inhomogeneous magnetic fields lead to two different drifts because of the perpendicular component of ∇B and the curvature of their field lines.

For magnetic fields that vary slowly in space, equation (2.15)can still be applied if the relative variation of B is small along one gyration of the particle.

In case of a magnetic field with a transverse gradient, the particle gyro-motion has a smaller radius of curvature on that part of its orbit, located in the stronger magnetic field, which leads to a drift perpendicular to both the magnetic field and its gradient. The force on a particle with a magnetic moment μ is given by

$$\mathbf{F}_{\nabla B} = -\mu \nabla B, \qquad\qquad (2.17)$$

which leads to

$$\mathbf{v}_{\nabla B} = -\frac{mv_\perp^2}{2eB^3}(\nabla_\perp B) \times \mathbf{B}. \qquad\qquad (2.18)$$

If there are curved magnetic field lines, a perpendicular drift appears in the plane in which the curvature lies. To understand this effect, a coordinate system which rotates with the angular

velocity, $v_\parallel/R$ of the particle is introduced where R is the radius of curvature of the field line. In this frame, the particle experiences a centrifugal force

$$\mathbf{F}_c = -\frac{mv_\parallel^2}{R^2}\mathbf{R}. \tag{2.19}$$

Taking this centrifugal force as an external force, the equations (2.15) can be applied to obtain the curvature drift.

$$\mathbf{v}_R = -\frac{mv_\parallel^2}{B^2R^2}\,\mathbf{R}\times\mathbf{B}. \tag{2.20}$$

In the absence of plasma current, $\nabla\times\mathbf{B}=0$, the ∇B drift goes into the same direction as the curvature drift and takes a similar form since there is a correlation between the field gradient and the curvature radius R

$$\frac{\mathbf{R}}{R^2} = -\frac{\nabla_\perp B}{B}. \tag{2.21}$$

Combining the equations (2.18), (2.20) and (2.21) leads to a total drift of the form,

$$\mathbf{v}_R + \mathbf{v}_{\nabla B} = \frac{m}{e}\frac{\mathbf{R}\times\mathbf{B}}{B^2R^2}(v_\parallel^2 + \frac{1}{2}v_\perp^2). \tag{2.22}$$

Taking an isotropic velocity distribution and $\varepsilon = \frac{1}{2}mv^2$, the resulting drift due to these two contributions is proportional to the particle energy

$$\mathbf{v} = \frac{4}{3}\frac{\varepsilon}{e}\frac{\mathbf{R}\times\mathbf{B}}{B^2R^2} \tag{2.23}$$

Collecting together the various drifts, described in this section, as [Morozov, 1966] shows, the guiding center drift velocity can be written as

$$\mathbf{v} = v_\parallel\hat{\mathbf{B}} + \frac{\hat{\mathbf{B}}}{eB}\times(mv_\parallel^2(\hat{\mathbf{B}}\cdot\nabla)\hat{\mathbf{B}} + \mu\nabla B + e\nabla\phi) \tag{2.24}$$

The first term in this expression clearly represents the parallel velocity of the guiding center along a field line,which will be studied in the following section, while the second term describes the perpendicular drift away from it. This second term may be considered to be made up of three separate parts, being the first one the perpendicular drift motion due to the curvature of the field lines. Particles following a curved field line experience a centripetal force which gives rise to a drift motion perpendicular to the instantaneous curvature vector and the magnetic field. The next term describes the so-called ∇B drift which occurs whenever the field strength varies. As the particle moves into a region of stronger or weaker field, its Larmor radius changes and its guiding center drifts accordingly. The final term in the above expression represents the so-called $\mathbf{E}\times\mathbf{B}$ drift.
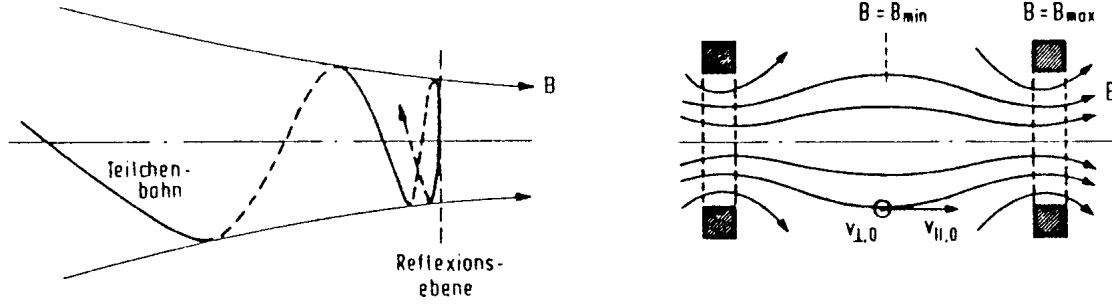
Figure 2.2: Mirror force scheme

2.1.4 Particle motion along B

Acceleration due to $E_\parallel$

A parallel electric field provides an acceleration given by

$$\frac{d}{dt}(mv_\parallel) = eE_\parallel \tag{2.25}$$

so that if $E_\parallel$ is a function of t, $v_\parallel$ is given by

$$mv_\parallel = e\int E_\parallel dt. \tag{2.26}$$

There are circumstances where the velocity resulting from such acceleration is relativistic. Therefore, if m_0 is the rest mass, the mass m is given by

$$m = m_0\gamma \quad where \quad \gamma = \frac{1}{\sqrt{1 - v^2/c^2}} \tag{2.27}$$

If $E_\parallel$ is a function of the distance $x_\parallel$ along the magnitude field and of time, it is necessary to solve the equation

$$\frac{d}{dt}\left(m\frac{dx_\parallel}{dt}\right) = eE_\parallel(x_\parallel, t) \tag{2.28}$$

Mirror Force

The existence of the mirror force is a direct consequence of the adiabatic invariance of μ . If a particle moves into a region of increased field strength, it's perpendicular velocity increases while it's parallel velocity decreases in order to keep μ and ε, the particle energy, constant. If the **B** field becomes strong enough, then the parallel velocity may be reduced to zero and then be reversed before the particle is accelerated in the direction of the weaker field, see Fig (2.2).

The force on the particle which leads to this motion is parallel to the magnetic field at the center of its gyro-orbit, and is given by the Lorentz formula:

20

$$\mathbf{F} = e(\ \mathbf{v} \times \mathbf{B}) \tag{2.29}$$

If the magnetic field is slowly varying, the component of this force, parallel to the field line at the guiding center of the orbit is

$$F = \alpha \cdot |e \cdot (\mathbf{v} \times \mathbf{B})| \tag{2.30}$$

where α is the small angle between the magnetic field at the position of the particle and that at the guiding center, the force is clearly in the direction of the weaker magnetic field.

Taking cylindrical coordinates with the z axis along the line of the guiding center motion and a radial coordinate r, the angle α is given by

$$\alpha = \frac{B_r}{B_z} \tag{2.31}$$

where B_r can be approached, using the Taylor formula, by

$$B_r \simeq \frac{\partial B_r}{\partial r}\rho, \tag{2.32}$$

being ρ the Larmor radius. Since $\nabla \cdot B = 0$ and $B_r \simeq r\partial B_r/\partial r$,

$$\frac{1}{r}\frac{\partial}{\partial r}(rB_r) = 2\frac{\partial B_r}{\partial r} = -\frac{\partial B_z}{\partial z}. \tag{2.33}$$

Taking $\frac{\partial B_z}{\partial z}$ at the guiding center,

$$\frac{\partial B_z}{\partial z} = |\nabla_{\parallel} B| \tag{2.34}$$

where $\nabla_{\parallel}$ is the gradient parallel to **B**. Taking $B_z = B$, from equations (2.31) and (2.34), the angle α is given by:

$$\alpha = \frac{1}{2}\rho\frac{|\nabla_{\parallel} B|}{B}. \tag{2.35}$$

From the force balance of the Larmor orbit

$$|\ e(v \times B)\ | = \frac{mv_{\perp}^2}{\rho} \tag{2.36}$$

and so, using equations (2.30), (2.35) and (2.36)the mirror force arising from $\nabla_{\parallel} B$ is therefore

$$F = -\frac{\frac{1}{2}mv_{\perp}^2}{B}\nabla_{\parallel} B. \tag{2.37}$$

If a magnetic field has a minimum along a field line, particles in this region of weaker field can be trapped between the two resulting mirrors. This resultant force is responsible for many processes in the universe, for example the Van Allen belt around the earth.

2.2 Tokamak Orbits

As seen before, a charged particle moving in an homogeneous magnetic field gyrates around a field line, and the guiding center of the particle's orbit moves with constant velocity along the magnetic field. The non-uniformity of the magnetic field leads to different drifts, which strongly influence the motion of the guiding center of the particle, especially curvature and ∇B drifts. In a toroidal system there are essentially two types of orbits, trapped and passing orbits. The transition from one to the other can be led by many causes. Particles which circulate continually round the torus are called *passing particles*. Particles whose parallel velocity vanishes at any point of their trajectory are called *trapped particles*. In tokamaks, two types of particles can be distinguished, since their parallel velocity has different signs compared with the plasma current (ASDEX Upgrade definition). Therefore, if the parallel velocity of the particles has the same sign as the plasma current, they are the so-called *co-going* particles, because if the velocities have the opposite sign than the plasma current, they are the so-called *counter-going* particles. The orbits of these two types of particles are different because of the drift sign.

The nature of the particle orbits in a tokamak plasma influences the physical properties of the plasma on a macroscopic scale, [Edegal, 2000]. The following cases are examples:

- Trapped particles do not contribute to the conductivity of a plasma but are responsible for bootstrap current;

- Current drive can be obtained by neutral beam injection into co- or counter-passing orbits;

- Due to finite orbit widths, the distribution function of fusion born α particles is anisotropic in velocity space.

The most interesting case is the large-trapped orbit of fast ions since they can strongly affect in different ways the plasma equilibrium, [Hsu, 1992]. They are becoming increasingly common as a results of auxiliary heating and in the near future due to fusion reactions (e.g., TFTR, [Grove, 1985] and JET, [Rebut, 1985]). The importance of the existence of these particles is two-fold:

1. If confined, their energy can be transferred to the background plasma, heating the bulk of the plasma;

2. As seen in previous section, they also may have destabilizing effects on the background plasma instabilities such as fishbones [Chen, 1984] or shear-Alfvén instabilities [Cheng, 1985].

2.2.1 Passing Orbits

Passing and trapped orbits lie on toroidally symmetric drift surfaces. Let d be the distance between the drift surface and the magnetic surface. For the passing case, this distance may be
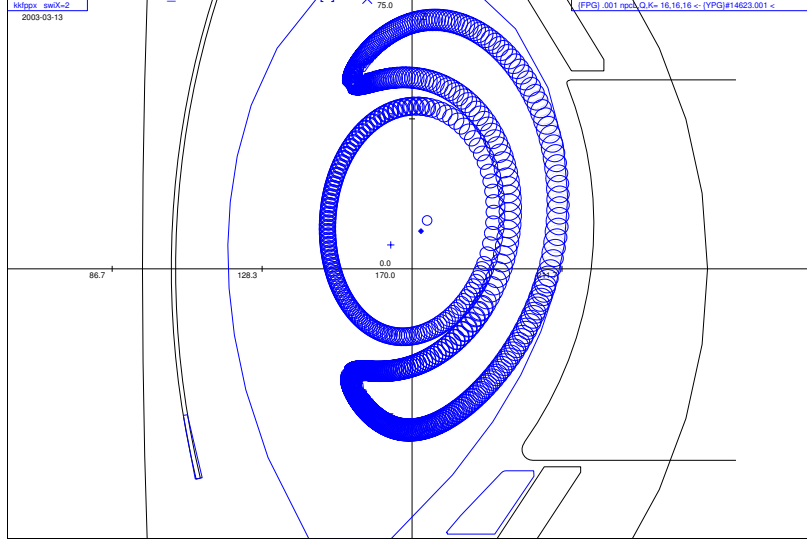
Figure 2.3: Trapped and passing orbits of a deuterium with 93 keV

calculated using the expression for the drift velocity.

The drift surfaces of passing particles may be determined by two components of the particle motion. The first one is the motion parallel to the magnetic field, giving rise to a poloidal rotation. For particles which are strongly passing, this rotation has a frequency of $\omega = (B_\theta/B)v_\parallel/r$ [Wesson, 1997]. The second component is the vertical drift due to the gradient and curvature of the toroidal field as given by equation (2.22), that is

$$v_d = \frac{m(v_\parallel^2 + \frac{1}{2}v_\perp^2)}{eRB_\phi} \qquad (2.38)$$

Combining these motions the equations for the drift orbit are

$$\frac{dR}{dt} = \omega z, \qquad \frac{dz}{dt} = -\omega(R - R_c) + v_d \qquad (2.39)$$

where z is the vertical coordinate and R_c is the R coordinate of the center of the cross-section of the magnetic surface.

The resulting equation for the drift surface is

$$\left(R - R_c - \frac{v_d}{\omega}\right)^2 + z^2 = constant. \qquad (2.40)$$

It represents a circular surface displaced from the magnetic surface by a distance

$$d = \frac{-v_d}{\omega} \simeq -\frac{r}{R}\frac{v_\parallel}{\omega_\theta} \qquad (2.41)$$

where $\omega_\theta = \frac{eB_\theta}{m}$.

23

2.2.2 Trapped Orbits

The responsible force of the trapped orbits is the mirror force, which is given by the equation (2.37). This force appears only when a particle is moving into a magnetic field of increasing magnitude. Since, in a tokamak, the magnetic field is a function of 1/R, particles which are on the outer side of the torus and are moving to the inner side, may undergo a magnetic mirror reflection. Only particles with a small parallel velocity suffer this effect. In absence of collisions and instabilities, the particles are trapped in the low field region, suffering repeated reflections.

Since μ is a constant of motion, the criterion for particle trapping can be calculated using this condition. Taking the maximum and minimum value of the magnetic field along the trapped orbit, and denoting the velocity at this point by a subscript zero, the constancy of μ gives

$$\frac{v_\perp^2}{B_b} = \frac{v_{\perp 0}^2}{B_{min}} \tag{2.42}$$

At the bounce point, $v_\parallel = 0$, and from the conservation of the energy

$$v_\perp^2 = v_{\perp 0}^2 + v_{\parallel 0}^2 \tag{2.43}$$

equation (2.42) becomes

$$\frac{B_b}{B_{min}} = 1 + \left(\frac{v_{\parallel 0}}{v_{\perp 0}}\right)^2. \tag{2.44}$$

The requirement then for trapping, given an initial value of $v_{\parallel 0}/v_{\perp 0}$ at the midplane, is that the magnetic field of the particle along its motion reaches the B_b value. That means that the particles have velocities lying within the cone of velocity space, so that satisfying the equation

$$\frac{v_{\parallel 0}}{v_{\perp 0}} < \left(\frac{2r}{R_0 - r}\right)^{1/2}. \tag{2.45}$$

Such relationship between $v_{\parallel 0}$ and $v_{\perp 0}$ is given by the so-called pitch angle, $v_\parallel/v_{total}$, and is one of the most important parameter in the study of particle trajectories in magnetic fields. Once the particle is trapped, its orbit may be calculated using the equation

$$F = -\mu \nabla_\parallel B, \qquad where \qquad \mu = \frac{\frac{1}{2}mv_\perp^2}{B} \tag{2.46}$$

Writing the major radius coordinate of the particle $R = R_0 + \cos\theta$, the parallel gradient of the magnetic field, dB/ds, may be obtained using

$$B = B_0 \frac{R_0}{R} = \frac{B_0}{1 + (r/R_0)\cos\theta} \tag{2.47}$$

which for *strongly trapped particles* $\theta = \frac{v_\parallel}{v_\perp} \ll 1$ gives

$$\frac{dB}{ds} = \frac{rB_0}{R_0} \frac{d\theta^2/2}{ds}. \tag{2.48}$$

The equation of a field line is $rd\theta/ds = B_\theta/B$ and so $\theta = (B_\theta/rB)s$. Therefore substituting equation (2.48) into equation (2.46) the equation of motion is

$$\frac{d^2s}{dt^2} = -\omega_b^2 s \tag{2.49}$$

where the bounce frequency is

$$\omega_b = \frac{v_\perp}{qR_0} \left(\frac{r}{2R_0} \right)^{1/2} \tag{2.50}$$

with $q = rB_0/R_0B_\theta$. The solution of equation (2.49)is clearly an oscillation given by:

$$s = s_b \sin \omega_b t. \tag{2.51}$$

Since $\theta = (B_\theta/rB)s$, the θ component of the motion is given by

$$\theta = \theta_b \sin \omega_b t. \tag{2.52}$$

The turning point θ_b is obtained using the equation (2.44) for the bounce condition. For $\theta_b \ll 1$, equation (2.47) gives

$$\theta_b = \frac{v_{\|0}}{v_{\perp 0}} \left(\frac{2R_0}{r} \right)^{1/2}. \tag{2.53}$$

The drift surface on which the trapped particle lies is now obtained by including the r component of the vertical drift due to the toroidal magnetic field as given by equation (2.38).
Taking $v_\perp \gg v_\|$, this drift is almost constant $v_d = \frac{1}{2}mv_\perp^2/qRB_\phi$ and its radial component is

$$\frac{dr}{dt} = v_d \sin\theta \simeq v_d\theta \tag{2.54}$$

Deriving equation (2.52) gives

$$\frac{d\theta}{dt} = \omega_b\theta_b \left(1 - \left(\frac{\theta}{\theta_b} \right)^2 \right)^{1/2}. \tag{2.55}$$

Therefore, the differential equation of the drift surface is

$$\frac{dr}{d\theta} = \frac{v_d}{\omega_b\theta_b} \frac{\theta}{\left(1 - \left(\frac{\theta}{\theta_b} \right)^2 \right)^{1/2}}. \tag{2.56}$$

25

Integrating the previous equation leads to the equation of the drift surface

$$(r - r_0)^2 = \left(\frac{\theta_b v_d}{\omega_b}\right)^2 \left(1 - \left(\frac{\theta}{\theta_b}\right)^2\right). \tag{2.57}$$

This equation represents a curve with the shape of a banana as shown in Fig(2.3). The half-width, $\triangle r$, of the orbit is

$$\triangle r = \frac{\theta_b v_d}{\omega_b} = \frac{v_{\|0}}{\omega_\theta} \tag{2.58}$$

where $\omega_\theta = eB_\theta/m$, therefore $\triangle r$ is equal to the Larmor radius calculated for a particle of velocity $v_{\|0}$ using the poloidal magnetic field B_θ. Since

$$B_\theta = \frac{\varepsilon}{q} B_\phi, \quad and \quad v_{\|0} = \varepsilon^{1/2} v_T \tag{2.59}$$

the $\triangle r$ becomes

$$\triangle r = \frac{q}{\varepsilon^{1/2}} \rho_l \tag{2.60}$$

with $\rho_l = \frac{v_T m}{eB_\phi}$, being v_T the thermal velocity.
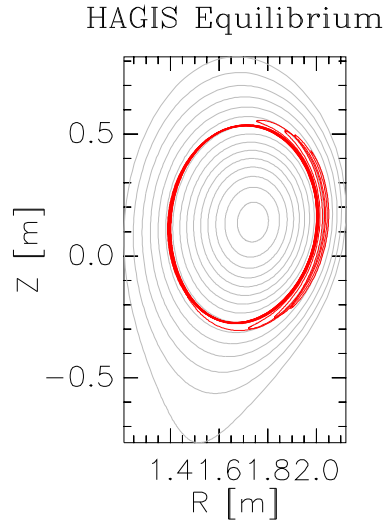

Figure 2.4: Transition from passing to trapped orbit due to collisions

2.3 Collisions

In order to have a full description of the behavior of fast ions and their confinement, a depth study of the diffusion mechanisms has to be taken into account.

The dependence of the diffusion coefficient on the collision frequency is shown in Fig.(2.5). The region $\nu_{eff} > v_T/Rq$ is called the *MHD region* or *collision region*, where v_T is the thermal velocity. The region $v_T/Rq > \nu_{eff} > \varepsilon^{3/2}v_T/Rq$ is the *plateau region* or the *intermediate region*; and the region $\varepsilon^{3/2}v_T/Rq > \nu_{eff}$ is the *banana region* or the *collisionless region*. Where the bounce frequency was taken as
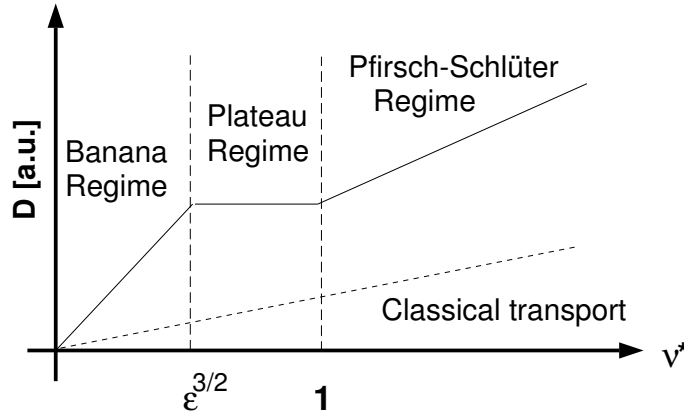

Figure 2.5: Different Collisional Regimes

$$\omega_b \simeq \frac{\varepsilon^{3/2}v_T}{qR} \tag{2.61}$$

These diffusion processes are collectively called *neoclassical diffusion*, [Miyamoto, 1989]. The study here presented is limited to the banana region, since fast ions have so high energy that the previous factor is , by far, lesser than $\varepsilon^{3/2}$. For ASDEX Upgrade, typical fast ion values, T=100 keV, R=1.65 m, q=4, this factor results in

$$\frac{\nu_i Rq}{v_T} \sim 10^{-7} \ll \varepsilon^{3/2} \tag{2.62}$$

and even for a density of $n = 10^21m^{-3}$, the collisionality still is low enough.

2.3.1   Banana Region

When a small collisionality is allowed, the trapped particles dominate the transport. When the collisionality is sufficiently low that particles complete at least one bounce orbit before suffering a collision, Fig.(2.4), the plasma is said to be in the banana regime. Collisions give rise to the diffusion of these particles in velocity space, they will then go out of the trapping

cone. The condition for collisions to prevent trapping is that the detrapping time be shorter than the bounce time ω_b^{-1}. This transition requires collisional diffusion in velocity space through an angle $\triangle\theta \sim \varepsilon^{1/2}$ and so the effective collision frequency for detrapping is $\nu/(\triangle\theta)^2 \sim \nu/\varepsilon$, where ε is the inverse aspect-ratio of the magnetic surface and therefore varies across the plasma radius. Thus the banana regime requirement becomes

$$\nu \ll \frac{\varepsilon^{3/2} v_T}{qR} \tag{2.63}$$

The collisions which scatter the particles out of their trapped orbits displace the particles across the flux surface by a distance $\sim \triangle r$, the banana width. This provides the step length for the diffusion process. Because of the banana width step length and the effective collision frequency, an estimate value of the diffusion could be

$$D \sim \triangle r^2 \nu_{eff} \qquad where \qquad \triangle r = \left(\frac{q}{\varepsilon^{1/2}}\right) \cdot \rho_l \quad and \quad \nu_{eff} = \frac{\nu_i}{\varepsilon} \tag{2.64}$$

But only a fraction, $\varepsilon^{1/2}$, of the particles are trapped and so the effective banana regime diffusion coefficient becomes

$$D \sim \frac{q^2}{\varepsilon^{3/2}} \nu_i \rho_l^2. \tag{2.65}$$

where q is the safety factor, $\varepsilon = r/R$ is the inverse aspect ratio, ν_i is the ion collision frequency and ρ_l the Larmor radius.

Actually, the calculation of the transport coefficients is much more complicated than the suggested above. A detailed study of the transport mechanisms was carried out using the HAGIS-Code improved with the Fokker-Planck collision operator.

Chapter 3

The NBI Spectra

3.1   Introduction

In chapter 1 it was shown that the reaction $D + T \rightarrow^4 He + n + 17.6\text{MeV}$ will be most likely used in a fusion reactor because it has the highest cross-section at the lowest energies. In this case the required central plasma temperature to ignite the fusion plasma is about 20keV and thus much higher than what occurs during plasma start-up in tokamaks. Therefore, some additional heating is required to raise the plasma temperature until the fusion reaction supplies the necessary heating. Some heating methods have been found to be particulary suitable to heat a fusion plasma to a sufficiently high temperature. The most used heating schemes at present are: Ohmic heating, electromagnetic wave heating, and neutral beam injection (NBI) heating. The last one was deeply studied in this work, since it generates the fast ion distribution [Staebler, 1999].

3.2   The NBI Scheme in ASDEX Upgrade

A brief description of the NBI-scheme is now here presented. The neutral beam injection heating consists of injecting a beam of neutral fuel atoms at high energy into the plasma.

In the plasma the beam atoms are ionized through ionization by electrons (dominant only at low electron temperatures of 1 keV), charge exchange (dominant process below 90 keV for deuterium beam), and ionization by ions (dominant process above 90 keV for deuterium beam). In total, these different processes lead to an approximately exponential decay of the beam neutral density along its path.

The energetic neutral atoms are created by extracting positive ions from suitable ion sources, accelerating the ions to the high energies, and finally neutralizing the energetic ions by collisions with a gas target in the so-called neutralizer. However, not only protons or deuterons are created in the ion source, but also the hydrogen or deuterium molecular ions H_2^+ and H_3^+ or D_2^+ and D_3^+ respectively. These molecular ions are also extracted, accelerated and dissociated in the neutralizer. Hence, the final neutral beam consists not only of neutral atoms with the full
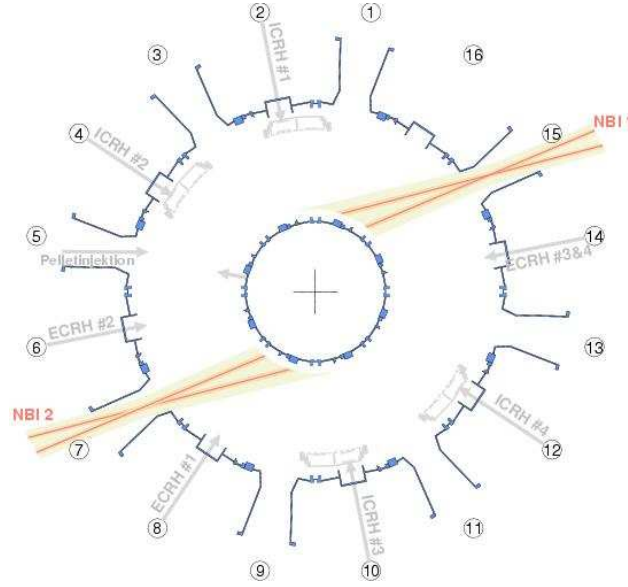
Figure 3.1: NBI overview in ASDEX Upgrade.

acceleration energy, but also of neutral atoms with the half and the third energy. After passing through the magnet, which reflects the non-neutralized ions, the neutral atoms are injected into the plasma through the duct between the beam lines and the torus vessel. The NBI system of ASDEX Upgrade consists of two beam lines. Each beam line is equipped with four ion sources. The sources of the first beam line is routinely operated at 55 kV for hydrogen (H^0) and 60 kV for deuterium (D^0), respectively. The sources of the second beam line are upgraded for operation at 70 kV for hydrogen and 100 kV for deuterium respectively. A total power of 14 MW H^0 and 20 MW D^0 can be injected in the ASDEX Upgrade torus.

The species and power distributions of these species depend on the special conditions in the ion source. Different plasma generating methods lead to different electron temperatures and density profiles in the ion source which influence the species distribution. Typical mean electron energies in a RF source are about 10 eV.

The injection geometry of both beam lines in a top view is shown in Fig.(3.1). A poloidal view is shown in Fig.(3.2).

3.3 FAFNER-Code, Numerical Simulation of NBI Spectra

3.3.1 Structure of the Code

FAFNER code is a computer program designed to model neutral beam injection into 3-D plasmas. The beam line section of the code provides a source function of coordinates of neutral particles in the velocity space as well as in the real space which is used to determine the initial ionization of the neutrals in the plasma. Plasma temperatures and densities are defined to be constant on flux surfaces, the magnetic field configuration is supplied for the
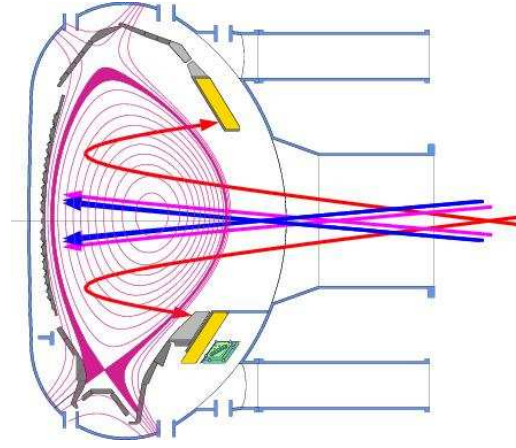
Figure 3.2: NBI Poloidal view

specific discharge. First, we have to define the beam lines used to inject neutral atoms into the plasma, which will provide a source of neutrals to use later in the code to compute power deposition profiles in the plasma, that will permit a detailed simulation of the power loading on scrapers along the beam line due to collisions with escaping neutrals.

The initial positions and directions of fast atoms emerging from the neutral beam source are chosen using the Monte Carlo techniques, appropriate to the provided input data. Then, it is calculated which of these particles reach the plasma and which are lost due to collisions with scrapers and ducts along the beam line. Initial conditions for the calculation of the fast ion deposition profile are supplied by the distribution of neutral atom generated in the source and computed in the beam line section. A Monte Carlo algorithm is then used to compute the deposition in the plasma in which the atom is ionized, either by ion or electron impact ionization or by charge exchange with plasma ions. The computation of mean free paths for these processes is made for each of the relevant injected energy species.

3.3.2   Description of Physics in Code

The NBI Scheme in FAFNER

A N_T number of beam lines are assumed, each containing n_s neutral beam sources with a total number n_B of sources available to heat the plasma. Neutral particles are assumed to emerge from a planar surface with a rectangular or circular shape. The code provides an option to supply details of the ion source. In the case where one of the isotopes of the H is to be injected, three species of ion H^+, H_2^+ and H_3^+, different energies, are emitted from the source with different power fractions, p_1, p_2 and p_3. A fraction η_k with $k = 1, 3$ of these ions are dissociated and neutralized into H atoms with energies T, T/2 and T/3 respectively, where T (eV) is the energy of ions leaving the ion source. As seen in the previous section, the angle formed by the particle trajectory and the field lines, always governs the behavior of the particle, FAFNER calculates the so-called pitch angle. However, the definition of pitch angle varies in

many works, being here defined by the relationship,

$$\Upsilon_{FAFNER} = \frac{v_\parallel}{v_{total}}. \tag{3.1}$$

Neutral Beam Ionization

The deposition of fast ions in the plasma due to interaction with neutral beams is governed by the equation

$$F(s) = \int f(\mathbf{x}_i, \mathbf{v}_i) e^{-\int_0^x \frac{dl}{\lambda(\mathbf{X}_p, \mathbf{V}_i)}} d\mathbf{x}_i d\mathbf{v}_i \tag{3.2}$$

where F(s) represents the flux of neutral particles crossing the flux surface s, $f(\mathbf{x}_i, \mathbf{v}_i)$ is the source function of neutral particles with space and velocity coordinates, $\mathbf{x}_i$ and $\mathbf{v}_i$ respectively, and λ is the total mean free path to collision for all ionization and charge-exchange processes, which is a function of $\mathbf{v}_i$ and of the plasma coordinates $\mathbf{x}_p$. The integral dl represents an integration along the path of each neutral particle from its origin point to its intersection with the flux surface s, at point x.

A representation of the source function $f(\mathbf{x}_i, \mathbf{v}_i)$ is computed in the beam line section of the code.

Cross Sections of Neutral Beam Collisions

In a uniform, pure hydrogen plasma of density n, the neutral beam of intensity I_0 is attenuated exponentially, along its direction x,

$$I = I_0 e^{-x/\lambda}, \tag{3.3}$$

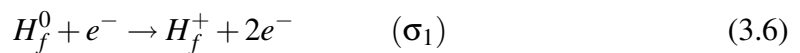where λ is the mean free path for ionizing collisions

$$\lambda = (n\sigma_\Sigma)^{-1}. \tag{3.4}$$

σ_Σ, the total trapping cross section, is the sum over all relevant rate coefficients

$$\sigma_\Sigma = \sum_{i=1}^3 \langle \sigma_i v \rangle v_b, \tag{3.5}$$

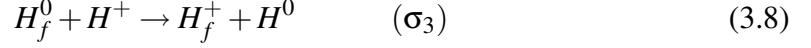with v_b being the beam velocity. σ_Σ is made of mainly three contributions:

- collisional ionization by electrons:

$$H_f^0 + e^- \rightarrow H_f^+ + 2e^- \qquad (\sigma_1) \tag{3.6}$$

- collisional ionization by plasma ions:

$$H^0_f + H^+ \rightarrow H^+_f + H^+ + e^- \qquad (\sigma_2) \qquad (3.7)$$

- charge exchange with plasma ions:

$$H^0_f + H^+ \rightarrow H^+_f + H^0 \qquad (\sigma_3) \qquad (3.8)$$

where the subscript 'f' denotes fast neutrals or ions, respectively.

A reasonable approximation for an energy per nucleon in the several 10 keV range is

$$\lambda = \frac{T}{18nA} \qquad (3.9)$$

with λ in meter, n in $10^{19}m^{-3}$, T in keV, and A, the atomic number in amu. A typical value for a 93 keV neutrals is $\lambda \sim 0.3m$.

The total cross section σ_Σ depends mainly on the energy per nucleon, with a small dependence on the electron temperature. Typical values for a purely hydrogenic plasma are $(13-15) \cdot 10^{-16}cm^2$ at 10 keV/amu, decreasing to about $3 \cdot 10^{-16}cm^2$ at about 80 keV/amu.

Computation of the Fast Ion Deposition Profiles

The computation of the equation (3.2) is explained here. A set of N_N neutral particle coordinates are selected from the source computed in the beam line code. The velocity coordinates are normalized and energy must be assigned to each neutral. This is done using the particle species fraction, p^n_k. A random number, ξ_1 is selected, and the energy E_i of the neutral is set, according to

$$p^n_1 > \xi_1 \qquad T_i = T \qquad (3.10)$$
$$p^n_1 < \xi_1 < p^n_1 + p^n_2 \qquad T_i = T/2 \qquad (3.11)$$
$$\xi_1 < p_1 + p^n_3 \qquad T_i = T/3. \qquad (3.12)$$

where E represents the injection energy of the beams. The smallest mean free path in the plasma, λ_{min} for each neutral injected species is computed, and then the neutral is advanced a distance

$$d = -ln(\xi_2)\lambda_{min} \qquad (3.13)$$

where ξ_2 is a random number. The atom is now located between the flux surfaces s_{j-1} and s_j and the probability that a collision occurs is

$$p = \frac{\lambda_{min}}{\lambda(s_j, \mathbf{v}_i)} \qquad (3.14)$$

33

where $\lambda(s_j, \mathbf{v}_i)$ is the total collision mean free path, given by the equation (3.4) on the flux surface s_j for an atom with velocity v_i.

The details of all particles are then summarized by the quantities H(s) and f_s, where f_s is the total energy loss due to neutrals failing to ionize and H(s) is defined such that

$$\frac{1}{V_p} \int H(s)dV = 1 - f_s \qquad (3.15)$$

where the integral is over the whole plasma volume. Therefore the deposition profile H(s) is a function of the flux coordinate s.

3.3.3 Results

The ionization pattern of a beam of the second neutral beam injector of ASDEX Upgrade was simulated considering only one specie in the source with the parameters corresponding to a specific real discharge. Two different magnetic field equilibrium were used during this work, one for the simulation of counter-injected particles (16095@3.10s) and the other for co-injected particles (15839@4.45s). However, most of the final results here presented are computed for the co-injected configuration, since it is more common in a typical ASDEX Upgrade discharge. The input data given in FAFNER were the following: The electron density was considered to be zero outside the separatrix in order to avoid the existence of fast ions in such region, since HAGIS can only calculate inside the last closed flux surface. In order to deeply study the trajectories of fast ions, only deuterium with 93 keV was considered. The ionization profile was calculated for 10.000 ions with the geometry of the beam number 5 of ASDEX Upgrade. The results for the initial distribution for the rest of the calculations are presented in the following pictures. As shown in Fig.(3.3), the ionization profile decays with the R coordinate as expected from the equation (3.3),that means the most particles are ionized just after they enter into the plasma.

The location of the beam in the toroidal direction can be observed in the ionization pattern shown in Fig.(3.4). Most of the atoms are ionized in a certain toroidal angle, constituting the largest branch. The other branch appears because some atoms of the neutral beam go through the first section of the plasma and are ionized in the second one, as shown Fig.(3.5). That occurs only if the beam is injected tangential to the torus. In other way the particles which form the second branch collide with the intern wall of the vessel. In the z-direction, the distribution is centered around z=-10 cm, where the beam is injected, as shown in a poloidal view of the beams, see Fig.(3.2).

The ionization distribution in the pitch angle is not uniform as shown in Fig.(3.6) and (3.7), since all particles enter into the plasma with almost the same direction and the same energy. It can be seen in Fig.(3.6) that the particles which are in the second branch have a certain pitch angle and that not all the particles with every pitch angle can go through the first section of the plasma. As shown in Fig.(3.7), the particles which are ionized at the beginning of the injection have a smaller pitch angle than the particles which reach the intern side of the plasma. This picture shows the trapped-passing boundary in ASDEX Upgrade. It can be seen that most
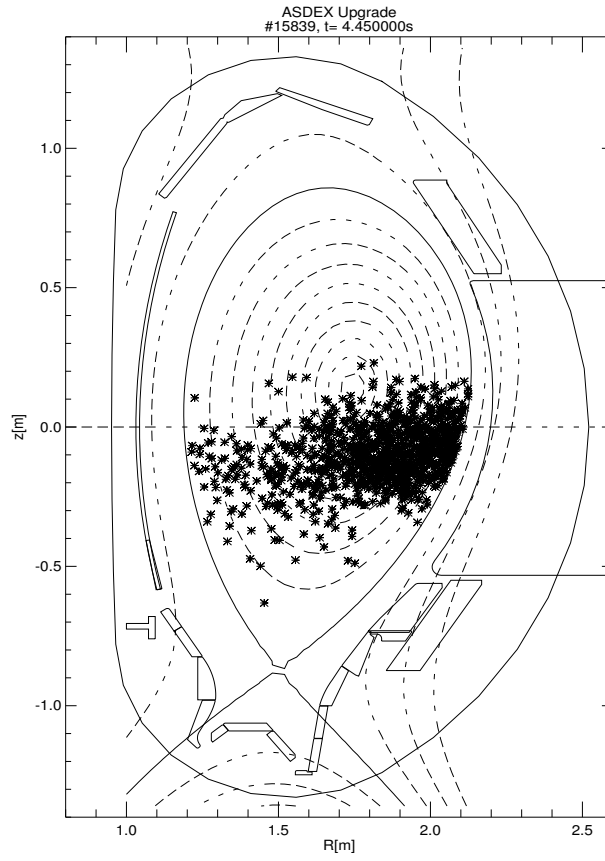
Figure 3.3: Simulation of the ionization pattern of the fifth beam of the second injector in ASDEX Upgrade. Only one specie with the full energy, 93 keV, was considered. Density of the background plasma n=8.4 $\cdot 10^{19} m^{-3}$.
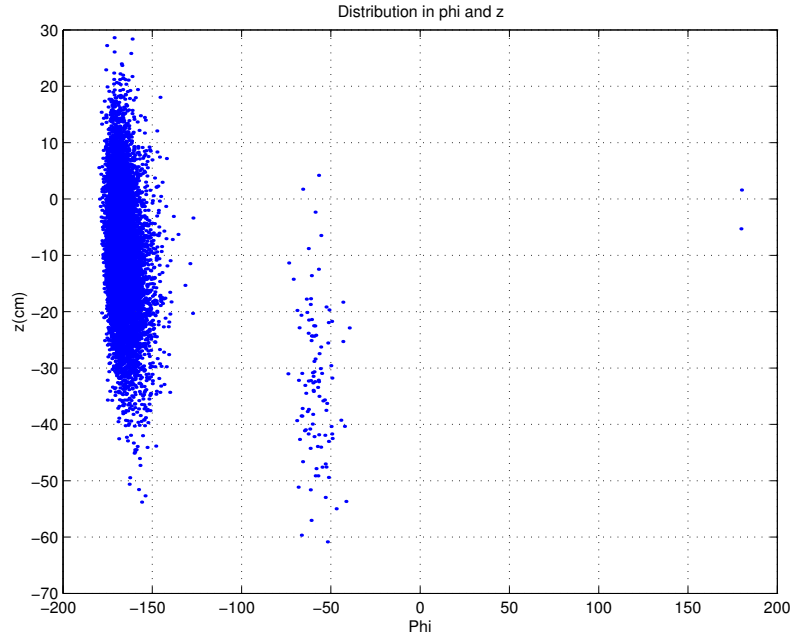
Figure 3.4: The two branches of the ionization distribution due to a tangential neutral beam injector in the plane formed by the toroidal coordinates ϕ and z .

particles are generated on trapped orbits. Using other injector or other beam geometry, the fraction of trapped particles is different.

Due to all the particles, which are ionized, have the same energy, the parallel and perpendicular components of the velocity lie on the circumference of radius $v_{total} = 2.99 \cdot 10^6 m/s$ which is the velocity of a deuterium with 93 keV. The initial distribution of the velocities is shown in Fig. (3.8) where the analytical circumference of radius $R = 2.99 \cdot 10^6$ is also plotted.
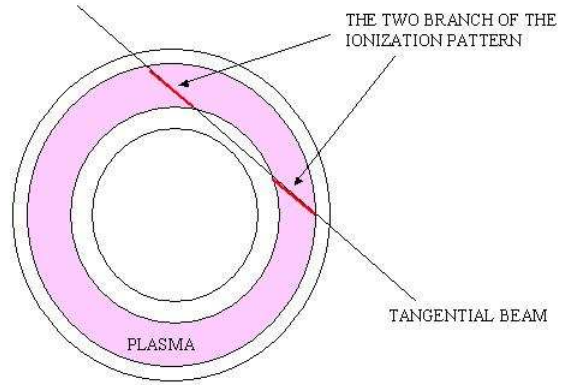
Figure 3.5: Illustration of the formation of two branches in the ionization pattern.
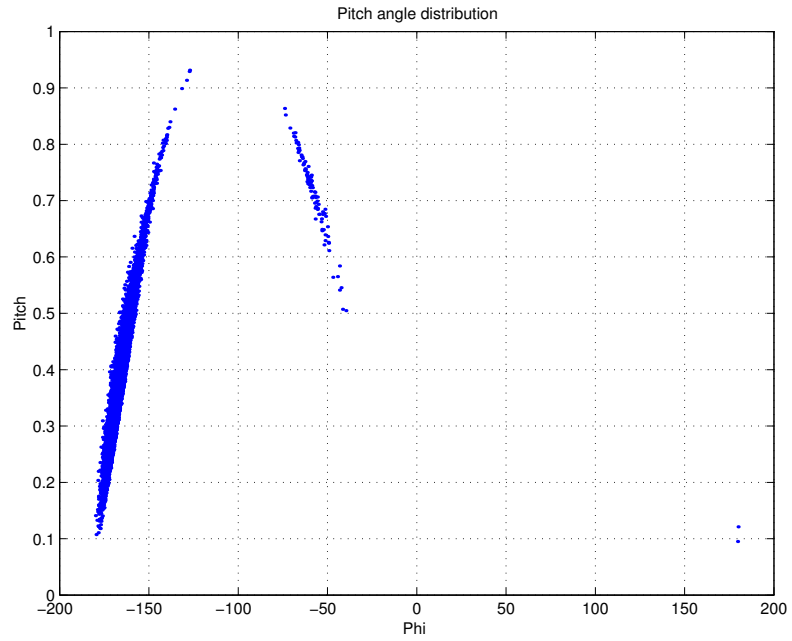

Figure 3.6: Pitch angle distribution in the ϕ direction of all co-injected particles. Pitch angle distribution in both branches.
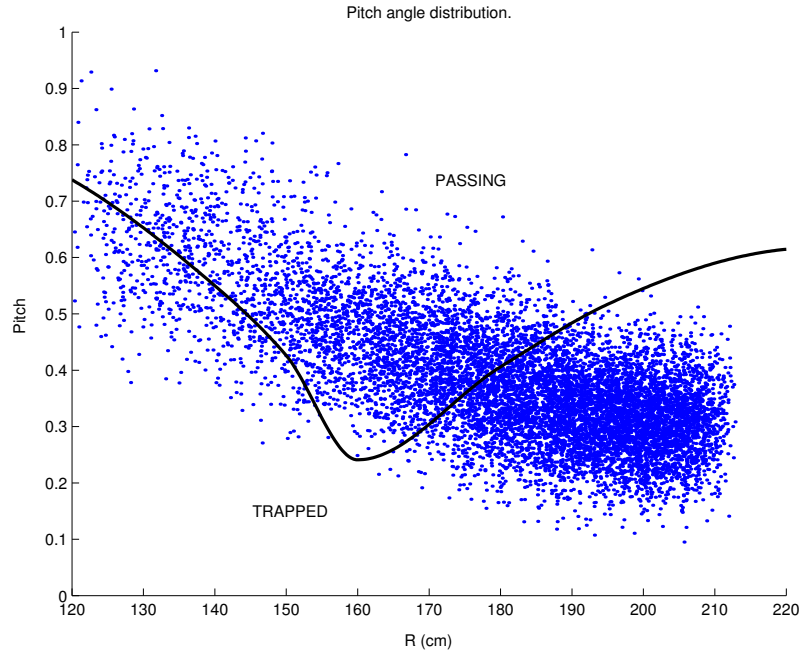
Figure 3.7: Pitch angle distribution in the radial direction.Pitch angle of each ionized particle and its radius. The passing-trapped boundary was fitted using a hermite polynomial.
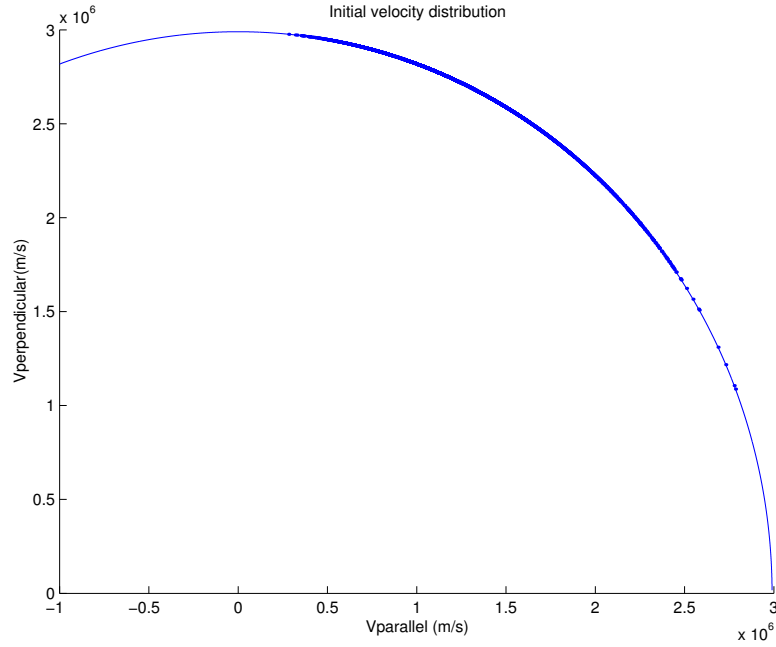

Figure 3.8: Initial velocity distribution of the ionized particles with the circumference of radius $2.99 \cdot 10^6$.

Chapter 4

HAGIS-Code

4.1 Introduction

The following description of the HAGIS-code follows the original work, which was carried out by [Pinches, 1996]. The study of trajectories of low energy background ions, which are frozen in the magnetic field, is well described by the magnetohydrodynamic approach (MHD), but for high energetic particles, these trajectories do significant excursions away from the magnetic field lines. In that case, ion motion has to be described using the guiding center approximation in which their parallel and perpendicular motion to the field lines are studied individually. A real magnetic configuration was taken from a specific discharge in ASDEX Upgrade. Together with the perturbation, this unperturbed magnetic field is the responsible for determining the particle orbits. In order to simplify the problem, the most suitable coordinate system was taken. The total field structure is in HAGIS represented as the superposition of a real magnetic configuration of a standard discharge, and a small electromagnetic perturbation representing the MHD-mode. In toroidal geometry, due to the periodicity in the toroidal and poloidal directions, each mode can be naturally decomposed into its Fourier components. In consequence, the spatial structure of the mode is here given by means of its toroidal and poloidal harmonic.

4.1.1 Particle Motion in Toroidal Magnetic Devices; Boozer coordinates

Solving any problem in Physic implies first to choose the most suitable coordinates system for the configuration. As shown in Fig. (1.3), for axisymmetric equilibria, the magnetic field lines lie in nested toroidal magnetic surfaces. From the equation of the equilibrium $\nabla p = \mathbf{j} \times \mathbf{B}$, there follows

$$\mathbf{B} \cdot \nabla p = 0 \tag{4.1}$$

$$\mathbf{j} \cdot \nabla = 0. \tag{4.2}$$

Then $\mathbf{j}$ and $\mathbf{B}$ lie in the magnetic surfaces of constant pressure. In this case, natural coordinates for a toroidal system are the so called flux coordinates. For non-circular, Shafranov-shifted flux
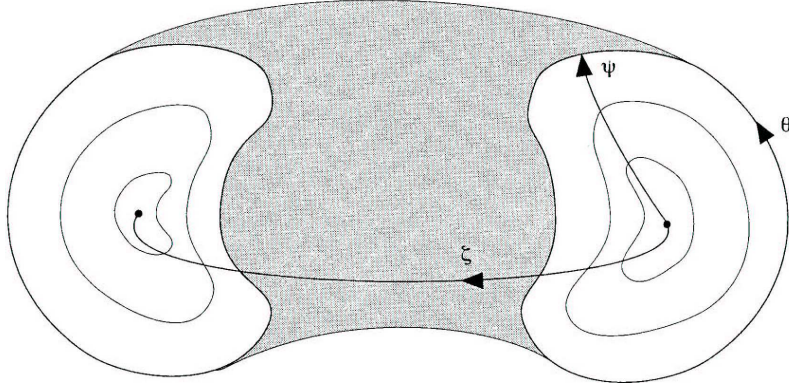
Figure 4.1: Set of toroidal coordinates used in HAGIS.

surfaces, the choice of these flux coordinates is not obvious, being one of these coordinates usually denoted by ψ, a constant over each flux surface. The other two coordinates form a grid within each surface, see Fig.(4.1). This set of coordinates forms a natural system because they allow to separate the rapid motion of the particle along the field line from the slow drift across the flux surface, since charged particles and field lines are closely tied. This enables the description to be characterized by the flux label ψ. The most suitable system of coordinates, in order to represent this description, was first used by Boozer [Boozer, 1981].

Giving the flux coordinates in a general form, a solenoidal field in a toroidal domain may be given by

$$\mathbf{B} = \nabla\psi \times \nabla\theta + \nabla\zeta \times \nabla\psi_p(\psi,\theta,\zeta) \tag{4.3}$$

where ψ denotes the toroidal flux, and ψ_p the poloidal flux

$$\psi = \frac{1}{2\pi}\int \mathbf{B}\cdot d\mathbf{s}_t \tag{4.4}$$

$$\psi_p = -\frac{1}{2\pi}\int \mathbf{B}\cdot d\mathbf{s}_p \tag{4.5}$$

with $\mathbf{B}$ the total magnetic field, $d\mathbf{s}_t$ a closed surface with its unitary vector in the toroidal direction and $d\mathbf{s}_p$ a closed surface with its unitary vector in the poloidal direction.

If the field has perfect surfaces, one can chose ψ, θ and ζ so that ψ_p is a function of ψ alone. However, if the field has a so complex topology that it can not be described by a set of nested flux surfaces, ψ_p must be considered as a function of all three coordinates. Therefore the field lines are given by

$$\frac{d\psi}{d\zeta} = \frac{\mathbf{B}\cdot\nabla\psi}{\mathbf{B}\cdot\nabla\zeta}, \qquad \frac{d\theta}{d\zeta} = \frac{\mathbf{B}\cdot\nabla\theta}{\mathbf{B}\cdot\nabla\zeta}, \tag{4.6}$$

while taking into account equation (4.3), become

$$\frac{d\psi}{d\zeta} = -\frac{\partial \Psi_p}{\partial \theta}, \qquad \frac{d\theta}{d\zeta} = \frac{\partial \Psi_p}{\partial \psi}, \tag{4.7}$$

If the magnetic field has a continuous symmetry such as toroidal symmetry, the field lines reduce to an integrable Hamilton form. Therefore, in the previous equation, $\Psi_p(\psi, \theta, \zeta)$ can be identified as the field line Hamiltonian, being θ, ψ and ζ, analog to position, momentum and time respectively.

Taking the specific Boozer coordinate system used by White and Chance [White, 1984], ψ_p is taken as the radial coordinate and we deform the toroidal and poloidal angle coordinate ζ and θ to obtain straight field lines. The general poloidal angle was chosen by selecting a specific form for the Jacobian to obtain a covariant representation of the magnetic field in which the angular components are functions of the poloidal flux alone.

Therefore, the covariant form for $\mathbf{B}$ may be written as

$$\mathbf{B} = B_{\psi_p}\nabla\psi_p + B_\theta\nabla\theta + B_\zeta\nabla\zeta, \tag{4.8}$$

The ζ and θ contravariant components of the field may be calculated, taking into account that the local helicity $(\mathbf{B}\cdot\nabla\zeta)/(\mathbf{B}\cdot\nabla\theta) \equiv B^\zeta/B^\theta$ is independent of θ.

And the contravariant form of $\mathbf{B}$ may now be written as

$$\mathbf{B} = \nabla\zeta \times \nabla\psi_p + q\nabla\psi_p \times \nabla\theta = \nabla\nabla(\zeta - q(\psi_p)\theta) \times \nabla\psi_p. \tag{4.9}$$

where $q\nabla\psi_p = \nabla\psi$, also $q = \frac{d\psi}{d\psi_p}$.

From this equation, the vector potential $\mathbf{A}$ may be written as

$$\mathbf{A} = \psi\nabla\theta - \psi_p\nabla\zeta. \tag{4.10}$$

Let δ be the radial covariant component of $\mathbf{B}$, the covariant representation then becomes

$$\mathbf{B} = \delta(\psi_p, \theta)\nabla\psi_p + (\mathcal{J}B^2 - qg)\nabla\theta + g(\psi_p)\nabla\zeta, \tag{4.11}$$

where $\mathcal{J}$ is the jacobian, if it is chosen to be of the form $\mathcal{J} = \mathcal{F}(\psi_p)/B^2$, B_θ is then a flux function since $B_\theta = \mathcal{F}(\psi_p) - g(\psi_p)q(\psi_p) \equiv I(\psi_p)$. Therefore, the final covariant form becomes,

$$\mathbf{B} = \delta(\psi_p, \theta)\nabla\psi_p + I(\psi_p)\nabla\theta + g(\psi_p)\nabla\zeta, \tag{4.12}$$

where

$$\mathcal{J} = \frac{I + gq}{B^2}. \tag{4.13}$$

and $I(\psi_p)$ and $g(\psi_p)$ may be interpreted in terms of the currents flowing in the device, being $2\pi I/\mu_0$ the total toroidal current inside the flux surface ψ_p and $2\pi g/\mu_0$ the poloidal current.

4.2 Guiding Center Equations

The equation of the guiding center motion is calculated here by means of a variational principle for guiding center motion, [Littlejohn, 1982].

Taking the Lagrangian of the system as

$$L = \frac{1}{2}mv^2 + e\mathbf{A} \cdot \mathbf{v} - e\Phi. \tag{4.14}$$

where $\mathbf{A}$ and Φ are the vector and scalar potential respectively and $\mathbf{v}$ is the particle velocity relative to the magnetic field in contravariant form.

Assuming the exact invariance of the magnetic moment, $\mu = mv_\perp^2/2B$, it becomes an 'internal' process analogous to electron spin and is coupled to the external degrees of freedom by means of the mirror force, $\mathbf{F}_m = -\nabla(\mu B)$. This suggest the interpretation of μB as a potential energy term rather than a kinetic one and allows the Lagrangian to be written in the form first given by Taylor. [Taylor, 1964],

$$L = \frac{1}{2}mv_\parallel^2 + e\mathbf{A} \cdot \mathbf{v} - \mu B - e\Phi. \tag{4.15}$$

Suitable canonical variables were initially presented in two works [White, 1984] and [White, 1982] using a rather laborious procedure. They tried to find the time variation of a particular coordinate, q_i say, while following the guiding center position. This meant demonstrating that $\dot{b}_i = \mathbf{v} \cdot \nabla q_i = \partial H/\partial p_i$, where the Hamiltonian H is the total energy of the system expressed in term of the canonical variables and $\mathbf{v}$ is the guiding center drift velocity given in equation (2.24). By adopting a Lagrangian approach, [Littlejohn, 1982]was able to considerably reduce the labour involved in finding a reduced set of guiding center canonical variables. The procedure used is based upon Hamilton's variational principle which may be written as

$$\delta \int L dt = 0, \tag{4.16}$$

with the guiding center Lagrangian given by [Littlejohn, 1982]

$$L = e\mathbf{A}^* \cdot \dot{\mathbf{x}} + \frac{m}{e}\mu\dot{\xi} - H, \tag{4.17}$$

where ξ is the gyro-phase and $\dot{\mathbf{x}}$ is the guiding center velocity and represents the total time derivative of the guiding center location, $\mathbf{x}$. The term $\mathbf{A}^* = \mathbf{A} + \rho_\parallel\mathbf{B}$ is known as the 'modified vector potential' and was first used by Morozov & Solov'ev in 1963 [Morozov, 1966]. It makes use of $\rho_\parallel = v_\parallel/\omega_{ci}$, which is referred to as the parallel gyroradius, with the Hamiltonian given by

$$H = \frac{1}{2}mv_\parallel^2 + \mu B + e\Phi. \tag{4.18}$$

It is convenient to choose units based around characteristic system quantities. Since the case being examined is the interaction of a distribution of fast particles with a perturbed magnetic

field, it is appropriate to express all masses and charges in terms of those of the fast particles and to express all lengths in terms of the toroidal major radius at the magnetic axis. Time units are specified in terms of the inverse fast particle cyclotron time at the magnetic axis, $1/\Omega_0 = 1/B_0$ in these units. Since we only consider a single species of fast particle we may subsequently omit all occurrences of charge and mass in the following formulae. Physical formulae consequently result by restoring these physical factors.

Canonical variables are obtained by substituting expressions for **A** and **B** into the equation (4.17) and rewriting it as

$$L = \sum_i p_i \dot{q}_i - H. \tag{4.19}$$

Once this form is obtained, the canonical momenta and coordinates can immediately be identified. Substituting equations (4.10) and (4.12) for **A** and **B** into the Lagrangian gives

$$L = (\rho_{\parallel} I + \psi)\dot{\theta} + (\rho_{\parallel} g - \psi_p)\dot{\zeta} + \mu\dot{\xi} - H + \delta\rho_{\parallel}\dot{\psi}_p \tag{4.20}$$

It is thus, natural to select the Boozer coordinates introduced in the previous section to form the canonical coordinates, enabling the canonical conjugate momentum variables to be read straight from equation (4.20). Upon closer inspection however there are seen to be four terms of the form $p_i \dot{q}_i$: ψ_p appears as a momentum term and consequently the final term interferes with this interpretation and must be removed.

One method of achieving this involves the observation that the equations of motion remain invariant under the addition of exact differential to the Lagrangian [Goldstein, 1980]. Therefore, terms such as $d(\delta\rho_{\parallel}\psi)/dt$ may be safely subtracted from equation (4.20) with no effect and the remaining terms absorbed into the canonical coordinates θ and ζ through their definition, or neglected if they are higher order in ρ [White, 1984] and [White, 1990]. This approach is unsatisfactory, however, since the resulting canonical coordinates no longer coincide with the Boozer magnetic coordinates derived above and also since the equations of motion do not exactly conserve H. A more desirable approach is one that while only reproducing particle motion to second order in ρ, exactly conserves the Hamiltonian. This is achievable by a modification of the guiding center velocity $\dot{\mathbf{x}} = \mathbf{v}$, so that $\mathbf{v} \to \mathbf{v} + \mathbf{w}$. This adds an additional term to equation (4.20) of the form $\mathbf{A}^* \cdot \mathbf{w}$, where **w** may be chosen such that

$$\mathbf{A}^* \cdot \mathbf{w} = -\delta\rho_{\parallel}\dot{\psi}_p. \tag{4.21}$$

With this choice the reduced set of canonical coordinates are θ, ζ and ξ, with the corresponding canonical momenta given by

$$
\begin{align}
P_\theta &= \rho_{\parallel} I + \psi, \tag{4.22}\\
P_\zeta &= \rho_{\parallel} g - \psi_p, \tag{4.23}\\
P_\xi &= \mu, \tag{4.24}
\end{align}
$$

and the equation of motion following from the Hamiltonian in the usual manner

$$\dot{\theta} = \frac{\partial H}{\partial P_\theta}, \qquad \dot{P}_\theta = -\frac{\partial H}{\partial \theta}, \tag{4.25}$$

$$\dot{\zeta} = \frac{\partial H}{\partial P_\zeta}, \qquad \dot{P}_\zeta = -\frac{\partial H}{\partial \zeta}, \tag{4.26}$$

$$\dot{\xi} = \frac{\partial H}{\partial P_\xi}, \qquad \dot{P}_\xi = -\frac{\partial H}{\partial \xi}. \tag{4.27}$$

Before proceeding to derive the equations of motion that follow from equations (4.25), (4.26) and (4.27), consider the inclusion of a general electromagnetic perturbation described by the vector and scalar potentials

$$\tilde{\mathbf{A}}(\mathbf{x},t) = \tilde{A}_{\psi_p}\nabla\psi_p + \tilde{A}_\theta\nabla\theta + \tilde{A}_\zeta\nabla\zeta, \quad and \quad \tilde{\Phi}(\mathbf{x},t). \tag{4.28}$$

Replacing then $\mathbf{A}$ with $\mathbf{A} + \tilde{\mathbf{A}}$, and Φ with $\Phi + \tilde{\Phi}$, means that the Lagrangian now becomes

$$L = (\rho_\parallel I + \psi + \tilde{A}_\theta)\dot{\theta} + (\rho_\parallel g - \psi_p + \tilde{A}_\zeta)\dot{\zeta} + \mu\dot{\xi} - H + (\delta\rho_\parallel + \tilde{A}_{\psi_p})\dot{\psi}_p. \tag{4.29}$$

The final term is treated as before and the canonical variables are now modified such that the canonical momenta are

$$P_\theta = \rho_\parallel I + \psi + \tilde{A}_\theta, \tag{4.30}$$

$$P_\zeta = \rho_\parallel g - \psi_p + \tilde{A}_\zeta, \tag{4.31}$$

$$P_\xi = \mu. \tag{4.32}$$

Examining these equations, it is easy to see that they are of the same structure as a free particle in classical electrodynamics for which the canonical momenta $\mathbf{P} = \mathbf{p} + \mathbf{A}$, where $\mathbf{p}$ is the known mechanical momentum. This is seen from equation (4.10) where it is observed that ψ and $-\psi_p$ are the θ and ζ covariant components of $\mathbf{A}$. Noting that $\rho_\parallel\mathbf{B}$ is the parallel momentum, it follows from equation (4.12) that the particle momenta corresponding to θ and ζ are $\rho_\parallel I$ and $\rho_\parallel g$ respectively.

The equation of motion may now be evaluated in accordance with equations (4.25), (4.26) and (4.27). The Hamiltonian of this system is the total energy and is therefore given by equation (4.18). Taking $\rho_\parallel$ as the normalized parallel velocity (since m=e=1 in the units adopted here)the Hamiltonian can be re-written as

$$H = \frac{1}{2}\rho_\parallel^2 B^2 + \mu B + \tilde{\Phi}. \tag{4.33}$$

Since H is not written in terms of the canonical momenta, this first involves evaluating the partial derivatives of ψ_p and $\rho_\parallel$ with respect to the canonical variables. Recalling that g, I and ψ

44

are all functions of ψ_p alone, equations (4.30), (4.31) and (4.32) give that $\psi_p = \psi_p(\theta, \zeta, P_\theta, P_\zeta)$ and that $\rho_\parallel = \rho_\parallel(\theta, \zeta, P_\theta, P_\zeta)$. Eliminating $\rho_\parallel$ from the first two of these equations gives

$$g(P_\theta - \psi - \tilde{A}_\theta) = I(P_\zeta + \psi_p - \tilde{A}_\zeta). \tag{4.34}$$

Differentiating this expression with respect to θ, ζ, P_θ and P_ζ is now possible to find the equations of motion from equations (4.25), (4.26)and (4.27) by making use of the chain rule, see [Pinches, 1996]. Although the equations for $\dot{\theta}$, $\dot{\zeta}$, $\dot{P}_\theta$ and $\dot{P}_\zeta$ which are obtained, describe completely the motion of the guiding center, they do not represent the easiest numerical scheme to implement since it is necessary to invert P_θ and P_ζ to obtain ψ_p and $\rho_\parallel$. A more practical approach is to evolve ψ_p and $\rho_\parallel$ directly by means of their time derivatives. The equations of motion are then

$$\dot{\theta} = \frac{1}{D}\left[\rho_\parallel B^2(1 - \rho_\parallel g' - \tilde{A}'_\zeta) + g\left((\rho_\parallel^2 B + \mu)B' + \tilde{\Phi}'\right)\right], \tag{4.35}$$

$$\dot{\zeta} = \frac{1}{D}\left[\rho_\parallel B^2(\rho_\parallel I' + q + \tilde{A}'_\theta) - I\left((\rho_\parallel^2 B + \mu)B' + \tilde{\Phi}'\right)\right], \tag{4.36}$$

$$\dot{\psi}_p = \frac{1}{D}\left[\left(I\frac{\partial \tilde{A}_\zeta}{\partial \theta} - g\frac{\partial \tilde{A}_\theta}{\partial \theta}\right)\dot{\theta} + \left(I\frac{\partial \tilde{A}_\zeta}{\partial \zeta} - g\frac{\partial \tilde{A}_\theta}{\partial \zeta}\right)\dot{\zeta} + g\dot{P}_\theta - I\dot{P}_\zeta\right], \tag{4.37}$$

$$\dot{\rho}_\parallel = \frac{1}{I}\left[\dot{P}_\theta - \frac{\partial \tilde{A}_\theta}{\partial \theta}\dot{\theta} - \frac{\partial \tilde{A}_\theta}{\partial \zeta}\dot{\zeta} - \frac{\partial \tilde{A}_\theta}{\partial t} - \left(q + \frac{\partial \tilde{A}_\theta}{\partial \psi_p} + \rho_\parallel I'\right)\dot{\psi}_p\right]. \tag{4.38}$$

with prime referring to differentiation with respect to ψ_p and

$$D = \rho_c[gI' - g'I] + I + qg. \tag{4.39}$$

To describe the path in real space, the vector function $\mathbf{x} = \mathbf{x}(\psi_p, \theta, \zeta)$ which allows the transformation to the inertial laboratory frame of reference, must be known. The given equations of motion may be simplified taking a particular form for the perturbed field instead of the general perturbation. Since a typical tokamak equilibrium is considered to be in low-β regime, as shown in [Pinches, 1996], $\delta B = 0$ and $E_\parallel = 0$. The first of these conditions places a constraint upon $\tilde{A}_\perp$ which can be encompassed by representing the perturbed magnetic field through the variable, $\tilde{\alpha}(\psi_p, \theta, \zeta, t)$ defined through the relation

$$\tilde{\mathbf{A}} = \tilde{\alpha}(\mathbf{x}, t)\mathbf{B}. \tag{4.40}$$

From this definition it can be seen that $\tilde{\alpha}$ is closely related to the parallel component of the perturbed vector potential and it follows that the resulting perturbation to the magnetic field is given by

$$\delta \mathbf{B} = \nabla \times (\tilde{\alpha}\mathbf{B}_0). \tag{4.41}$$

Since the electron parallel conductivity has a very large value, the electric field is perpendicular to the magnetic field. The condition that $E_{\parallel} = 0$ provides a relationship between $\tilde{\alpha}$ and the scalar potential $\tilde{\Phi}$:

$$E_{\parallel} = -\nabla_{\parallel}\tilde{\Phi} - \frac{\partial}{\partial t}(\tilde{\alpha}B_0) = 0. \tag{4.42}$$

Hence only one scalar field is required to describe the field perturbations arising from the MHD-mode present. Substituting for the covariant components of $\tilde{\alpha}\mathbf{B}$ into the above equations of motion produces the same expressions as used by White and Chance [White, 1984]:

$$\dot{\theta} = \frac{1}{D}\left[\rho_{\parallel}B^2(1 - \rho_c g' - g\tilde{\alpha}') + g\left((\rho_{\parallel}^2 B + \mu)B' + \tilde{\Phi}'\right)\right], \tag{4.43}$$

$$\dot{\zeta} = \frac{1}{D}\left[\rho_{\parallel}B^2(\rho_c I' + q + I\tilde{\alpha}') - I\left((\rho_{\parallel}^2 B + \mu)B' + \tilde{\Phi}'\right)\right], \tag{4.44}$$

$$\dot{\psi}_p = \frac{1}{D}\left[\rho_{\parallel}B^2\left(g\frac{\partial\tilde{\alpha}}{\partial\theta} - I\frac{\partial\tilde{\alpha}}{\partial\zeta}\right) - \left(g\frac{\partial\tilde{\Phi}}{\partial\theta} - I\frac{\partial\tilde{\Phi}}{\partial\theta} - I\frac{\partial\tilde{\Phi}}{\partial\zeta}\right) - g(\rho_{\parallel}^2 B + \mu)\frac{\partial B}{\partial\theta}\right], \tag{4.45}$$

$$\dot{\rho}_{\parallel} = \frac{1}{D}\left[\left(I\frac{\partial\tilde{\alpha}}{\partial\zeta} - g\frac{\tilde{\alpha}}{\partial\theta}\left((\rho_{\parallel}^2 B + \mu)B' + \tilde{\Phi}\right)\right) - (q + \rho_c I' + I\tilde{\alpha}')\frac{\partial\tilde{\Phi}}{\partial\zeta}\right] \tag{4.46}$$

$$+ \frac{1}{D}\left[(\rho_c g' - 1 + g\tilde{\alpha}')\left((\rho_{\parallel}^2 B + \mu)\frac{\partial B}{\partial\theta} + \frac{\partial\tilde{Phi}}{\partial\theta}\right)\right] - \frac{\partial\tilde{\alpha}}{\partial t}, \tag{4.47}$$

where $\rho_c = \rho_{\parallel} + \tilde{\alpha}$.

Given the equilibrium functions, g, I, q and B, and the perturbation parameter $\tilde{\alpha}$, particle trajectories may be accurately followed in the presence of a perturbation.

4.3   Fokker-Planck Collision Operator

In order to study the Neoclassical Transport mechanisms together with any instabilities, the Hagis-code was improved by computing the Fokker-Planck collision operator with the AS-DEX Upgrade parameters. The following algorithm was taken from the work of [Lin, 1995]. The numerical simulation of neoclassical transport based on the drift-kinetic formalism was carried out by [Tsang, 1975]. More recently, [Wu, 1993] used a hamiltonian guiding center Monte Carlo code to study the bootstrap current. [Ma, 1992] developed a particle simulation scheme using the conventional gyrokinetic algorithm and binary collisions. The present work is intended to improve the original Hagis code with the study of binary collisions simplifying the approach of [Lin, 1995]. Since only fast ion trajectories constitute the goal of this work, momentum and energy conservation in the whole system was not taken into account. That makes the algorithm significantly easier, since a δf model is not considered. Simulation results of the diffusion time in the banana regime are found to agree very well with the standard neoclassical theory, see section 4.5. Based on the approach adopted by Xu and Rosenbluth [Xu, 1991], an accurate collision operator is developed and implemented [Bergmann]. It was

proved that in the banana regime, the neoclassical enhancement of the viscosity is a Pfirsch-Schlüter factor times the classical viscosity.

The usual drift kinetic equation for a guiding center distribution function f(E,μ, **x**), where E is the particle kinetic energy, μ is the magnetic moment, and **x** is a guiding center coordinate has the form

$$\frac{\partial f}{\partial t} + (v_{\parallel}\hat{b} + \mathbf{v}_d) \cdot \frac{\partial f}{\partial \mathbf{x}} - C(f) = 0 \tag{4.48}$$

In dealing with collisions of test particles (α) with background particles (β), first the Rosenbluth potentials are taken, assumed both distribution functions f^{α} and f^{β} to be close to Maxwellian. The linearized operator is [Xu, 1991]

$$C(f^{\alpha}) = \frac{\partial}{\partial \mathbf{v}} \cdot (\mathbf{v}F f^{\alpha}) + \frac{1}{2}\frac{\partial^2}{\partial \mathbf{v}\partial \mathbf{v}} : [G(\mathbf{I}v^2 - \mathbf{v}\mathbf{v}) + H\mathbf{v}\mathbf{v}]f^{\alpha}, \tag{4.49}$$

where the first term is the test-particle drag and the second one is the diffusion term. Functions F, G and H are defined by

$$F = \left(1 + \frac{m_{\alpha}}{m_{\beta}}\right)\phi(x)\nu_{\alpha\beta}, \tag{4.50}$$

$$G = \left[\left(1 - \frac{1}{2x}\right)\phi(x) + \frac{d\phi(x)}{dx}\right]\nu_{\alpha\beta}, \tag{4.51}$$

$$H = \frac{1}{x}\phi(x)\nu_{\alpha\beta}, \tag{4.52}$$

respectively. Here $x = v^2/v_{th}^2$ and $\phi(x)$ is the Maxwellian integral defined by

$$\phi(x) = \frac{2}{\sqrt{\pi}}\int_0^x e^{-t}\sqrt{t}dt. \tag{4.53}$$

Since electrons and ions have a different mass, the study of their collisions with beam ions has to be made separately. The basic collision frequency here is defined for collisions between fast ions with background ions by

$$\nu_{ib} = \frac{ne^4 ln\Lambda}{8\pi\varepsilon_0^2 m_b^{1/2} T_0^{3/2}} \cdot \left(\frac{T_0}{T_b}\right)^{3/2} \tag{4.54}$$

and with electrons by

$$\nu_{eb} = \frac{ne^4 ln\Lambda}{8\pi\varepsilon_0^2 m_b^{1/2} T_0^{3/2}} \cdot \left(\frac{T_0}{T_b}\right)^{3/2} \cdot \left(\frac{m_e}{m_b}\right)^{5/2} \tag{4.55}$$

where n is the electron density, $ln\Lambda$ is the Coulomb logarithm, m_b is the fast ion mass, T_0 is the background energy and T_b is the fast ion energy.

The diffusion tensor can be diagonalized by transforming to the coordinate system $\mathbf{w}$ in which the z axis is the direction of the particle velocity, $\mathbf{w}_\| = \mathbf{w}_z = \mathbf{v}$. This leads to

$$C(f^\alpha) = \frac{\partial}{\partial w_\|}(vFf^\alpha) + \frac{1}{2}\frac{\partial^2}{\partial w^2}(v^2 H f^\alpha) + \frac{1}{2}\left(\frac{\partial^2}{\partial w_x^2} + \frac{\partial^2}{\partial w_y^2}\right)(v^2 G f^\alpha), \qquad (4.56)$$

where w_x and w_y are orthogonal to $w_\|$ and to each other. In the drift kinetic limit, velocity space coordinate may be transformed to cylindrical coordinate $(v_\|, v_\perp, \phi)$, with ϕ representing the gyroangle. After averaging over gyrophase ϕ, the operator becomes

$$C(f^\alpha) = \frac{\partial}{\partial v_\|}(\nu_{s\|}f^\alpha) + \frac{\partial^2}{\partial v_\perp^2}(\nu_{s\perp}f^\alpha) + \frac{\partial^2}{\partial v_\| \partial v_\perp^2}(\nu_{\|\perp}f^\alpha) \qquad (4.57)$$

$$+ \quad \frac{1}{2}\frac{\partial^2}{\partial v_\|^2}(\nu_\| f^\alpha) + \frac{1}{2}\frac{\partial^2}{(\partial v_\perp^2)^2}(\nu_\perp f^\alpha), \qquad (4.58)$$

where the collision coefficients are

$$\nu_{s\|} = v_\| F, \qquad (4.59)$$
$$\nu_{s\perp} = 2v_\perp^2 F - v_\perp^2 H - (2v_\|^2 + v_\perp^2)G, \qquad (4.60)$$
$$\nu_\| = v_\|^2 H + v_\perp^2 G, \qquad (4.61)$$
$$\nu_\perp = 4v_\perp^2(v_\perp^2 H + v_\|^2 G), \qquad (4.62)$$
$$\nu_{\|\perp} = 2v_\perp^2 v_\|(H - G). \qquad (4.63)$$

Xu and Rosenbluth , [Xu, 1991], found from the gyroaveraged Fokker-Planck operator an expression for the mean parallel and perpendicular components of the test particle velocity after a short time $\triangle t$

$$\overline{v}'_\| = v_\|[1 - \nu_{s\|}\triangle t], \qquad (4.64)$$
$$\overline{v}'_\perp = v_\perp^2 - v^2 \nu_{s\perp}\triangle t. \qquad (4.65)$$

This result is valid for $\nu_{s\|}\triangle t \ll 1, \nu_{s\perp}\triangle t \ll 1$ and indicates the monotonic decrease of parallel test momentum as a result of Coulomb collisions. The perpendicular and parallel velocity diffusion processes indicated by $\nu_\perp, \nu_\|,$ and $\nu_{\|\perp}$ have to be treated differently.

Because they are diffusive, they lead to a probability distribution $p(\mathbf{v} - \overline{\mathbf{v}})$ of the velocity about the mean velocity given in equations (4.64)and (4.65). Since the diffusion results from purely random processes in the parallel and perpendicular directions, we can anticipate that this probability distribution will be Gaussian and of the form

$$p(\triangle v_\parallel, \triangle p) = \frac{1}{2\pi\delta_\parallel\delta_\perp^2} \cdot e^{-\frac{\triangle v_\parallel^2}{2\delta_\parallel^2} - \frac{\triangle\Gamma^2}{2\delta_\perp^4}}, \tag{4.66}$$

where

$$\triangle\Gamma = \triangle v_\perp^2 - \beta\triangle v_\parallel. \tag{4.67}$$

By requiring

$$\langle\triangle\Gamma\triangle v_\parallel\rangle = 0, \tag{4.68}$$

the average diffusive spreads of the probability distribution are given by

$$\langle\triangle v_\parallel^2\rangle \quad = \delta_\parallel^2, \tag{4.69}$$

$$\langle(\triangle v_\perp^2)^2\rangle \quad = \delta_\perp^4 + \beta^2\delta_\parallel^2, \tag{4.70}$$

$$\langle\triangle v_\parallel^2\triangle v_\perp^2\rangle \quad = \beta\delta_\parallel^2. \tag{4.71}$$

From this gyroaveraged collision operator, they obtained

$$\delta_\parallel \quad = \quad \sqrt{\nu_\parallel(v_\parallel^2, v)v^2\triangle t}, \tag{4.72}$$

$$\beta \quad = \quad \frac{\nu_{\parallel\perp}(v_\parallel, v_\perp^2)}{\nu_\parallel(v_\parallel, v_\perp)} \cdot v, \tag{4.73}$$

$$\delta_\perp^2 \quad = \quad v^2\sqrt{\left(\nu_\perp(v_\perp^2, v) - \frac{\nu_{\parallel\perp}^2(v_\parallel, v_\perp^2)}{\nu_\parallel(v_\parallel, v_\perp)}\right)\triangle t}. \tag{4.74}$$

Equations (4.64)-(4.74) provide a basis for a probabilistic numerical approach for the inclusion of Coulomb collisional effects in a gyrokinetic system. The test-particle drag and diffusion terms can be then implemented by utilizing the following Monte Carlo method. The diffusive spreads of particle velocity are obtained by computing a random number between -1 and 1 and then multiplying this number by the average diffusive spreads [(4.72) -(4.74)]. Thus, we find the new parallel $v'_\parallel$ and perpendicular component $v'^2_\perp$ of particle velocity which can be evaluated from the old velocities $(v_\parallel, v_\perp^2, v)$ by

$$v'_\parallel \quad = \quad v_{\parallel 0} - \nu_{s\parallel}\triangle t + 2\sqrt{3}(R_1 - 0.5)\sqrt{\nu_\parallel\triangle t}, \tag{4.75}$$

$$v'^2_\perp \quad = \quad v_{\perp 0}^2 - v^2\nu_{s\perp}\triangle t + 2\sqrt{3}(R_2 - 0.5)\sqrt{\left(\nu_\perp - \frac{\nu_{\parallel\perp}^2}{\nu_\parallel}\right)\triangle t} \tag{4.76}$$

$$+ \quad 2\sqrt{3}(R_1 - 0.5)\frac{\nu_{\parallel\perp}}{\nu_\parallel}\sqrt{\nu_\parallel\triangle t}, \tag{4.77}$$

where R_1 and R_2 are two independent uniform random numbers.

4.4 Island Simulation

A change in the magnetic topology may be induced by the inclusion of a small helical magnetic perturbation. The magnetic field structure is no longer composed of nested flux surfaces. This occurs at surfaces with rational values of q. At these surfaces, the magnetic field lines break and reconnect to form magnetic islands, see Fig.(4.2). The formation of magnetic islands is generally associated with resistive instabilities and particularly tearing modes. A general
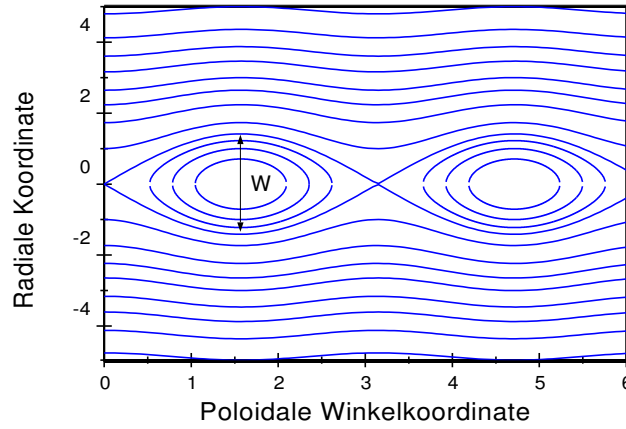
Figure 4.2: Reconnection of magnetic field producing magnetic islands

description of the perturbed fields is introduced. Only one toroidal mode is considered here, since each wave is characterized by a distinct toroidal eigenfunction, and represented as a sum of poloidal harmonics m,

$$\tilde{\Phi} = \sum_m \tilde{\phi}_m(\psi) e^{i(\mathbf{k}_{mn} \cdot \mathbf{X} - wt)} = \sum_m \tilde{\phi}_m(\psi) e^{i(n\zeta - m\theta - wt)}, \qquad (4.78)$$

where the wave vector,

$$\mathbf{k}_{mn} = n\nabla\zeta - m\nabla\theta, \qquad (4.79)$$

and in general $\tilde{\phi}_m$ may be a complex quantity containing information regarding the relative phase-shifts between neighboring harmonics.

Since $E_\parallel = 0$, a relationship between $\tilde{\Phi}$ and $\tilde{\alpha}$ is given by

$$E_\parallel = 0 \qquad \Rightarrow \qquad \nabla_\parallel \tilde{\Phi} + \frac{\partial}{\partial t}(\tilde{\alpha} B_0) = 0 \qquad (4.80)$$

$$\Rightarrow \qquad \sum_m k_{\parallel m} \tilde{\phi}_m e^{i(n\zeta - m\theta - \omega t))} = \omega B_0 \sum_m \tilde{\alpha}_m e^{i(n\zeta - m\theta - \omega t)} \qquad (4.81)$$

$$\Rightarrow \qquad \tilde{\alpha}_m = \frac{k_{\parallel m}}{\omega B_0} \tilde{\phi}_m. \qquad (4.82)$$

Although in this study only one poloidal harmonics is considered at each time, to illustrate the destruction of nested flux surfaces, a small time independent perturbation of the poloidal flux function is considered and described by the perturbation parameter $\tilde{\alpha}$. Once decomposed into Fourier harmonics and written in terms of the unperturbed toroidal flux, ψ_p becomes,

$$\psi_p = \int \frac{1}{q} d\psi - \sum_{m,n} \alpha_{mn} e^{i(n\zeta - m\theta)}. \tag{4.83}$$

where q was taken here as $q = m/n$, which in our case becomes

$$\psi_p = \int \frac{1}{q} d\psi - \alpha_{mn} e^{i(n\zeta - m\theta)}. \tag{4.84}$$

Following with this simplified model of an island and from equations (4.6), field lines are described, in general, by the equations

$$\frac{d\psi}{d\zeta} = im\alpha_{mn} e^{i(n\zeta - m\theta)}, \qquad \frac{d\theta}{d\zeta} = \frac{1}{q}, \tag{4.85}$$

being in this equation q a function of the flux, $q = q(\psi)$.

From equation (4.12),it is easy to see that the perturbation has introduced a small component of **B** across the original flux surfaces

$$\mathbf{B} \cdot \nabla \psi = im\alpha_{mn} e^{i(n\zeta - m\theta)}. \tag{4.86}$$

If α_{mn} is finite and q is not close to a rational surface $q = m/n$, then q may be approximated by a constant and the equations integrated to give

$$\theta = \frac{\zeta}{q} + \theta_0, \tag{4.87}$$

and

$$\psi = -\frac{m\alpha_{mn} q e^{i(n\zeta - m\theta)}}{m - nq} + \psi_0. \tag{4.88}$$

Therefore, the flux surfaces are distorted but remain topologically nested. If $m - nq(\psi) \approx 0$, however, the resonant denominator creates large excursions in ψ and this solution is not valid. Restricting attention to a single harmonic described by the mode numbers m and n, the resonant surface will lie on $q = m/n$, given by its toroidal eigenfunction

$$\tilde{\Phi} = \tilde{\phi}_m(\Psi) e^{i(n\zeta - m\theta)} \tag{4.89}$$

Field lines on this surface define a helix and $\chi = \theta - n\zeta/m$ is a convenient angular coordinate orthogonal to this helix (parallel to **k** on this surface). Expanding q around ψ_0 such that

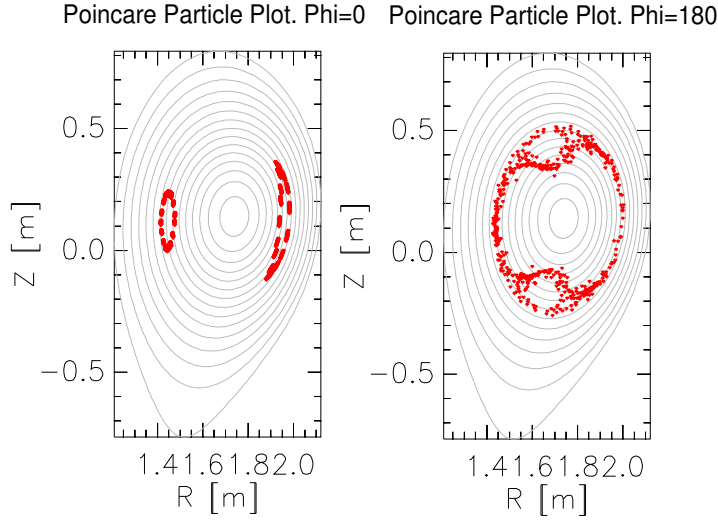Poincare Particle Plot. Phi=0   Poincare Particle Plot. Phi=180

Figure 4.3: View of a Magnetic Island at two different toroidal angles $\phi_1 = 0$ and $\phi_2 = \pi$. Poincaré plot mapped out by a particle with an energy of 5 eV and a pitch angle of $\Upsilon_{HAGIS} = v_\parallel / v_{total} = 0.9$.

$$q(\psi) = \frac{m}{n} + \frac{dq}{d\psi}(\psi - \psi_0) \tag{4.90}$$

gives, using equation (4.85)

$$\frac{d\chi}{d\zeta} = -\left(\frac{n^2 q'}{m^2}\right)(\psi - \psi_0), \qquad and \qquad \frac{d\psi}{d\zeta} = im\alpha e^{-im\chi}, \tag{4.91}$$

where $q' = dq/d\psi$. These equations may be integrated to give

$$(\psi - \psi_0)^2 = \frac{2m^2}{n^2 q'}\alpha \left[e^{-im\chi} + c\right], \tag{4.92}$$

where c is a constant determined by the initial position. In order to examine island structures, the so-called Poincaré plot is often made, which is constituted by the points formed of successive transits of a field line in the θ, ψ plane at $\zeta = 0$, see Fig. (4.3). Poincaré is usually mapped out by particles with large $v_\parallel / v_\perp$ and a small energy. It is seen from the definition of χ that at $\zeta = 0$, $\chi = \theta$. Expanding near $\theta = l\pi/m, l \in \mathcal{Z}$, it is found that

$$(\psi - \psi_0)^2 + \frac{\alpha m^2}{n^2 q'}(m\theta)^2 = constant, \tag{4.93}$$

i.e. for $\alpha/q' > 0$ and $c < 1$ the points lie on elliptic manifolds about the periodic points, while for $c > 1$ the points lie on hyperbolic manifolds. Thus, there is a chain of elliptic and hyperbolic points at $\psi = \psi_0$. This island chain is separated from the topological toroidal surfaces by a

separatrix. The separatrix is described by choosing the integration constant $c = 1$, giving islands with width

$$\triangle\psi = \frac{4m}{n}\sqrt{\frac{\alpha}{q'}} \tag{4.94}$$

In order to validate the numerical approach, the obtained island width using HAGIS code was compared by [Pinches, 1996]with the analytical estimate found, using equation (4.94) with an accuracy of

$$\frac{\triangle\psi_{HAGIS}}{\triangle\psi_{Analytical}} = 0.909 \tag{4.95}$$

4.5 Numerical Simulations

4.5.1 Confinement Time

In order to validate the code, several comparisons were made between analytical values and numerical values generated by HAGIS-code.

The confinement time was calculated theoretically, using the following expressions for the banana regime.

$$\tau = \frac{a^2}{5.8 \cdot D_{GS}} \tag{4.96}$$

where a is the minor radius, D_{GS} is the diffusion coefficient in the banana regime, and the 5.8 is a factor coming from the cylindrical geometry. As seen in previous section, equation (2.65)

$$D_{GS} = \frac{q^2}{\varepsilon^{3/2}}\nu_i\rho_l^2 \tag{4.97}$$

where q is the safety factor, ε is the inverse aspect ratio, ν_i is the ion collision frequency and $\rho_l$the Larmor radius. Taking for the ion collision frequency, the simplified form corresponding to singly charged ions, [Wesson, 1997], becomes

$$\nu_i^{-1} = \tau_i = 6.60 \cdot 10^{17}\left(\frac{m_i}{m_p}\right)^{1/2}\frac{T_i^{3/2}}{nln\Lambda}, \tag{4.98}$$

where T_i is the fast ion energy, n is the electron density and $ln\Lambda$ is the Coulomb logarithm and was taken $ln\Lambda = 17$. This gives for deuterium with an energy of $T = 100$keVand a test-density of $n = 8.4 \cdot 10^{21}m^{-3}$, a value of $\nu_i = 1.67 \cdot 10^2 s^{-1}$. Such a density is not real under ASDEX Upgrade conditions, but the validity of this approach was proved, since the confinement time scale with the density as $1/n$. Such a density was taken in order to speed up the calculations. Calculating for the specific values of an ASDEX Upgrade discharge

$$R = 1.6m, \quad \varepsilon = 0.26, \quad q = 4 \quad and \quad \rho_i = 21.5mm \tag{4.99}$$

we obtain analytically a confinement time of

$$\tau = 0.0093s \tag{4.100}$$

while with the right density, $n = 8.4 \cdot 10^{19} m^{-3}$ we obtain analytically a confinement time of $\tau = 0.93s$.

Simulating the behavior of 400 co-injected fast ions in ASDEX Upgrade with the improved version of HAGIS, but only with collisions and not with MHD modes, the expected exponential function for the fast ion losses was obtained, see Fig.(4.4).
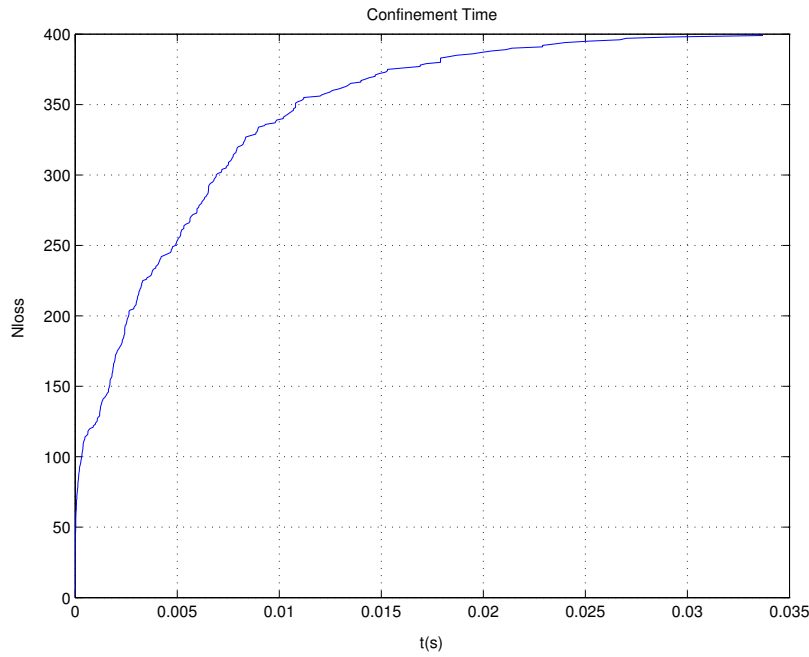
Figure 4.4: Exponential growth of ion losses due to collisions. Computation made with a density of $n = 8.4 \cdot 10^{21} m^{-3}$. The peak at short times due to prompt losses is also shown.

Modelling the rate of fast ion losses as in the following equation

$$N_{loss}(t) = N_{prompt} + (N_{tot} - N_{prompt})(1 - e^{-t/\tau}) \tag{4.101}$$

taking logarithms and rewriting it, the confinement time τ, is easily calculated by means of the following equation

$$ln(N_{tot} - Nloss) = -\frac{1}{\tau}t + ln(N_{tot} - N_{prompt}) \tag{4.102}$$

and the linear regression of the numerical data, see Fig. (4.5).

$$\tau_{HAGIS} = 0.0059s \tag{4.103}$$

The approach is then proved to be correct, since

$$\frac{\tau_{HAGIS}}{\tau} \sim 0.6 \tag{4.104}$$

However, the accuracy is not the best one, since the coefficient $\frac{\tau_{HAGIS}}{\tau}$ was not equal to 1. That is because the particles were not ionized directly in the center of the plasma, also they were not thermal and the equation used for calculating the confinement time is valid for thermal particles. Although, the deviation from the expected value, due to these inaccuracies, was not too important, as shows the final result.

The scaling of the confinement time with the density was proved computing the behavior of 500 co-injected particles with the real density, giving a confinement time of $\tau_{HAGIS} = 0.45s$. The small divergence of this two values obtained by means of the simulations is due to the approach in the linear regression and the limit of the prompt losses, since the calculations must be done without the prompt losses, in other case the exponential behavior of the losses is not satisfied.
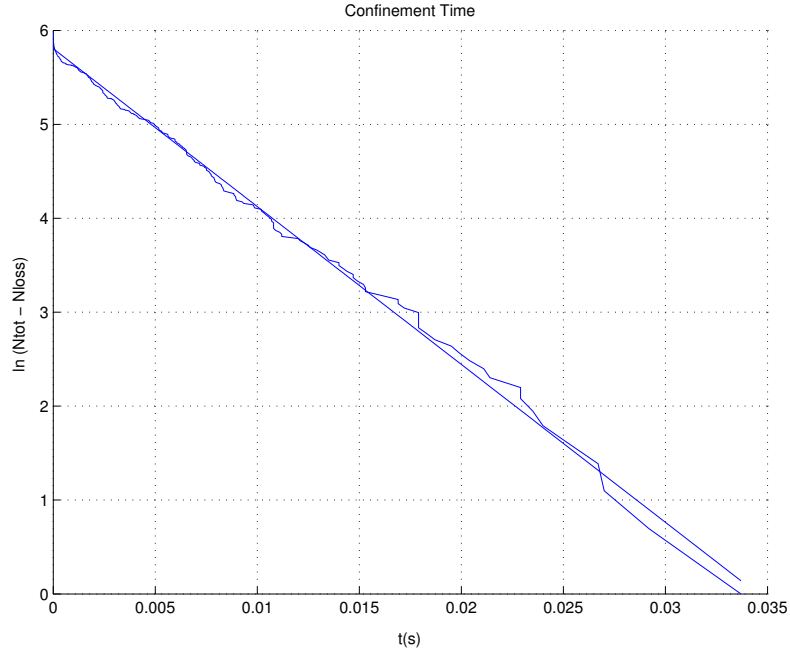
Figure 4.5: Numerical results and its linear regression. The prompt losses were not considered in order to have a suitable exponential behavior.

4.5.2 Slowing down Time

Once the neutral beam particles entering the plasma have become ionized, the resulting fast ions are slowed down by Coulomb collisions. By means of these collisions, the fast NBI-ions transfer their energy to the background particles, electrons and ions.

Since electrons and ions have a different mass, the study of collisions with background particles must be made separately. Collisions with electrons cause only a small scattering of the beam ions. Consequently if the drag force which the electrons transmit to the beam ion is F_{be}, and beam ion velocity is v_b, the heating of the plasma electrons is given by

$$P_e = -F_{be}v_b. \tag{4.105}$$

Giving the force F_{be} as the rate of momentum loss [Wesson, 1997], the electron heating is then given by

$$P_e = \frac{em_e^{1/2}m_b A_D \varepsilon_b}{3(2\pi)^{1/2}T_e^{3/2}}. \tag{4.106}$$

where

$$A_D = \frac{ne^4 ln\Lambda}{2\pi\varepsilon_0^2 m_b^2}. \tag{4.107}$$

and ε_b is the beam energy $\frac{1}{2}mv_b^2$.

The study of collisions with ions is similar, but the difference in mass causes another effect on the beam ions. Due to their similar mass, the slowing down process of the beam ion is accompanied by a scattering of the beam ion velocities principally perpendicular to the initial direction of the beam. This scattering constitutes a 'heating' of the beam ions, energy which will heat the plasma but not in the initial direct heating. Therefore, the initial direct heating of the plasma ions is

$$P_i = -F_{bi}v_b - \frac{1}{2}m_b\langle v_\perp^2 \rangle \tag{4.108}$$

where $\langle v_\perp^2 \rangle$ can be seen as the diffusion term, and F_{bi} is the drag force on the beam ion due to the plasma ions.

Therefore, the direct heating of the plasma ions appears as

$$P_i = \frac{m_b^{5/2}A_D}{2^{3/2}m_i\varepsilon_b^{1/2}} \tag{4.109}$$

And the total direct heating per beam ion, $P = P_e + P_i$, given by the combination of equations (4.105) and (4.109) is

$$P = \frac{2m^{1/2}m_b A_D}{3(2\pi)^{1/2}T_e^{3/2}} \varepsilon_b \left(1 + \left(\frac{\varepsilon_c}{\varepsilon_b}\right)^{3/2}\right) \tag{4.110}$$

where ε_c is the critical energy, given by

$$\varepsilon_c = \left(\frac{3\sqrt{\pi}}{4}\right)^{2/3} \left(\frac{m_i}{m_e}\right)^{1/3} \frac{m_b}{m_i} T_e. \tag{4.111}$$

In order to study the slowing down of the beam ions, just consider the power balance equation

$$P = -\frac{d\varepsilon_b}{dt} \tag{4.112}$$

and with equation (4.110), it follows

$$\frac{d\varepsilon_b}{dt} = -\frac{2}{\tau_{se}} \varepsilon_b \left(1 + \left(\frac{\varepsilon_c}{\varepsilon_b}\right)^{3/2}\right) \tag{4.113}$$

where

$$\tau_{se} = \frac{3(2\pi)^{1/2}T_e^{3/2}}{m_e^{1/2}m_b A_D} \tag{4.114}$$

Therefore, integrating the equation (4.113), being ε_{b0}, the initial value of ε_b, the solution for the beam energy at each time is:

$$\varepsilon_b = \varepsilon_{b0} \left[e^{-3t/\tau_{se}} - \left(\frac{\varepsilon_c}{\varepsilon_{b0}}\right)^{3/2} \left(1 - e^{-3t/\tau_{se}}\right)\right]^{2/3} \tag{4.115}$$

The slowing down characteristic time may be calculated, just putting $\varepsilon_b = 0$, that follows

$$\tau = \frac{\tau_{se}}{3} ln \left(1 + \left(\frac{\varepsilon_{b0}}{\varepsilon_c}\right)^{3/2}\right). \tag{4.116}$$

The validation of the code results is here proved just by comparing the theoretical curve for the equation of the beam energy and the results obtained using HAGIS. The theoretical curve was represented using the same parameter as in HAGIS, that means,

$$T_e = 4\text{keV}, \quad n = 8.4 \cdot 10^{19} m^{-3}, \quad \varepsilon_{b0} = 93\text{keV} \quad and \quad \tau_{se} = 0.3129s. \tag{4.117}$$

Giving a slowing down time of $\tau \simeq 0.071s$ which is in agreement with the numerical results, as shown in graphic (4.6) and (4.7), where both curves are represented.
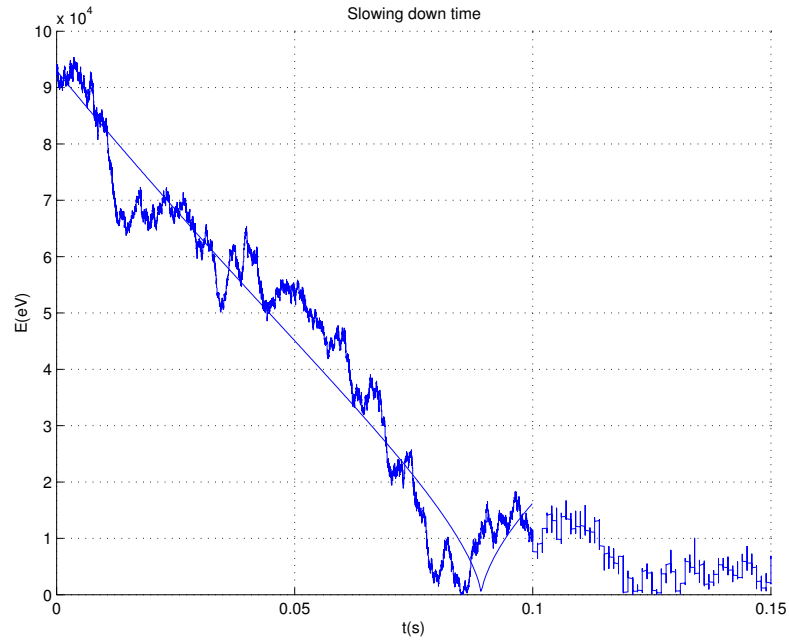
Figure 4.6: Numerical slowing down and its analytical behavior of a test particle with an initial energy of 93 keV.
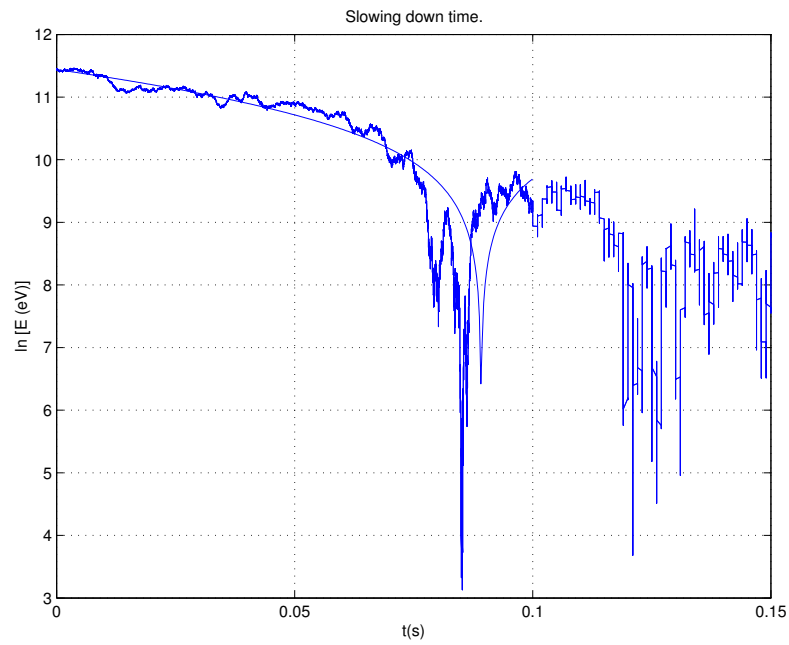
Figure 4.7: Numerical slowing down and its analytical behavior in logarithmic scala.

Chapter 5

GOURDON-Code

5.1 Introduction

GOURDON is a full 3-D computer program that computes 3-D particle trajectories using a 3-D magnetic field configuration. The code was developed in 1970 by C.Gourdon to compute magnetic fields and field lines in toroidal devices.

It is the aim of this work to deeply study the fast ion losses in tokamaks and since HAGIS traces particle trajectories only inside the last closed magnetic surface, this 3-D version of GOURDON was improved to compute particle trajectories outside the separatrix in ASDEX Upgrade. The real orbits of all particles which cross the plasma boundary are traced without collisions by means of the GOURDON code. A real magnetic configuration was computed from a specific discharge in ASDEX Upgrade. Together with the present vessel geometry of this discharge, the deposition pattern of the high energetic particles on the vessel walls was calculated. The computation of the magnetic field is stored on a grid in toroidal coordinates, a transformation of coordinates to cartesians is then made and finally the interpolation for further calculations, [Kisslinger]. Since this version of GOURDON was thought to work with stellarator devices, the existence of plasma currents had to be introduced. A final improvement of the code was the implementation of the geometry of a further detector, where the manipulator is in ASDEX Upgrade, in order to name the particles which strike the detector.

5.2 Structure of the Code

First of all, the magnetic field of a real discharge is computed from an ASDEX Upgrade equilibrium reconstruction (LIBKK-routines). Once the magnetic field and its derivatives are computed in cylindrical coordinates , they are stored in a 2-D grid. This grid supplies the input data for further calculations with GOURDON. Since GOURDON computes the guiding center trajectory as well as the real orbit in cartesian coordinates, the appropriate transformation of coordinates is made here. The next step is the calculation of the geometry of the limiting structures in ASDEX Upgrade corresponding to the discharge. The corresponding geometry

is supplied by the LIBKK-routines. The obtained data are stored in cylindrical coordinates in a file.

During the calculation of the trajectories, as well as the pursuit of field lines, it was asked at each integration step if the corresponding trajectory crossed any target plate. In that case, the coordinate of the cross point in cylindrical coordinates and the number of the target plate is written in a file.

5.3 Description of Physics in Code

5.3.1 Magnetic Field Configuration

Computing the magnetic field from the discharge using statistical methods, needs much more computational time than interpolating it from magnetic field values given on a grid. Therefore, the magnetic field is computed once on a grid and then stored. This grid has to cover the relevant region, i.e. the plasma region and the boundary region including the first wall. Furthermore, it has to be good enough to guarantee results, independently of its discreteness. The grid points are equidistant in cylindrical coordinates (R, ϕ, z). They are defined on a region satisfying the first requirement (for ASDEX Upgrade geometry $R_{min} = 1.0m$, $z_{min} = -1.80m$ and $R_{max} = 2.50m$ and $z_{max} = 1.80m$).

The magnetic field as well as its derivatives, are computed from a real discharge using different statistical methods by means of the LIBKK-routines. Then, the field is stored and serves as an input to GOURDON. Since this version of GOURDON makes the calculations in cartesian coordinates and the magnetic field was stored in cylindrical coordinates, the appropriate transformation was made, taking into account that in tokamaks the ansatz $\nabla \times \mathbf{B} = 0$ is not valid anymore. Details can be found in appendix A.

5.3.2 Particle Trajectories

Originally, the code was programmed to compute magnetic field lines in toroidal devices as well as to show the magnetic surfaces and to study the magnetohydrodynamic stability by means of the the integral $V' = \frac{1}{M} \int \frac{dl}{B}$. The field line is followed from a starting point by means of the ADAMS method of integration. The present version of GOURDON follows field lines as well as computes guiding center trajectories and real orbits of particles. The input data for the computation of guiding center trajectory are the same as for the computation of real orbits, requiring also the last one, the gyro phase. The definition of pitch angle in code has to be taken into account, since it is different as in the other two codes used during this work,

$$\Upsilon_{GOURDON} = \frac{v_\perp}{v_{total}}. \tag{5.1}$$

Therefore, the input data for the computations are: the coordinates of the guiding center, the velocity of the particle (energy) and its pitch angle with its sign in order to differentiate co-going particles from counter-going particles.

Guiding Center Trajectories

The motion of the guiding center is calculated here under the adiabatic approach. As seen in chapter 2, the motion of the guiding center can be written in terms of the velocity components, parallel and perpendicular to the magnetic field line. Therefore, the equations of motion programmed in GOURDON are the following:

$$\frac{dv_\parallel}{dt} = -\frac{\mu}{m} \cdot \frac{\mathbf{B} \cdot \nabla B}{B} \tag{5.2}$$

$$\frac{d\mathbf{x}}{dt} = \frac{m}{eB^2} \cdot v_\parallel^2 (\mathbf{B} \times \mathbf{k}) + \frac{\mu}{eB^2}(\mathbf{B} \times \nabla B) + \mathbf{v}_\parallel. \tag{5.3}$$

where

$$\mathbf{B} \times \mathbf{k} = \frac{1}{B}(\mathbf{B} \times \nabla B) + \nabla \times \mathbf{B} - \frac{1}{B^2}\mathbf{B}(\mathbf{B} \cdot \nabla \times \mathbf{B}). \tag{5.4}$$

The radius of curvature of the field line is given by

$$\rho = \frac{1}{|\mathbf{k}|} \tag{5.5}$$

and the magnetic moment by

$$\mu = \frac{m \cdot v_\perp^2}{2B} = const. \tag{5.6}$$

Since the program does not check if the adiabatic approach is correct or not, when the particle has a large gyro radius, this approach must be checked. The validity of the approach can be proved by comparing the obtained guiding center trajectory with the real orbit of the particles computed using the code.

The computation of the motion of the guiding center goes on, whilst the guiding center stays in the given space, which is the plasma vessel.

Real Orbits

In this section, the real orbit of charged particles in magnetic fields is computed. The trajectory is computed step by step by integrating the equation of motion

$$\frac{d\mathbf{v}}{dt} = \frac{e}{m}(\mathbf{v} \times \mathbf{B}) \tag{5.7}$$

The integration step is given by the user. The value of the integration step depends on the curvature radius of the particle trajectory, so that the step integration should be around 0.03 times the curvature radius.

The rise of errors because of an inappropriate integration step is checked at each step by means of the total velocity. Since the total velocity must be constant, only magnetic field is considered
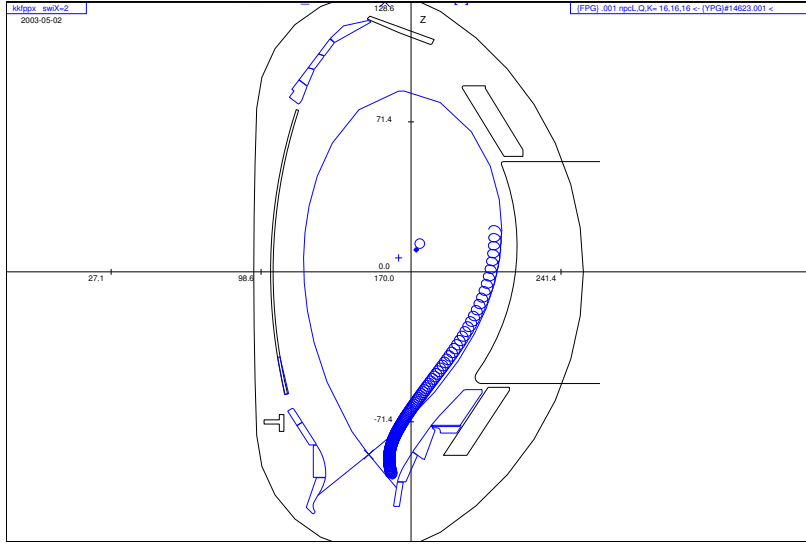
Figure 5.1: Projection in poloidal plane of the trajectory of a deuterium with 93 keV and $\Upsilon_{GOURDON} = 0.81$. The initial magnetic field is B=1.75T and the guiding center initial position: R=2.10m and z=0.20m.

and it does not lead to any change in the total velocity, $\frac{v}{v_0}$ is calculated at each step, the program stops if this coefficient does not lie inside the interval (0.99, 1.01).

The input data for this calculation are the same as in the section for guiding center trajectory but here the initial gyro phase must be given as well. The initial gyro phase is given by the angle which form the projection of **v** on the R-z plane with **R** at the initial point of the trajectory.

The calculation of the trajectory goes on while the particle is inside the given space, geometry of the vessel. Then, the program stops and gives the final coordinates of the particle.

5.4 Results

Different particles of interest in fusion reactions as well as particles of the NBI were followed using the code here presented in order to validate the calculations. The real magnetic field configuration corresponds to the discharge number 15839@4.45s of ASDEX Upgrade. The difference between these trajectories is due to the different particle energy and mass. A typical deuterium generated by the neutral beam injection system with an energy of 93 keV was followed with different pitch angles and initial positions. The Fig. (5.1) shows the projection in the poloidal plane of the trajectory of a deuterium which was ionized closed to the separatrix, with a pitch angle $\Upsilon_{GOURDON} = 0.85$. Since there are no collisions and no magnetic perturbations the particle follows the magnetic field line, ending its trajectory as the separatrix does, on the wall.

In Fig.(5.2), a deuterium also with an energy of 93 keV but with a pitch angle of 0.51 was followed. The relationship between the components of the velocity does not satisfy the equation

62
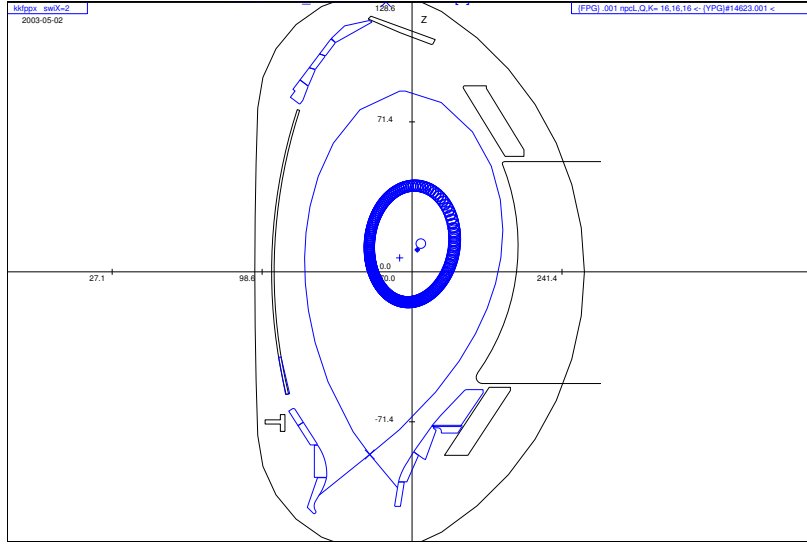
Figure 5.2: Projection in the poloidal plane of the trajectory of a deuterium with 93keV and Pitch=0.51. The initial magnetic field is B=1.88T and the guiding center initial position: R=1.90m and z=0.20m.

(2.45) for the condition of trapping orbits, so the particle does a passing trajectory.

In order to test the code with different particles of fusion reactions, the following reaction was considered,

$$D + D = p(3.024MeV) + T(1.008MeV). \tag{5.8}$$
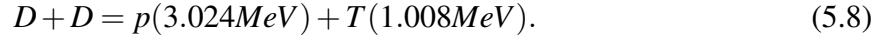
and trajectories of tritium (1.008 MeV) and protons(3.024 Mev) were computed.

In Fig.(5.3) is shown the projection in the poloidal plane of the trajectory of a fusion born tritium with 1.008 MeV, it can be seen that the tritium makes a confined orbit but with large excursions in the radial direction.

The trajectories of a fusion born proton with 3.024MeV at two different pitch angles are shown in Fig.(5.4). The one with a pitch angle of 0.81 trace a large unconfined banana orbit, since its velocity components satisfy the trapping condition seen in chapter 2.

According to equation (2.23), the 3.024MeV protons vertical drift velocity is the largest because its energy is the largest. They have a gyroradius around 11 cm in the region of high magnetic field. They always leave the plasma before the calculation time expires, though they start at the same point and with the same pitch angle than the tritium. Since the dependence of the magnetic field on the radius, R, can be approached by $\frac{1}{R}$, the gyro radius of each particle always is much larger in the outer side of the plasma, as can be seen in Fig.(5.3) and Fig.(5.4).
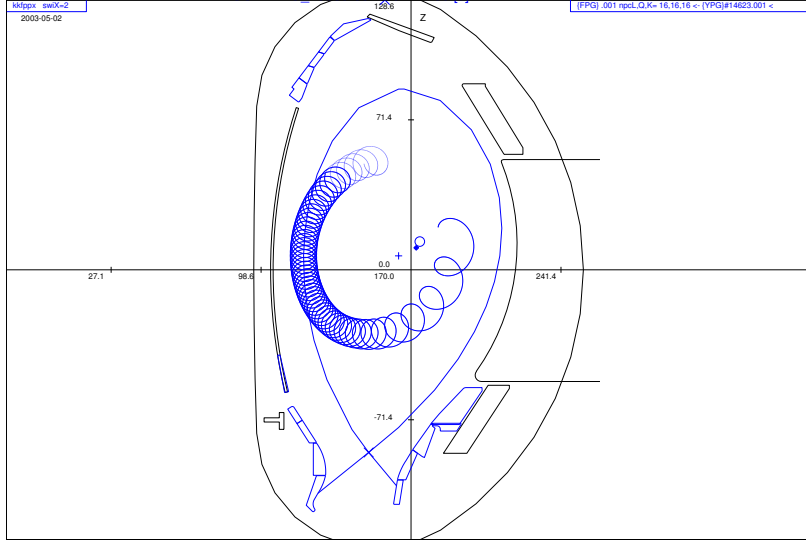
Figure 5.3: Projection in the poloidal plane of the trajectory of a tritium with 1.008MeV and $\Upsilon_{GOURDON} = 0.51$, 'confined passing orbit'. The initial magnetic field is B=1.88T and the guiding center initial position: R=1.90m and z=0.20m.
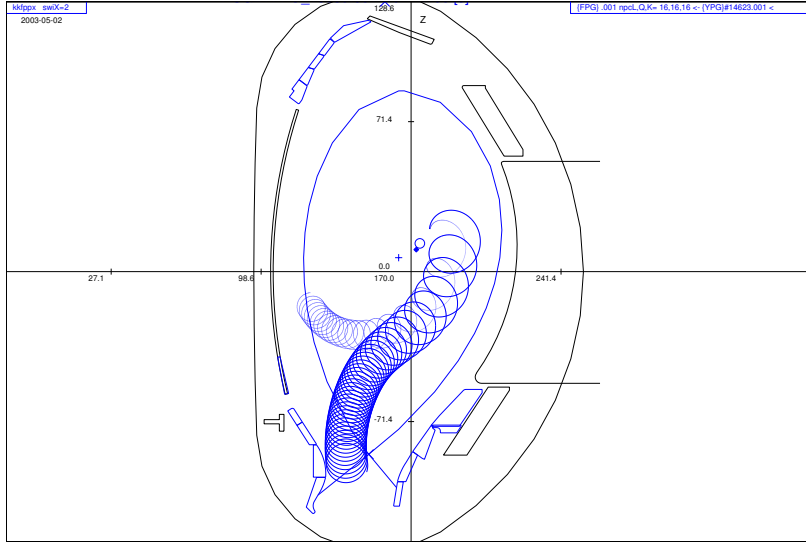
Figure 5.4: Projection in the poloidal plane of the trajectory of two protons with 3.024MeV and $\Upsilon_{GOURDON} = 0.81$, 'large unconfined banana', and $\Upsilon_{GOURDON} = 0.51$, 'passing-orbit with large excursion' .The initial magnetic field is B=1.88T, and the guiding center initial position: R=1.90m and z=0.20m.

Chapter 6

Results

Four different cases were examined in order to make a deep study of the behavior of fast ions with their environment. Counter-injected particles, as well as co-injected particles were followed with the code-package, being the last one the most interesting, since in ASDEX Upgrade they are the most common. However, several calculations were also made for counter-injected ions, proving that losses from counter-injection always appear to be stronger than from co-injection. The results shown here were calculated using 1000 co-injected particles with an energy of 93keV. No important differences can be observed on the poloidal direction of all of the ion loss distribution.

6.1 No Collisions

In absence of collisions and MHD-modes, ion losses appear just before the first $10^{-5}s$, since there are no more mechanisms to cause any other losses. They are the so-called prompt losses which were defined in section 1.3. Taking into account that the initial distribution function of fast ions was almost localized at two ϕ toroidal angles, prompt losses are also localized in the toroidal coordinate, as shown in Fig.(6.2). Particles which lie on such an orbit but come from the second branch of the initial distribution supplied by FAFNER, see Fig. (3.4) explain the few prompt losses at different ϕ angles. They were ionized in the inner side of the plasma so that they have to do longer excursions in order to leave the plasma. For that reason, these losses are not so localized around a given ϕ angle.

Prompt losses appear at a time shorter than $10^{-5}s$, that implies that they do not have enough time to collide with background particles. Therefore, the orbits of such particles are either directly lost orbits or trapped and lost orbits. Two examples of such orbits are presented in Fig.(6.1). Both of them correspond to deuterium from the NBI system which are ionized with velocities lying within the loss cone, see equation (2.45), and then followed with their specific parameter, using the GOURDON code. Since there are no collisions, no change in the energy of the particles is expected. Therefore, there is also no change in the prompt losses velocity, and their perpendicular and parallel components lie on a circumference of radius $v_{total} = const$, see Fig.(6.3). As expected, the velocities of the prompt losses lie on the same interval than the
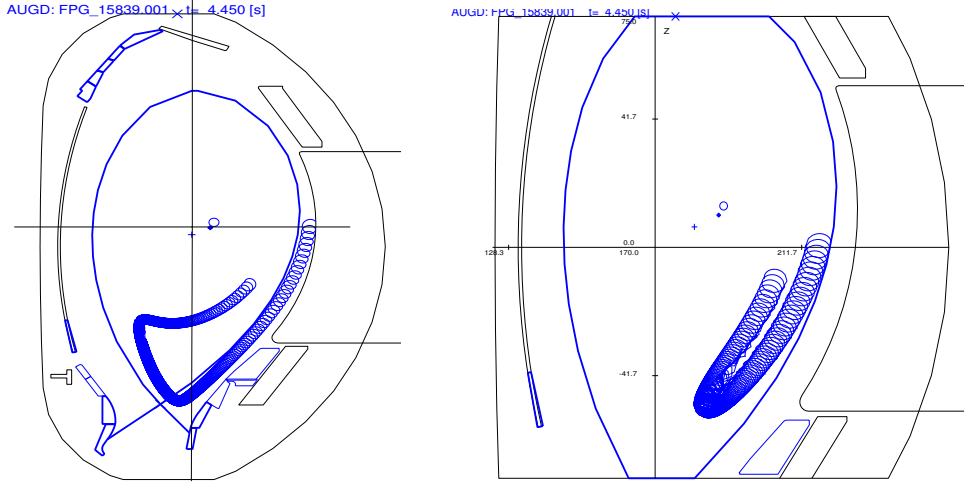
Figure 6.1: Projection in poloidal plane of the trajectory of two prompt lost deuterium with 93keV and $\Upsilon_{GOURDON} = 0.85$, but started at different guiding center positions giving rise to a 'large unconfined banana' and an 'unconfined banana'. The initial magnetic field is $B \sim 1.75T$.

velocities in the initial distribution, supplied by FAFNER.

6.2 With Collisions

Since the slowing down process is of crucial importance in the study of ion orbits, it also has to be considered for the study of ion losses. The influence of collisions in the distribution of ion losses is shown here, following the description made in section 2.3. Because the slowing down time is much shorter than the confinement time $\tau_{Slowdown} < \tau_{Conf}$, as seen in the previous section, the particles slow down to the thermal energy, giving rise to the symmetrization in the toroidal direction. As Fig.(6.4) shows, the particle distribution is no longer localized along the ϕ angle. Fast ions cross the separatrix at every toroidal location due to the symmetrization in the toroidal direction.

Since fast ions slow down by means of collisions, their velocity is not a constant anymore. Perpendicular and parallel components of the lost ions do not lie on the circumference of radius $v_{total} = const$, as happened in the previous case with the prompt losses, see Fig.(6.5).

Since the losses occur at different times, in this picture three regions can be differentiated, : the first one where the lost particles have not changed their initial velocity thus, their velocities lie on the circumference of radius $v_{total} = const$, the second one where the particles slow down, in this region the lost particles have a velocity within the loss cone, and the third region where the velocity of the lost particles lies inside the circumference of radius $v = 1.2 \cdot 10^6 m/s$. The first region is constituted by the prompt losses and the particles which were ionized closed to the separatrix in a passing orbit and leave the plasma after the first collisions.

It can be deduced from this picture that the particles which leave the plasma in the second region, due to collisions, have a relationship between perpendicular and parallel component of
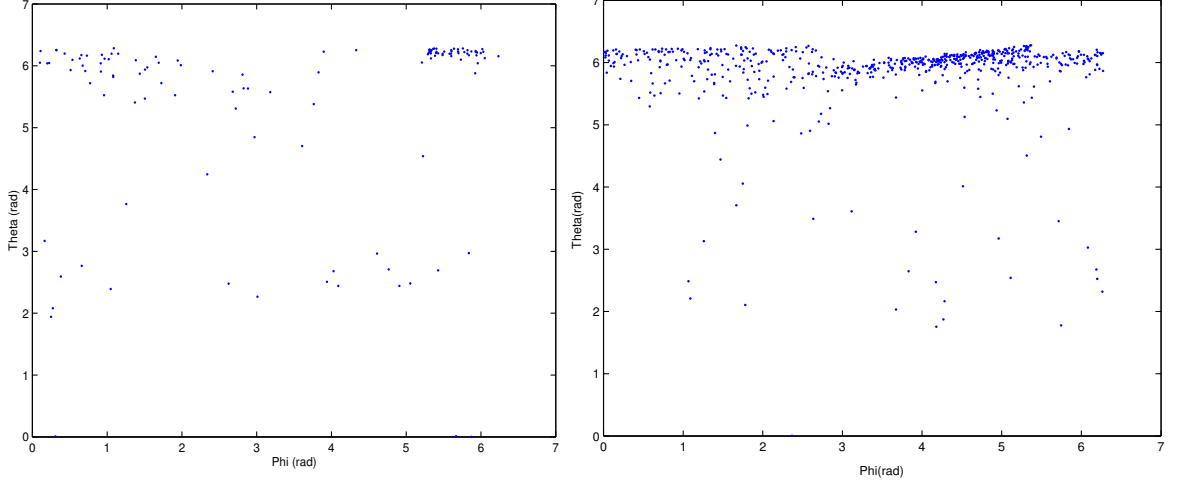
66

Figure 6.2: Prompt losses distributions in the plane given by the flux coordinates θ and φ. Distributions obtained using co- and counter-going injected particles.

the velocity. They lie in the region of the loss cone, see section 2.2.2, defining the loss cone to be the region where

$$\frac{v_{\parallel}}{v_{\perp}} < \left(\frac{2r}{R_0 - r}\right)^{1/2} = \left(\frac{2\varepsilon}{1 - \varepsilon}\right)^{1/2} \simeq 1 \quad for \quad \varepsilon = 0.25. \tag{6.1}$$

As shown in this picture, most particles which leave the plasma between the two external circumferences, are inside the loss cone. Therefore, these losses are a result of their banana orbits. Banana orbits also seem to be the reason for the losses between the region which is dominated by the prompt losses and the region which is dominated by the losses of thermal particles. Only the right side of the loss cone is filled, that is just because the initial velocity of the particles were in this side.

Inside the circumference of radius $v = 1.2 \cdot 10^6 m/s$, the fast injected particles which leave the plasma have velocities within the whole circumference, their velocities do not just lie in the loss cone anymore. That is because the Maxwell distribution of the background particles is symmetric around the zero. The losses should be grouped around the circumference, defined by the radius of the background energy, $v = 0.62 \cdot 10^6 m/s$, now we also find passing losses from the edge of the plasma.

In concordance with the expected results, a peak in the ion losses appears at short time, due to the prompt losses, which are particles that leave the separatrix before the exponential decay is achieved, see Fig.(6.6).
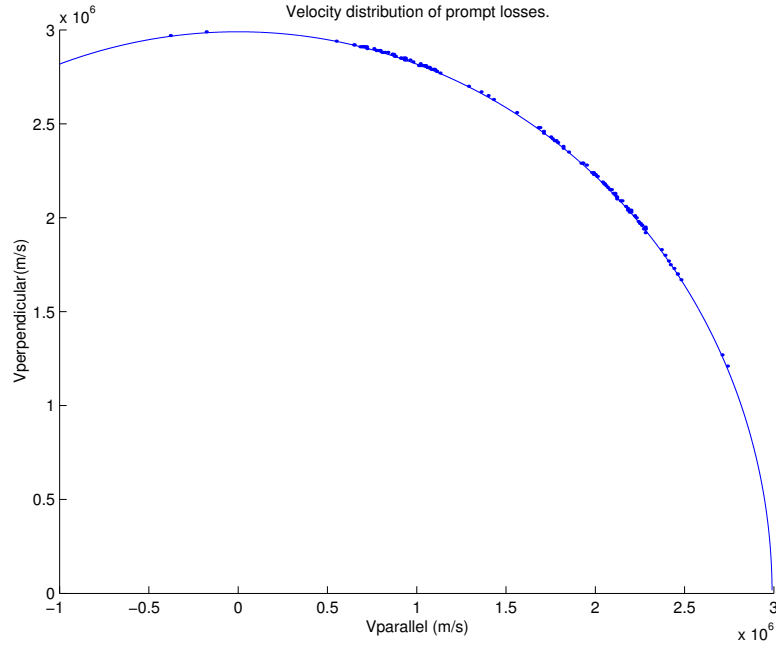
Figure 6.3: Velocity distribution of the lost particles in absence of collisions and MHD-modes. Prompt losses.

6.3 MHD-modes

A single toroidal mode, n = 1, was considered with certain radial profile and frequency. Different cases, namely m=4 and m=2 were studied separately. In a simplified study, to see much more better the influence of the mode, non-rotational modes with different amplitudes were taken into account. The effect of the MHD-perturbation on the motion of each particle is presented in Fig.(6.7), where the projection in the poloidal plane of an unperturbed banana orbit is plotted together with the corresponding perturbed trajectory in order to see the influence of a mode with a high amplitude, $\sim 6 \cdot 10^{-2}$, on such an orbit. As shown in that picture, the perturbation can induce a transition from passing to trapped orbit, causing more losses, as occurred with collisions, see Fig. (2.4). As shows Fig.(6.8), the good localization of ion losses seen in Fig.(6.2) is broken in the presence of MHD modes, as well as in the presence of collisions. This distribution was obtained studying the effect of MHD-induced losses on the delocalization, using a mode with n=1, m=2, and a high amplitude. The mode then produces a more delocalized ion loss distribution, accompanied by a higher number of ion losses).

However, in this case, the distribution seems to be partially localized around a certain toroidal position, $\phi = \pi$ which coincides with the X-point of the island, formed by the mode m=2. The topology of the island is shown in Fig.(4.3) at two different toroidal positions in a poincaré plot in order to identify the X-point of the island at $\phi = \pi$.

In order to understand much better the effect of a MHD-mode on the spatial distribution of losses, a mode m=4 with a high amplitude was studied. As Fig.(6.9) shows, the losses are distributed along the magnetic field lines on the flux surface, q=4. Therefore, the distribution
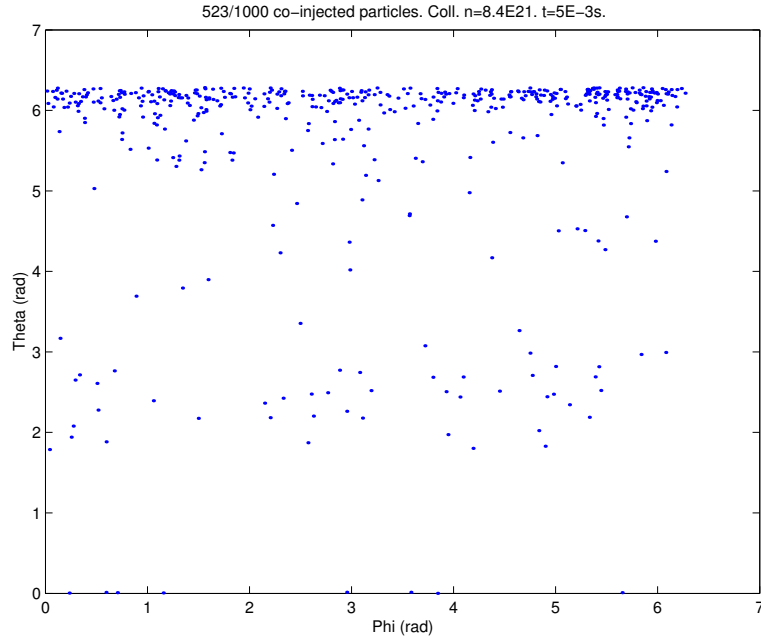
Figure 6.4: Symmetrization due to collisions. Study of the effect of the collisions on the spatial distribution of the losses. Energy of the background T=4 keV and electron density of $n = 8.4 \cdot 10^2 1 m^{-3}$

of losses is not localized in the toroidal or poloidal angle anymore. On the left side of this picture, the field lines on the q=4 surface were plotted, since the distribution of the losses was plotted on the right side.

The radial profiles considered for each mode, together with the safety factor, are shown in Fig.(6.10) in order to see which perturbation amplitude (radial profile) corresponds to each magnetic surface, q=2 or q=4.

No effect on the change of the total velocity of the lost particles was observed with the two modes and this fast ion configuration, since the interaction between both of them appears only under certain resonance conditions, as seen in chapter 1. Because of that, as Fig.(6.11) shows, the velocity distribution lies on the circumference of radius $v_{total} = const$. The difference which was found between the two velocity distributions is that the mode m=4 also induces losses in the region of $v_\parallel < 0$. Such result will be of great value in further works to determinate the mechanism for these mode-induced losses. As seen in chapter 1, three possible mechanisms of losses induced by MHD-perturbations are considered, being the stochasticity not possible in this work, since only one harmonic was considered.

6.4 MHD-modes and Collisions

The influence of MHD-modes, together with collisions on the ion loss distribution, is shown in this section. As shown in Fig.(6.12), the distribution of lost ions due to collisions and the
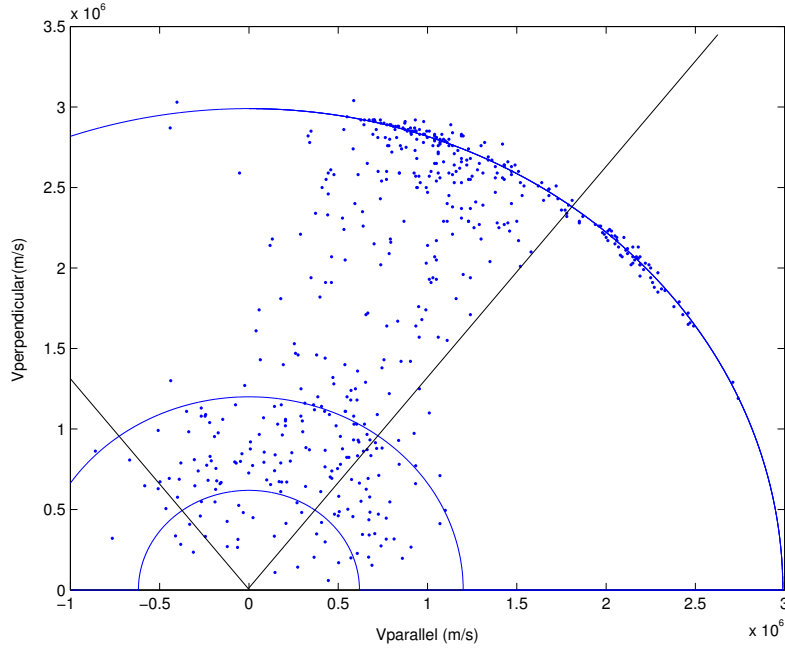
Figure 6.5: Velocity distribution due to collisions. Collisions distinguish three regions in the distribution. The loss cone.

mode m=2, is totally delocalized in the toroidal direction, but not in the poloidal direction, as it was also the case only with collisions. However, the spatial distribution of losses considering collisions and the mode m=4 is found delocalized in the toroidal direction, as well as in the poloidal direction. The losses appear along the field lines as Fig.(6.13) shows. Comparing Fig.(6.9) with Fig.(6.13), it can be seen that the effect of the collisions produces a better distribution of the losses in the poloidal direction, since the particles do not leave the plasma only along the field lines.

The effect of the MHD-mode on the ion losses is more important in the presence of collisions, 720 losses of 1000 injected particles with the mode m=4,which is more than in the case with only MHD-modes, 525 losses of 1000 injected particles with the same mode. That is because the particles make excursion in the radial direction by means of collisions reaching the region where the island is, and suffering in that way the effect of the perturbation.

Since the particles slow down, they leave the plasma with different velocities and due to that, the velocity distribution does not lie on the circumference of $v_{total} = const$ anymore. No noticeable difference can be seen due to the MHD-mode because the mode does not change the total velocity of the particles. The velocity distribution stays similar to the case in which there were only collisions, as shows Fig.(6.14). However, it can be seen that there are some losses on the left side of the loss cone that appears as an effect of the mode m=4. As seen in the previous section, this perturbation induces some losses in the region where $v_{\parallel} < 0$, but due to the collisions not only on the circumference of $v_{total} = const$.
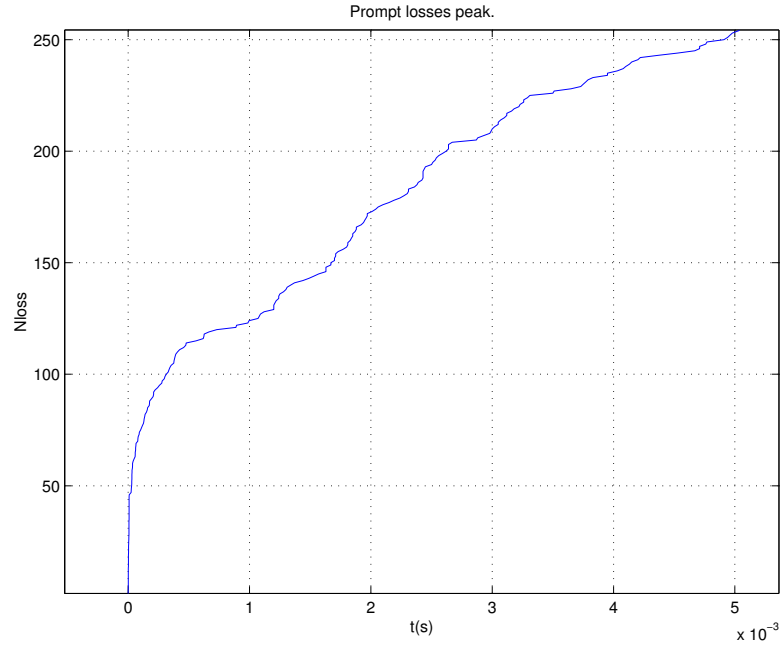
70

Figure 6.6: Peak at a very short time due to prompt losses.

6.5 Conclusions for the Detector Design

The development and construction of a charged particle detector will allow to measure the fast ion losses in the ASDEX Upgrade tokamak. The final aim of this work is to have the necessary tools to analyze and compare the theoretic data with the obtained measurement, using the fast ion detector. A deep study of the ion loss distributions was made during this work, in order to know the most suitable place for the detector. As a first attempt to make a model of the fast ion detector, the work of [Darrow, 2001] was very helpful . Since a typical ASDEX Upgrade discharge only has co- or counter-going beam ions, the probe will be able to measure only one of them at each discharge. Because of that, the detector needs to have only one pinhole so that the particles enter through.

The escaping energetic ions will be detected using a magnetic spectrometer, as shows Fig. (6.15). The design which will be used is based on the concept of the α-particles detector, that is used with highly accurate results in the Tokamak Fusion Test Reactor (TFTR), [Darrow, 1995], as well as in the stellarator W7-AS, [Darrow, 2001], see Fig(6.15).

The probe will be located outside the plasma and will be formed by a metal box with a pair of apertures mounted in one side. Escaping ions that are able to pass through both apertures strike the end of the box at a position determined by their pitch angle and gyroradius. The end of the box contains a plate, coated with a scintillator that emits light when bombarded with the ions. A three dimensional model of the probe can be seen in Fig.(6.16).

The code-package here developed will supply the necessary information about the pitch angle and energy (gyro-radius) of the particles which will strike the scintillator plate.
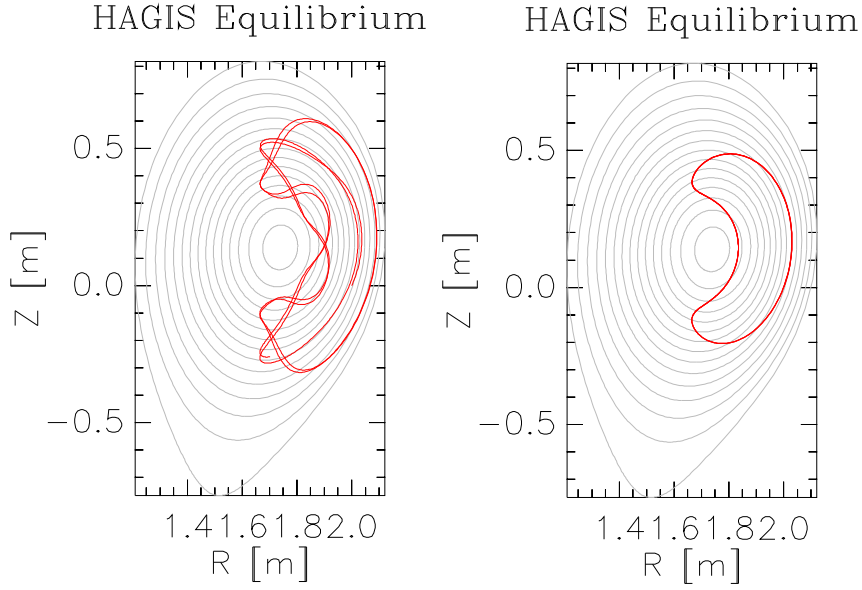
Figure 6.7: Influence of the MHD-perturbation (n=1, m=4) on the trajectory of the particles. Parameters considered: amplitude=$6 \cdot 10^{-2}$, frequency = $10^{-6} s^{-1}$ and a radial profile given by $P(s) = s^2$, where s plays the role of a radial coordinate.

Particles leaving the separatrix at a certain (ϕ, θ) position are followed using GOURDON-code till they reach the vessel wall. In the opposite direction, particles can also be followed just changing the sign of the velocity. These tools will be of great value to identify the reason of the loss of these particles. Assumed that a particle strikes the detector with a certain pitch angle and energy. Just following this particle with the same parameter but with opposite velocity, it is localized by crossing the separatrix at a certain (ϕ, θ) position. By comparing these coordinates with the ion loss distributions from the previous section, the most possible reason for such a loss can be studied.

In order to show the power of the code-package, a particle was released with certain parameters (energy and pitch angle) at the manipulator position and followed till it crossed the separatrix, see Fig.(6.17). The initial conditions of the test particle are:

$$v_{total} = 3 \cdot 10^6 m/s, \qquad \Upsilon_{GOURDON} = 0.95 \qquad (6.2)$$

The inserts in Fig.(6.17) show where the particle, followed from the detector, left the plasma in the velocity space as well as in the real space.

The installation of the detector on the midplane manipulator (mobile tube) gives the chance to modify the original position, in order to solve possible inaccuracy in our calculations. However, from this work it follows that the most suitable place for the detector is also the midplane, and wherever in the toroidal direction, since the obtained ion loss distributions were toroidally symmetric. Cases in which the distribution was neither poloidal nor toroidally symmetric anymore were also found in the presence of certain MHD-modes. This topic should also be considered in further works as well as for the installation of the detector.
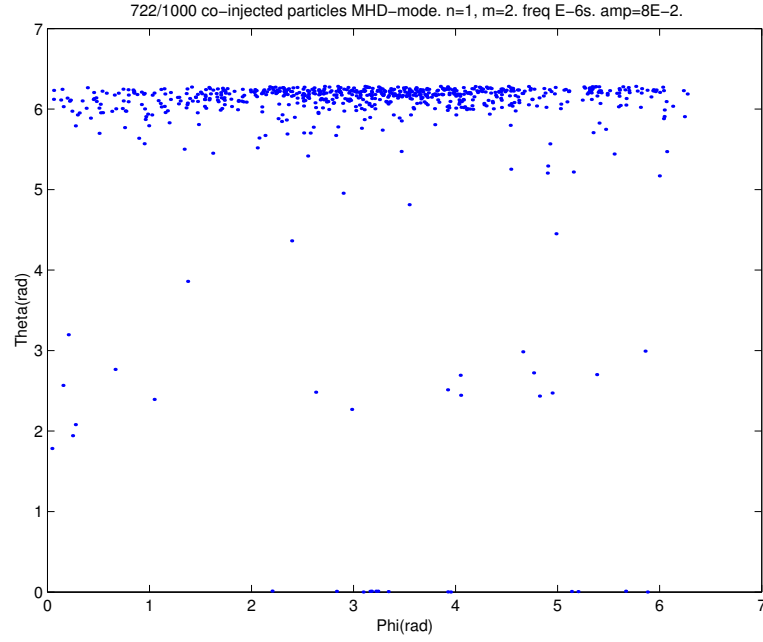
Figure 6.8: Symmetrization due to the MHD-mode, n=1 and m=2. Parameters considered: amplitude=$8 \cdot 10^{-2}$, frequency = $10^{-6}s^{-1}$ and a radial profile given by $P(s) = s^2 - 2s^3 + s^4$, where s plays the role of a radial coordinate.
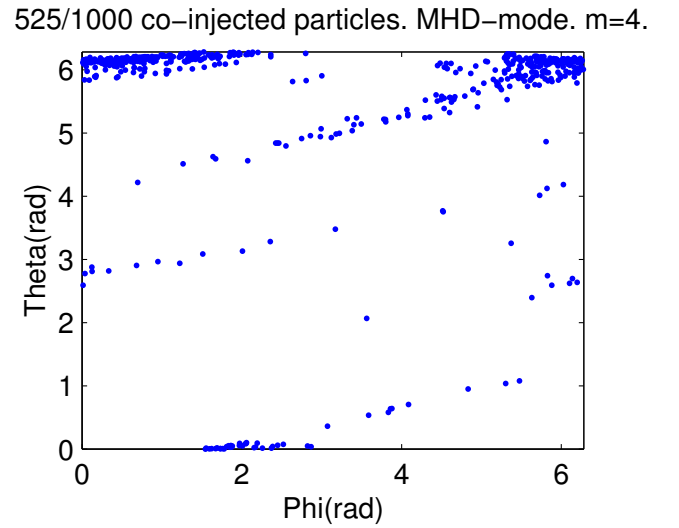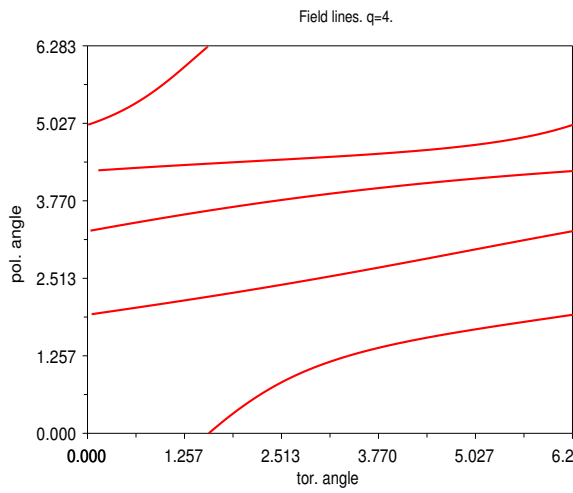

Figure 6.9: Distribution of losses along the field lines due to the mode n=1 and m=4. The perturbation was studied with an amplitude of $6 \cdot 10^{-2}$ and a frequency of $10^{-6}s$. The field lines on the flux surface q=4 is also presented.
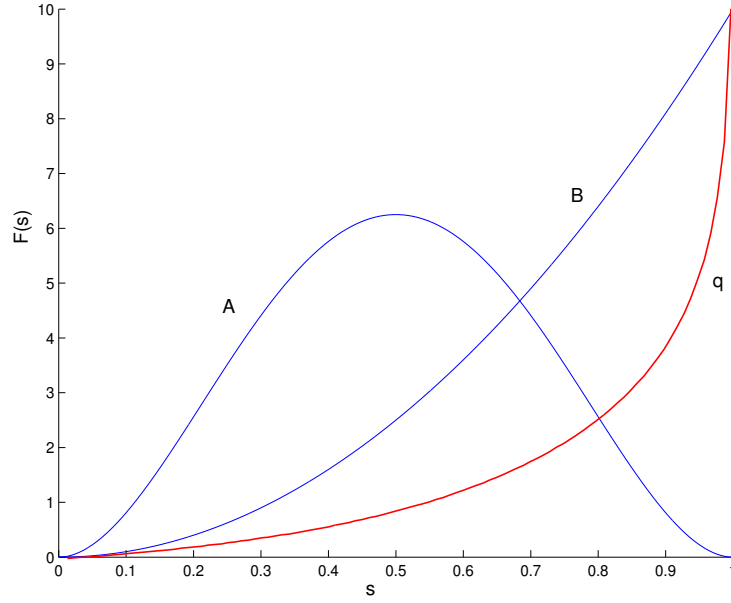
Figure 6.10: Radial profile of the two perturbations considered with the safety factor (red one). The two profiles were given by the polynomials: $P_A(s) = s^2 - 2s^3 + s^4$ and $P_B(s) = r^2$ where s plays the role of a radial coordinate.
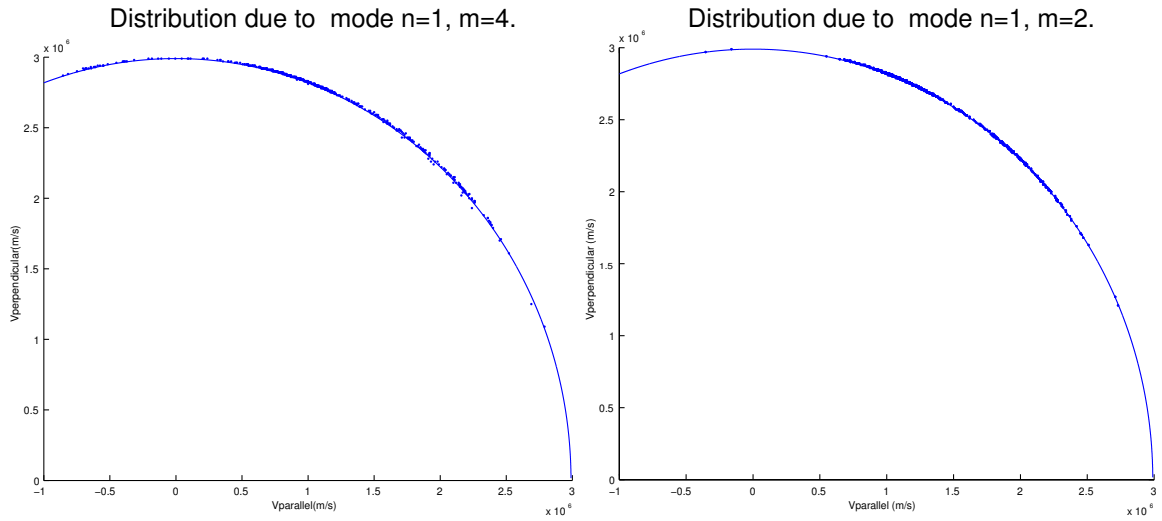
Figure 6.11: Velocity distributions due to the two MHD-modes, n=1, m=4 and m=2. The parameters considered for both cases were: amplitude=$6 \cdot 10^{-2}$, frequency = $10^{-6} s^{-1}$ and a radial profile given by $P_A(s)$ and $P_B(s)$, where s plays the role of a radial coordinate.
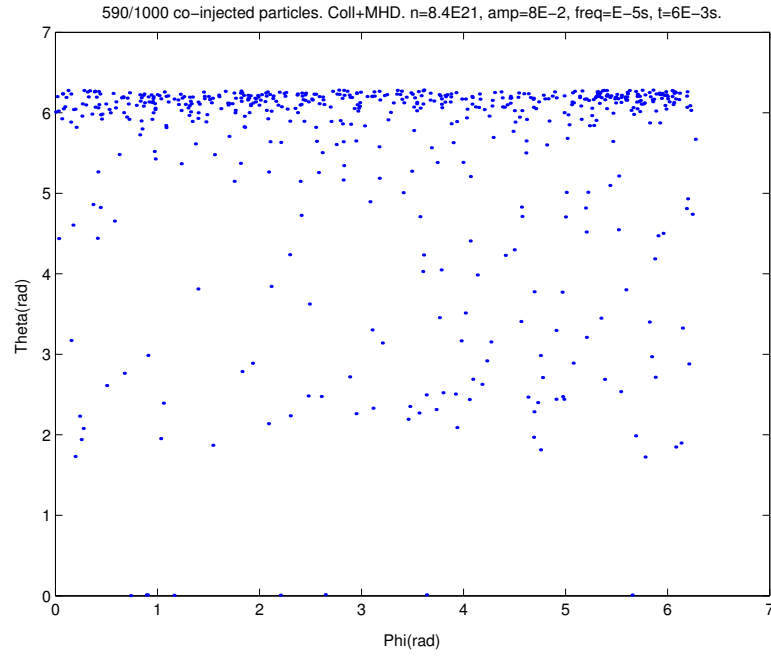
Figure 6.12: Symmetrization due to MHD-modes and collisions. Distribution calculated for an electron density of $n = 8.4 \cdot 10^{21} m^{-3}$. The mode considered was the n=1 and m=2 with and amplitude of $6 \cdot 10^{-2}$ and a frequency of $10^{-6} s^{-1}$.
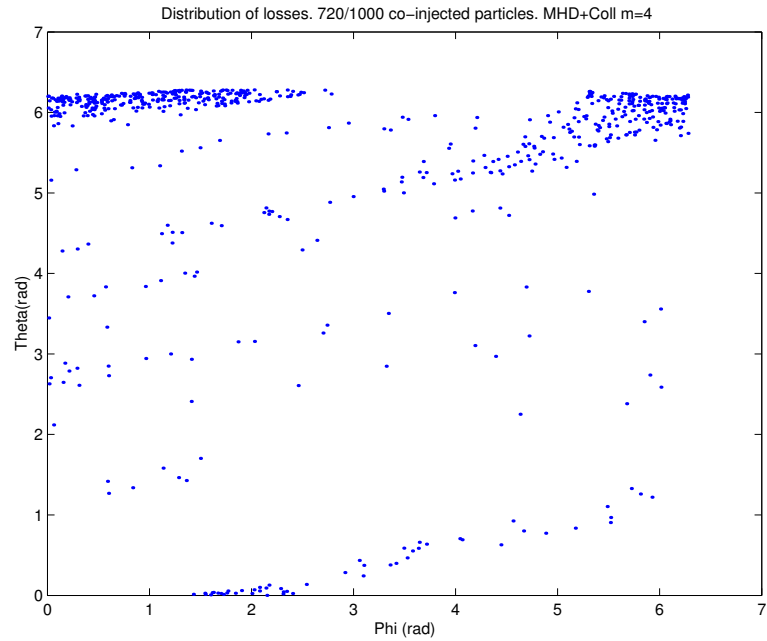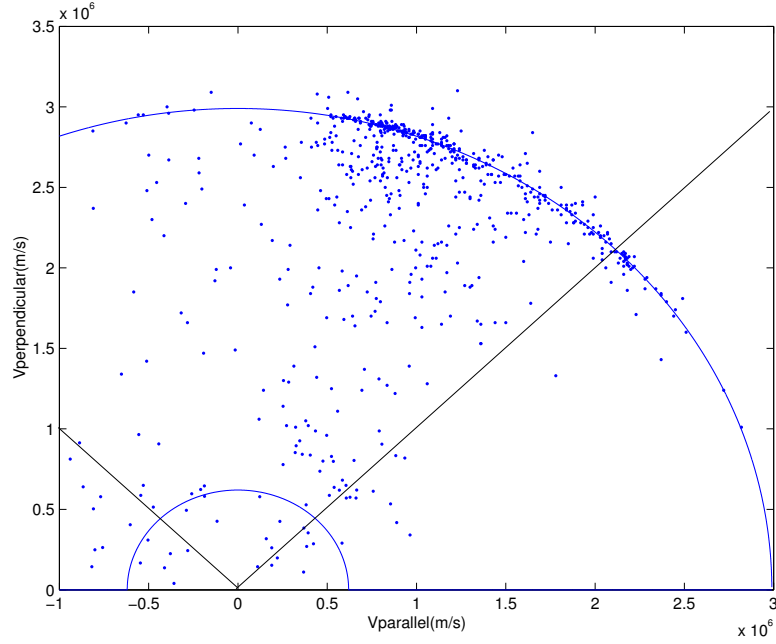

Figure 6.13: Distribution due to MHD-modes and collisions. Distribution calculated for an electron density of $n = 8.4 \cdot 10^{21} m^{-3}$. The mode considered was the n=1 and m=4 with an amplitude of 10^{-2} and a frequency of $10^{-6} s^{-1}$. The particles leave the plasma following the field lines.

Figure 6.14: Velocity distribution due to MHD-modes and collisions. Distribution calculated for an electron density of $n = 8.4 \cdot 10^{21} m^{-3}$. The mode considered was the n=1 and m=4 with an amplitude of 10^{-2} and a frequency of $10^{-6} s^{-1}$.
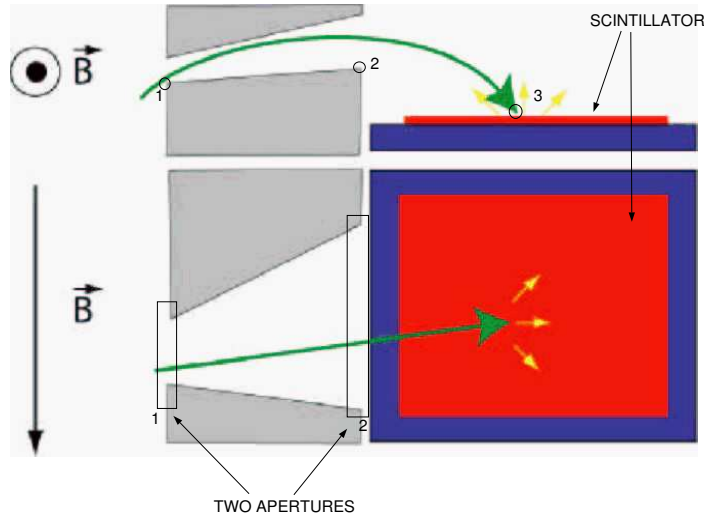

Figure 6.15: Schematic top and side view of the probe with a possible fast ion orbit. The gyroradius (energy) of the particle determines how far from the apertures it will strike the scintillator. The pitch angle determines where the ion will strike along the orthogonal dimension of the scintillator. Points 1,2, and 3 determine the gyroradius, while points 1 and 3 determine the pitch angle.

Figure 6.16: Overview of a 3-D model of the operation. Some different particle trajectories are plotted entering into the detector and thus, striking the scintillator plate.

Figure 6.17: Particle encountering detector. Projection in poloidal plane of the trajectory of a deuterium which leaves the plasma with certain parameters given in the velocity and spatial distributions and strikes the detector.

Chapter 7

Summary

The tokamak operation is often restricted by the losses of fast ions, especially before they slow down and lose their energy to the bulk of the plasma. This may lead to different effects on operation regimes. To avoid these, it is of special importance to understand the reason for these losses. This can be gained from a combination of a theoretical model of the behavior of fast ions in tokamaks with the measurements of such losses. A full understanding is possible only with both methods. The code-package developed here provides the theoretical view of the losses, in order to understand the measurement obtained, using the appropriate detector. The main advantage of these tools is the possibility to follow single particles in two directions; either from where they are born inside the plasma until they strike either the wall or the detector, or from the strike point at the wall or detector until where they were born, like back in the time. That gives hints toward the reason for such a loss, i.e. due to insufficient confinement properties of the magnetic field or due to magnetohydrodynamic perturbations occurred during the discharge, making possible the identification of the perturbation. Following particles from where they are born inside the plasma, the code-package simulates the ionization pattern of the NBI system in ASDEX Upgrade and then computes the trajectory of the fast ions inside the separatrix, taking into account the specific magnetic configuration of each discharge and calculating the effect of a perturbation on particle trajectories. Once the particles have left the plasma, the particles are followed by means of a real orbit code without collisions. By that the exact cross point where the particles leave the torus is given. First of all, the collision operator was validated, calculating the slowing down time of the fast ions inside the plasma as well as proving the dependence of the confinement time on the density. To demonstrate the power of the developed tools, it has been applied to different types of magnetohydrodynamic perturbations as well as to different collision parameters in ASDEX Upgrade. The mechanisms of losses were studied in different ways, prompt losses, effects of collisions, effects of MHD-modes and finally the effect of both together, collisions and MHD-modes were also considered. The distribution of prompt losses was found to be highly localized for the case with co-going ions around the NBI injector position in the toroidal direction. However, some losses were found at different ϕ angles because the injected beam was tangential. The prompt losses for counter-going ions was found to be not so localized anymore, since the ions can trace large banana orbit before they leave the plasma. In absence of magnetohydrodynamic perturbations,

it was found that the losses appear in three different regions, depending on their velocities. This result confirms the hypothesis that most particles which leave the plasma while they slow down, make it in a banana orbit. Two different modes were considered, m=2 and m=4, both with n=1, providing that the effect of each mode is located on different radial positions and that such perturbations have no important effect on the velocity distribution of the losses. However, different spatial distributions of the losses were found with each mode. The mode m=2 leads to losses localized around a poloidal angle but along the whole torus, finding more losses at $\phi = \pi$, where the island had its X-point, while with the mode m=4 was found that the particles which leave the plasma, make it along the field lines on the magnetic surface q=4.

Together, the effect of collisions and MHD-modes were considered, leading to a no localized distribution of losses in the toroidal direction but localized around the midplane.

Strictly speaking, these results were obtained only for a small class of fast ions with a particular energy in the interior of a specific ASDEX Upgrade discharge. However, these results can be generalized for different particles, since all important parameters in the description of their orbits are taken into account and can be modified.

Finally, the code-package here presented was applied to a first model of a detector to be installed in ASDEX Upgrade. It was shown that the code-package will be of great value for detector design as well as interpretation of the measurements.

Appendix A

Transformation of Coordinates

In this appendix, the appropriate transformation between cartesian and toroidal coordinates, used in GOURDON, is calculated. The relationship between the components of the magnetic field as well as their derivatives in both system of coordinates is here developed. First of all, the components of the magnetic field can be written in terms of the toroidal coordinates as follows

$$
\begin{align}
B_x &= -B_\phi \cdot \sin\phi + B_r \cdot \cos\phi \tag{A.1} \\
B_y &= B_\phi \cdot \cos\phi + B_r \cdot \sin\phi \tag{A.2} \\
B_z &= B_z. \tag{A.3}
\end{align}
$$

From that, each derivative was calculated as a function of the toroidal coordinates and their derivatives respect to the toroidal coordinates. So that, the derivative of B_x with respect to x can be written in toroidal coordinates as follows

$$
\begin{align}
\frac{dB_x}{dx} &= \frac{d}{dx}(-B_\phi \cdot \sin\phi + B_r \cdot \cos\phi) = \\
&- \frac{d\phi}{dx} \cdot \sin\phi - \frac{d}{dx}(\sin\phi) \cdot B_\phi + \frac{dB_r}{dx} \cdot \cos\phi + B_r \cdot \frac{d}{dx}(\cos\phi) = \\
&- \sin\phi \cdot \cos\phi \cdot \frac{dB_\phi}{dr} + B_\phi \frac{\sin\phi \cdot \cos\phi}{r} + \sin\phi \cdot \cos\phi \frac{dB_r}{dr} + \frac{\sin^2\phi}{r} \cdot B_r \tag{A.4}
\end{align}
$$

where the following chain rules were considered and will be used in the rest of the calculations.

$$
\begin{align}
\frac{d\phi}{dx} &= -\frac{\sin\phi}{r} \tag{A.5} \\
\frac{dr}{dx} &= \cos\phi \tag{A.6} \\
\frac{d(\cos\phi)}{dx} &= \frac{\sin^2\phi}{r}, \tag{A.7} \\
\frac{d(\sin\phi)}{dx} &= -\frac{\sin\phi \cdot \cos\phi}{r} \tag{A.8}
\end{align}
$$

80

$$\frac{dB_\phi}{dx} = \frac{dB_\phi}{d\phi} \cdot \frac{d\phi}{dx} + \frac{dB_\phi}{dr} \cdot \frac{dr}{dx} = \frac{dB_\phi}{dr} \cdot \cos\phi \qquad (A.9)$$

$$\frac{dB_r}{dx} = \frac{dB_r}{d\phi} \cdot \frac{d\phi}{dx} + \frac{dB_r}{dr} \cdot \frac{dr}{dx} = \frac{dB_r}{dr} \cdot \sin\phi. \qquad (A.10)$$

Since the system was taken as toroidally symmetric, the magnetic field does not vary with the toroidal angle ϕ. The derivative of B_y with respect to x is given by

$$\begin{aligned}
\frac{dB_y}{dx} &= \frac{d}{dx}(B_\phi \cdot \cos\phi + B_r \cdot \sin\phi) = \\
&\quad \frac{dB_\phi}{dx} \cdot \cos\phi + B_\phi \cdot \frac{d}{dx}(\cos\phi) + \frac{dB_r}{dx} \cdot \sin\phi + B_r \cdot \frac{d}{dx}(\sin\phi) = \\
&\quad \frac{dB_\phi}{dr} \cdot \cos^2\phi + B_\phi \cdot \frac{\sin^2\phi}{r} + \sin\phi \cdot \cos\phi \cdot \frac{dB_r}{dr} - B_r \cdot \frac{\sin\phi \cdot \cos\phi}{r}. \qquad (A.11)
\end{aligned}$$

The derivative of B_z with respect to x coordinate seems to be trivial.

$$\frac{dB_z}{dx} = \frac{dB_z}{dr} \cdot \cos\phi. \qquad (A.12)$$

Now, the derivatives with respect to y are calculated.

$$\begin{aligned}
\frac{dB_x}{dy} &= \frac{d}{dy}(-B_\phi \cdot \sin\phi + B_r \cdot \cos\phi) = \\
&\quad B_r \cdot \frac{d}{dy}(\cos\phi) + \frac{dB_r}{dy} \cdot \cos\phi - B_\phi \cdot \frac{d}{dy}(\sin\phi) - \frac{dB_\phi}{dy} \cdot \sin\phi = \\
&\quad - \frac{\sin\phi \cdot \cos\phi}{r} \cdot B_r + \cos\phi \cdot \sin\phi \cdot \frac{dB_r}{dr} - \frac{\cos^2\phi}{r} \cdot B_\phi - \sin^2 \cdot \frac{dB_\phi}{dr}. \qquad (A.13)
\end{aligned}$$

Where the following chain rules were taken into account.

$$\frac{d\phi}{dy} = \frac{\cos\phi}{r} \qquad (A.14)$$

$$\frac{dr}{dy} = \sin\phi \qquad (A.15)$$

$$\frac{d(\cos\phi)}{dy} = -\frac{\sin\phi \cdot \cos\phi}{r} \qquad (A.16)$$

$$\frac{d(\sin\phi)}{dy} = \frac{\cos^2\phi}{r} \qquad (A.17)$$

$$\frac{dB_r}{dy} = \frac{dB_r}{d\phi} \cdot \frac{d\phi}{dy} + \frac{dB_r}{dr} \cdot \frac{dr}{dy} = \frac{dB_r}{dr} \cdot \sin\phi \qquad (A.18)$$

$$\frac{dB_\phi}{dy} = \frac{dB_\phi}{d\phi} \cdot \frac{d\phi}{dy} + \frac{dB_\phi}{dr} \cdot \frac{dr}{dy} = \frac{dB_\phi}{dr} \cdot \sin\phi. \qquad (A.19)$$

The derivative of B_y with respect to y can be written as

$$
\begin{aligned}
\frac{dB_y}{dy} &= \frac{d}{dy}(B_\phi \cdot \cos\phi + B_r \cdot \sin\phi) \\
&\quad B_\phi \cdot \frac{d}{dy}(\cos\phi) + \cos\phi \cdot \frac{dB_\phi}{dy} + B_r \cdot \frac{d}{dy}(\sin\phi) + \sin\phi \cdot \frac{dB_r}{dy} = \\
&\quad - \frac{\sin\phi \cdot \cos\phi}{r} \cdot B_\phi + \sin\phi \cdot \cos\phi \cdot \frac{dB_\phi}{dr} + \frac{\cos^2\phi}{r} \cdot B_r + \sin^2\phi \cdot \frac{dB_r}{dr}. \quad \text{(A.20)}
\end{aligned}
$$

And finally the derivative of B_z with respect to y is given by

$$
\frac{dB_z}{dy} = \frac{dB_z}{dr} \cdot \sin\phi. \tag{A.21}
$$

The derivatives with respect to z are trivial, as the following equations show.

$$
\frac{dB_x}{dz} = -\frac{dB_\phi}{dz} \cdot \sin\phi + \frac{dB_r}{dz} \cdot \cos\phi \tag{A.22}
$$

$$
\frac{dB_y}{dz} = \frac{dB_\phi}{dz} \cdot \cos\phi + \frac{dB_r}{dz} \cdot \sin\phi \tag{A.23}
$$

$$
\frac{dB_z}{dz} = 1. \tag{A.24}
$$

Appendix B

The ASDEX Upgrade experiment

The ASDEX Upgrade divertor tokamak went into operation at Garching in 1990 and it successes ASDEX, which was in operation from 1980 until 1990. At present, it is Germany's largest fusion device. Its name is derived from Axial Symetric Divertor EXperiment. To make experiments under reactor-like conditions possible essential plasma properties, particularly the plasma density and pressure and the wall load, have been adapted in ASDEX Upgrade to the conditions that will be present in a future fusion reactor. Like ASDEX, ASDEX Upgrade has a poloidal divertor, which was optimized to meet the requirements of a future fusion reactor. In order to get an overview of the experiment, the global parameters are listed here.

Major plasma radius	R_0	1.65 m
Minor plasma radius	a	0.5 m
Plasma height	b	0.8 m
Plasma elongation	s=b/a	1.6
Plasma aspect ratio	A	3.3
Maximum magnetic field	B_{max}	3.1 T
Plasma volume	V_{plasma}	$13m^3$
Plasma current	I_{plasma}	2 MA
Discharge duration	t_D	10 s
Plasma density	n_e	$\leq 3 \cdot 10^{20} m^{-3}$
Average plasma temperature	$T_i = T_e$	5 keV
Heating power	P[MW]	$20_{(NBI)}, 5.7_{(ICRH)}, 1.6_{(ECRH)}$

Table B.1: ASDEX Upgrade parameters.

The plasma is controlled through a system of 12 vertical field coils and kept in its elliptical shape with an X-point above the bottom divertor. The purely toroidal field is usually kept constant during the entire discharge. Nevertheless it can also be varied during the discharge to some degree, if the physical requirements need such a field variation. Additionally there are two vertical field coils close to the plasma for a fast control of the plasma.

The described set of coils is controlled in real-time by a control computer. This computer calculates through a large number of measurement coils the actual values from the plasma position and plasma shape and corrects the currents in the field coils in order to achieve the desired values.
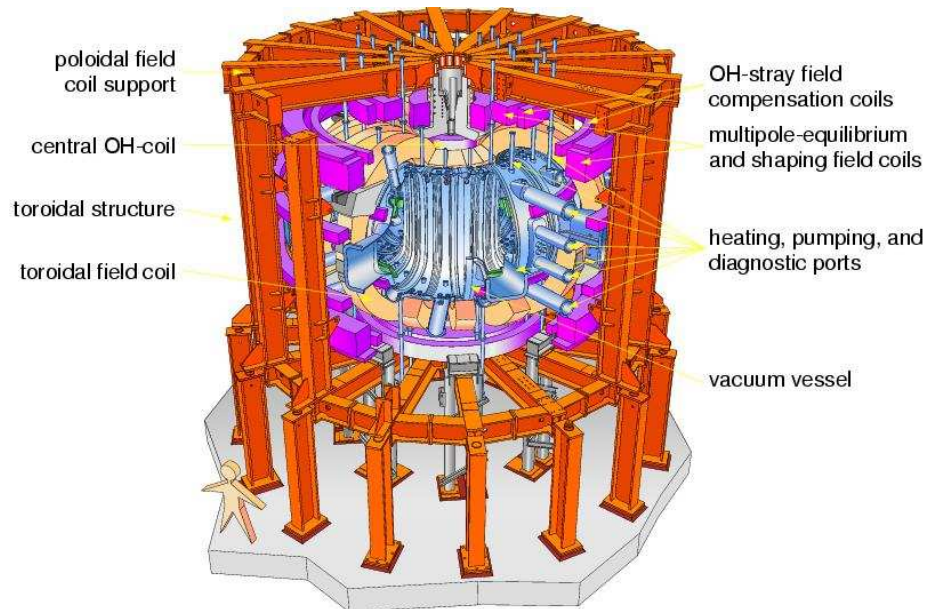

Figure B.1: ASDEX Upgrade Tokamak

Bibliography

[Alfvén, 1940] Alfvén, H. (1940). *Ark. Mat. Astron. Fys.*, 1(27A).

[Bergmann] Bergmann, A. Private communication.

[Boivin, 1993] Boivin, R.L. Zweben, S. (1993). Study of stochastic toroidal field ripple losses of charged fusion products at the midplane of tftr. *Nuclear Fusion*, 33.

[Bonheure, 2000] Bonheure, G. (2000). *Development of a fast ion detector for the textor-94 tokamak and application to the spectroscopy of 3 MeV fusion protons.* PhD thesis, l'Universite de Mons-Hainaut.

[Boozer, 1981] Boozer, A. H. (1981). Plasma equilibrium with rational magnetic surfaces. *Phys. Fluids*, 24(11):1999.

[Bosch, 1987] Bosch, H. (1987). *Diagnostik geladener Fusionreaktionprodukte in ASDEX.* PhD thesis, T.U.Muenchen.

[Carolipio, 1998] Carolipio, E. (1998). Simulations of beam ion transport during tearing modes in the diii-d tokamak. *Nuclear Fusion*.

[Chen, 1984] Chen, L. (1984). *Phys. Rev. Lett.*, 52:1122.

[Cheng, 1985] Cheng, C. (1985). *Phys. Fluids*, 29:3695.

[Darrow, 1995] Darrow, D. (1995). *Rev. Sci. Instrum.*, 66:476.

[Darrow, 2001] Darrow, D. (2001). Energetic ion loss diagnostic for the wendelstein 7-as stellerator. *Rev. Sci. Instrum.*, 72(7):2936.

[Darrow, 1992] Darrow, D. e. a. (1992). *Plasma Physics*, 16C.

[Darrow, 2002] Darrow, D.S. Medley, S. (2002). Measurments of prompt and mhd-induced fast ion loss from national spherical torus experiment plasmas. In *19 th IAEA Fusion Energy Conference, Lyon, France*.

[Duong, 1990] Duong, H.H. Heidbrink, W. (1990). A 15 mev proton diagnostic for diii-d. *Review of Scientific Instruments*, 61(10):3137.

[Duong, 1993a] Duong, H.H. Heidbrink, W. (1993a). Confinement of fusion produced mev ions in the diii-d tokamak. *Nuclear Fusion*, 33(2):211.

[Duong, 1993b] Duong, H.H. Heidbrink, W. (1993b). Loss of energetic beam ions during tae instabilities. *Nuclear Fusion*, 33(5):749.

[Edegal, 2000] Edegal, J. (2000). Drift orbit topology of fast ions in tokamaks. *Nuclear Fusion*, 40(9):1597.

[Goldstein, 1980] Goldstein, H. (1980). *Classical Mechanics*. Addison-Wesley Publishing Company.

[Gourdon, 1970] Gourdon, C. (1970). *Programme optimise de calculs numeriques dans les configurations magnetiques*. Centre d'etudes nucleaires de Fontenay aux Roses.

[Grove, 1985] Grove, D. (1985). *Nucl. Fusion*, 25:1167.

[Hawryluk, 1991] Hawryluk, R. (1991). *Plasma Phys. Controlled Fusion*, 33:1509.

[Heidbrink, 1984] Heidbrink, W. (1984). *Tokamak diagnostics using fusion products*. PhD thesis, Princenton University.

[Heidbrink, 1991] Heidbrink, W. (1991). *Nuclear Fusion*, 31:1635.

[Hsu, 1992] Hsu, C.T. Sigmar, D. (1992). Alpha-paricle losses from toroidicity-induced alfvén eigenmodes. part i: Phase-space topology og energetic particle orbits in tokamak plasma. *Phys. Fluids B*, 4(6):1492.

[Huysmans, 1990] Huysmans, G. (1990). *Comp. Phys.*

[Kallne, 1987] Kallne, J. Gorini, G. (1987). Measurments of the burn-up of fast he3 and t ions in deuterium plasmas. *Physica scripta*, 16.

[Kisslinger] Kisslinger, J. Private communication.

[Lin, 1995] Lin, Z. e. a. (1995). Gyrokinetic particle simulation of neoclassical transport. *Phys. Plasmas*, 2(8):2975.

[Lister, 1985] Lister, G. G. (1985). A fully 3-d neutral beam injection code using monte carlo methods. Technical report, Max-Planck-Institut Fuer Plasmaphysik.

[Littlejohn, 1982] Littlejohn, G. (1982). Variational principles of guiding center motion. *J. Plasma Physics*, 29:111.

[Ma, 1992] Ma, S. (1992). *Bull. Am. Phys. Soc.*, (37):1546.

[Miyamoto, 1989] Miyamoto, K. (1989). *Plasma physics for nuclear fusion*. MIT.

[Morozov, 1966] Morozov, A. (1966). *Reviews of Plasma Physics*, 2:201.

[Mynick, 1993] Mynick, H. (1993). Stochastic transport of mev ions by low-n magnetic perturbations. *Phys. Fluids B*, 5:2460.

[Pinches, 1996] Pinches, S. (1996). *Nonlinear Interaction of Fast Particles with Alvén Waves in Tokamaks*. PhD thesis, University of Nottingham.

[Rebut, 1985] Rebut, P. (1985). *Nucl. Fusion*, 25:1011.

[Rosenbluth, 1975] Rosenbluth, M. N. Rutherford, P. H. (1975). Excitation of alfvén waves by high-energy ions in a tokamak. *Physical Review Letters*, 34(23):1428.

[Sigmar, 1992] Sigmar, D. (1992). Alpha-particle losses from toroidicity-induced alfven eigenmodes. part ii: Monte carlo simulations and anomalous alpha-loss processes. *Phys. Fluids B*, 4(6):1506.

[Staebler, 1999] Staebler, A. (1999). The role of neutral beam injection geometry in advanced discharge scenarios on asdex upgrade. Technical report, Max-Planck-Institut fuer Plasmaphysik.

[Taylor, 1964] Taylor, J. (1964). *Phys. Fluids*, 2(4).

[Tsang, 1975] Tsang, K. (1975). *Phys Fluids*, 18:1282.

[Werner, 2001] Werner, A. Weller, A. (2001). Fast ion losses in the w7-as stellerator. *Review of scientific instrument*, 72(1):780.

[Wesson, 1997] Wesson, J. A. (1997). *Tokamaks*. Clarendon Press, Oxford.

[White, 1995] White, R.B. Fredikson, E. (1995). Toroidal alfvén eigenmode-induced ripple trapping. *Phys. Plasmas*.

[White, 1982] White, R. (1982). *Phys. Fluids*, 25(3).

[White, 1984] White, R. (1984). *Phys. Fluids*, 27:2455.

[White, 1989] White, R. (1989). *Theory of Tokamak Plasmas*. North-Holland Physics.

[White, 1990] White, R. (1990). Canonical hamiltonian guiding center variables. *Phys. Fluids B*, 2(4):845.

[White, 1983] White, R.B. Goldston, R. (1983). Theory of mode-induced beam particle loss in tokamaks. *Phys. Fluids*, 26(10):2958.

[Wong, 1991] Wong, K. (1991). *Phys. Rev. Lett.*, 66:1874.

[Wu, 1993] Wu, Y. (1993). Numerical simulation of bootstrap current. *Phys. Fluids B*, 5(9):3291.

[Xu, 1991] Xu, X. (1991). Numerical simulation of ion-temperature-gradient-driven modes. *Phys Fluids B*, 3(3):627.

Acknowledgments